HOKKAIDO UNIVERSITY

Title	Heterogeneity of oxygen isotopes and chemical compositions in a chondrule rim from carbonaceous chondrite
Author(s)	松田, 望
Degree Grantor	北海道大学
Degree Name	博士(理学)
Dissertation Number	甲第13756号
Issue Date	2019-09-25
DOI	https://doi.org/10.14943/doctoral.k13756
Doc URL	https://hdl.handle.net/2115/76088
Type	doctoral thesis
File Information	Nozomi_MATSUDA.pdf

Hokkaido University Collection of Scholarly and Academic Papers : HUSCAP

Heterogeneity of oxygen isotopes and chemical compositions in a chondrule rim from carbonaceous chondrite

炭素質コンドライト中のコンドリュールリムにおける酸素同位体と化学組成の不均一

A dissertation submitted for the doctoral degree of science

by

Nozomi Matsuda

Department of Natural History Sciences
Graduate School of Science
Hokkaido University

2019, September

Abstract

Chondrules are surrounded by igneous rims that show evidence of a high degree of melting. Due to their common occurrence in various types of chondrites, igneous rims formed on pre-existing chondrules throughout chondrule-forming regions of the solar nebula. Although igneous rim formation was related to chondrule formation event, the rim formation process is not fully understood. Because igneous rims have experienced extensive alteration on the parent body, primary features of igneous rims could be changed. In this thesis, to reveal the rim formation process, I determined the two-dimensional chemical and oxygen isotopic distributions in an igneous rim of a chondrule within the Northwest Africa 3118 $CV3_{oxA}$ chondrite with sub-micrometer resolution using secondary ion mass spectrometry and scanning electron microscopy.

The chondrule with type I porphyritic texture is completely surrounded by a coarse-grained igneous rim. The igneous rim is mostly dominated by olivine, which has more FeO-rich compositions compared to those within the host chondrule ($Fa_{2–5}$). The FeO contents show a bimodal distribution: MgO-rich ($Fa_{11–22}$) and FeO-rich (Fa_{40-49}) compositions. The igneous rim experienced aqueous alteration on the CV parent body. The aqueous alteration resulted in precipitation of the secondary FeO-rich olivine ($Fa_{40–49}$) and slightly disturbed the Fe-Mg distribution in the MgO-rich olivine phenocrysts ($Fa_{11–22}$) at about a 1 μm scale. However, no oxygen isotopic disturbances were observed at a scale greater than 100 nm. The MgO-rich olivine, a primary phase of igneous rim formation, has $\delta^{17}O = -6\pm3‰$ and $\delta^{18}O = -1\pm4‰$, and some grains contain extreme ^{16}O-rich areas ($\delta^{17}O$, $\delta^{18}O = \sim -30‰$)

nearly 10 μm across. I detected oxygen isotopic migration of approximately 1 μm at the boundaries of the extreme ^{16}O-rich areas. Using oxygen self-diffusivity in olivine, the heating time of the igneous rim formation could have continued from several hours to several days at near liquidus temperatures (~2000 K) in the solar nebula suggesting that the rim formed by a similar flash heating event that formed the chondrules.

Acknowledgements

It is a great pleasure to acknowledge the people who helped me throughout this work. First of all, I am indebted to Professor Hisayoshi Yurimoto. He provided me this precious study opportunity as a Ph.D. student in his laboratory. I have learned how to think logically and scientifically in the field of cosmochemistry and geochemistry form him.

I would like to express my deepest gratitude to Dr. Naoya Skamoto for teaching, assisting me in using the SIMS from the beginning and useful advice. I am deeply grateful to Professor Shogo Tachibana for his helpful advice and discussions. Without their guidance and persistent help, this thesis would not have been possible.

I thank to Mr. Sachio Kobayasi and Dr. Noriyuki Kawasaki for guiding me to the SIMS and SEM analyses. I could obtain much of my knowledge for analytical techniques from them.

I thank to Dr. Junji Yamamoto and Dr. Ken-ichi Bajo for their advice and valuable comments. I thank to Dr. Laurette Piani for discussion and teaching me English. I also thank Mr. Kousuke Nakamura for his support for sample evaluation. I am grateful to colleagues, staffs and student of yurimoto laboratory for many helpful talks for science and life.

Finally, this thesis would not have been possible without the continued support and encouragement of my family.

CONTENTS

List of Tables vi

List of Figures vii

1 INTRODUCTION 1

2 ANALYTICAL TECHNIQUES 5

2.1 Sample 5

2.2 Petrographic and X-ray analysis 6

2.3 Oxygen isotope measurements 6

2.3.1 Spot analysis 6

2.3.2 Isotopography 7

3 RESULTS 11

3.1 Petrography and mineralogy 11

3.1.1 Chondrule 11

3.1.2 Igneous rim 14

3.1.3 Matrix 25

3.2 Oxygen isotopic compositions of olivine 27

3.2.1 Spot analysis 27

3.2.2 Isotopograpy 28

4 DISCUSSION 34

4.1 Aqueous alteration on the parent body 34

4.2 Oxygen diffusion in MgO-rich olivine 41

5 CONCLUSIONS 47

REFERENCES.....79

APPENDIX.....85

List of tables

Table 1. Chemical composition of olivine in the chondrule 49

Table 2. Chemical composition of nepheline, plagioclace and augite in the chondrule 50

Table 3. Chemical composition of Fe-Ni metal, magnetite and sulfide in the chondrule 51

Table 4. Chemical composition of olivine in the igneous rim 53

Table 5. Chemical composition of feldspathic glass in the igneous rim.....55

Table 6. Chemical compositions of nepheline in the igneous rim 56

Table 7. Chemical composition of enstatite, pigeonite and augite in the igneous rim.....57

Table 8. Chemical compositions of Fe-(Ni) sulfides in the igneous rim 63

Table 9. Chemical composition of olivine in matrix.....64

Table 10. Oxygen isotopic composition of olivine in the chondrule 65

Table 11. Oxygen isotopic composition of olivine in the igneous rim 66

Table 12. Oxygen isotopic composition of olivine in the igneous rim from SCAPS 67

Table 13. Chemical composition of olivine along the line profiles 68

Table 14. Oxygen diffusion distance from $\delta^{18}O$ isotopograph 78

List of Figures

Figure 1. Backscattered electron image of Northwest Africa 3118 5

Figure 2. A schematic diagram of isotope microscope system 8

Figure 3. The spatial resolution of the $\delta^{18}O$ isotopograph 10

Figure 4. Petrography of a type I chondrule surrounded by the igneous rim 12

Figure 5. Backscattered electron image of the mesostasis in the chondrule 13

Figure 6. Backscattered electron image of the opaque phase in the chondrule 14

Figure 7. Petrography of the igneous rim 15

Figure 8. Histogram of Fa compositions for olivine grains 16

Figure 9. FeO-rich olivine, enstatite, pigeonite, augite, feldspathic glass, nepheline and Fe-(Ni) sulfide in the igneous rim 18

Figure 10. Crystallographic orientation of olivine and vein 20

Figure 11. The compositions of FeO-rich olivine from the chondrule-rim boundary to the rim-matrix boundary 21

Figure 12. The features of FeO-rich olivine 22

Figure 13. Composition profiles along a line crossing the interface between the FeO-rich olivine and MgO-rich olivine 23

Figure 14. Petrography of matrix 26

Figure 15. Oxygen isotopic compositions of olivine 28

Figure 16. Distribution of the extreme ^{16}O-rich olivine grains 29

Figure 17. The $\delta^{18}O$ isotopographs containing the extreme ^{16}O-rich olivines 32

Figure 18. Oxygen self-diffusion distance on the parent body 41

Figure 19. Oxygen diffusion distance in MgO-rich olivine 42

Figure 20. Fe-Mg interdiffusion distance during the igneous rim formation.....45

Figure 21. Heating duration of the igneous rim.....46

Chapter 1

INTRODUCTION

Chondrites are meteorites that are the oldest and most primitive rocks in the solar system. They provide clues to the evolution of planetary materials in the early solar system. Chondrites consist of chondrules, refractory inclusions (Ca-Al-rich inclusions (CAIs) and amoeboid olivine aggregates (AOAs)), Fe-Ni metal, and matrix. CAIs are the oldest objects (Amelin et al. 2002) in the meteorite and formed as condensates from a gas of solar compositions in a high temperature (Grossman, 1972). In contrast, chondrules are major constituents of chondrites and are millimeter to sub-millimeter sized spherules. It is believed that chondrules formed during flash heating events in the solar nebula (e.g., Gooding et al., 1980; Grossman and Wasson, 1982; Hewins, 1996). Chondrules formation had continued for at least ~3 My after CAIs formation (Connelly et al., 2012). Although chondrules and CAIs have been extensively and repeatedly studied, the information on the evolution of planetary materials in the early solar system is limited after chondrule formation.

Chondrules are often surrounded by rims that formed in the nebula after the host chondrules. Chondrule rims are divided into two types: (1) fine-grained or matrix-like rims that are similar in chemical composition and grain size to the host chondrite matrix (e.g., Ashworth, 1977; Allen et al., 1980; King and King, 1981; Scott et al., 1984), and (2) coarse-grained or igneous rims that show evidence of a high degree of melting (e.g., Rubin, 1984; Rubin and Wasson, 1987; Krot and Wasson, 1995). Igneous rims surround ~50%, ~10% and <1% of chondrules in the CV3, H-L-LL3, and CO3 chondrites, respectively (Rubin, 1984). The ubiquitous occurrence

of igneous rims across the chondrite groups suggests that igneous rim formation commonly occurred in the solar nebula and was related to chondrule formation. However, the rim formation process is not as well understood compared with chondrule formation, even CV chondrite have the most abundance of igneous rims. For example, the heating duration has not yet been evaluated.

Chondrules in CV chondrite had experienced complex alteration on the parent body (e.g., Krot et al., 1995, 1998, 2004; Maruyama et al., 1999; Maruyama and Yurimoto, 2003; Brearley, 2003), suggesting igneous rims in CV chondrites also had experienced the same alteration on the parent body. The alteration processes have modified primary features (e.g., texture, chemical, and oxygen isotope compositions) of igneous rims. Thus, to constrain rim formation process, it is important to understand what are the primary features in igneous rims, what has changed in them of igneous rims, and how much they have changed.

Oxygen is the third abundant elements in the solar system and the most in rocky planets. Oxygen isotopic compositions of solar system materials are discovered heterogeneous (Clayton et al., 1973). Oxygen has three stable isotopes (^{16}O, ^{17}O, and ^{18}O), which are synthesized by a different nuclear process. Oxygen isotopic variations provide important constraints on the origin and early evolution of the solar system. The oxygen isotopic anomalies are plotted along with the carbonaceous chondrite anhydrous mineral (CCAM) line with slope ~1. Refractory inclusions, such as Ca-A-rich inclusions (CAIs) and amoeboid olivine aggregates (AOAs), generally show ^{16}O-rich compositions, whereas chondrules are relatively ^{16}O-depleted values. However, olivine phenocrysts within igneous rims sometimes contain very ^{16}O-rich areas in their interiors (e.g., Takeda et al., 2002; Nagashima et al., 2003, 2011, 2013,

2015). The ^{16}O-rich composition is clearly distinct from that of most olivine in igneous rims and the phenocrysts in the host chondrules, and is similar to that of amoeboid olivine aggregates. Such ^{16}O-rich olivine cannot form during chondrule formation because the oxygen isotopic compositions of the minerals crystallized from chondrule melts are typically close to those of the rocky planets (Yurimoto et al., 2008; Tenner et al., 2018). Therefore, these ^{16}O-rich olivines are the igneous rim feedstocks and heating process survivors (i.e. relict grain) from the igneous rim formation, and the rim formation process could be traced using these olivines. However, oxygen isotopic compositions with the extreme ^{16}O-rich in an igneous rim from CV_{oxA} have been poorly studied.

In this study, the main purpose is to reveal the formation process of an igneous rim from CV_{oxA} chondrite. I performed the two-dimensional micro-distribution of the chemical compositions and oxygen isotopes in an igneous rim from the Northwest Africa (NWA) 3118 CV_{oxA} chondrite intercorrelated with detailed petrography.

Chapter 2 is the analytical methods and conditions. In order to investigate oxygen isotopic distributions of an igneous rim, isotope microscope composed of a direct combination of secondary ion mass spectrometry and 2-dimensional ion detector has used for the isotopic study. It is possible to compare between chemical and oxygen isotopic distributions of minerals in an igneous rim. Chapter 3 describes the results of petrologic observation and oxygen isotope measurements. Detailed petrography was performed to understand alteration features on the parent body in the igneous rim. Investigations of extreme ^{16}O-rich olivine and oxygen isotopic distributions were performed to constrain rim formation process. In chapter 4, first of all, redistribution of

chemical and oxygen isotope composition on the parent body is discussed. Next, I discuss the exchange of chemical and oxygen isotope composition during rim formation in the solar nebula. Finally, I estimated the heating duration of an igneous rim to constrain rim formation process. In chapter 5, I conclude all the findings in this thesis. It is noted that chapter 2, chapter 3, and chapter 4 is taken from a manuscript accepted to Geochemistry.

Chapter 2

ANALYTICAL TECHNIQUES

2.1 Sample

A polished thin section sample of the Northwest Africa (NWA) 3118 CV_{oxA} chondrite containing an igneous rimmed porphyritic olivine chondrule was used in this study. NWA 3118 is classified as a CV_{oxA} chondrite (Russell et al., 2005). Figure 1 shows whole image of NWA 3118 thin section.

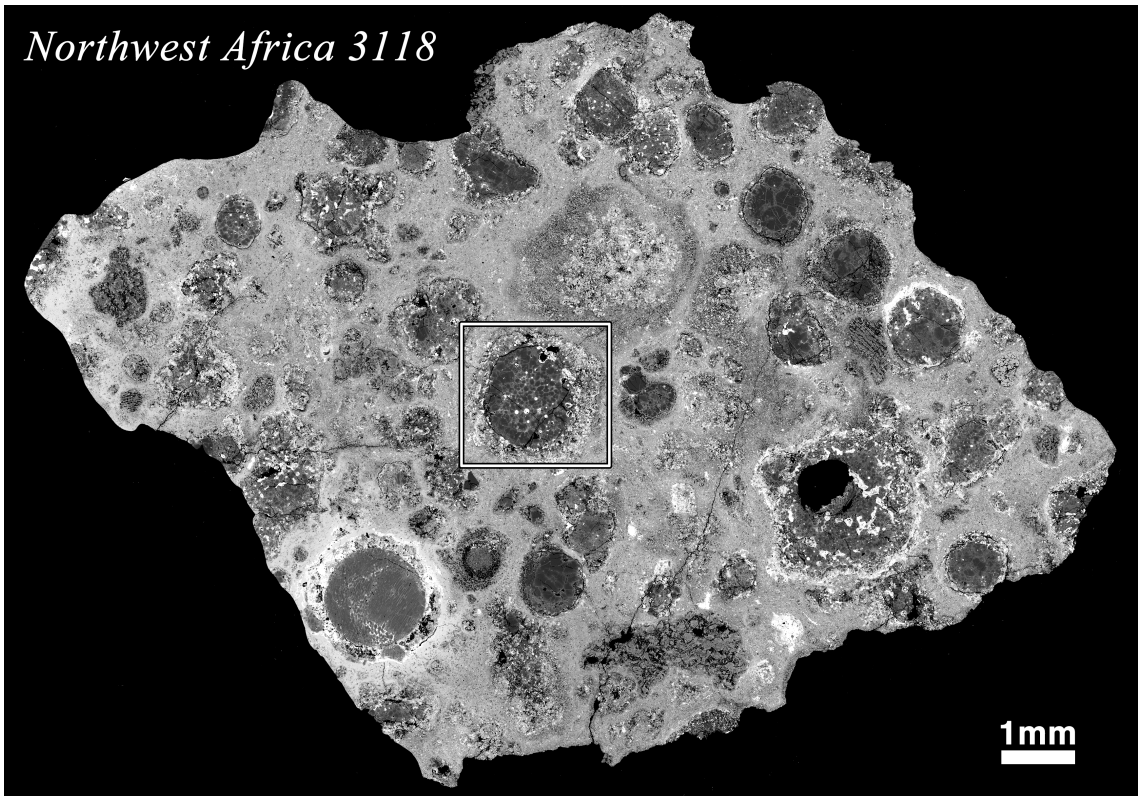

Figure 1. Backscattered electron (BSE) image of Northwest Africa 3118. The areas outlined by square are enlarged and shown in Figure 4.

2.2 Petrographic and X-ray analysis

The section was coated with a thin film (~20 nm) of carbon for the petrographic observations, quantitative elemental analysis, and X-ray elemental mapping using a field emission scanning electron microscope (FE-SEM; JEOL JSM-7000F) equipped with an energy dispersive spectrometer (EDS; Oxford X-Max 150) at the Hokkaido University. In addition, a crystallographic orientation map was obtained using an electron backscattered diffraction (EBSD; Oxford HKL) installed on the FE-SEM. A 15 keV electron beam probe was applied with currents of 0.3 nA and 5nA for the quantitative chemical analysis, and X-ray elemental mapping and EBSD mapping, respectively. The step sizes and the dwell times for the mapping were typically set at 0.5 μm and 10 μs, respectively.

2.3 Oxygen isotope Measurements

2.3.1 Spot analysis

The section was coated with a Au thin film (70 nm) before the secondary ion mass spectrometry (SIMS) analysis. The point analyses of oxygen isotopes were made using a SIMS (Cameca ims-1280HR) at Hokkaido University. I applied a focused Cs^+ ion primary beam (3−5 μm in diameter) with a total kinetic energy of 20 keV. A normal incident electron gun was used for charge compensation on the primary beam irradiated area. The secondary ions of $^{16}O^-$ sputtered by the primary beam were accelerated to 10 keV and measured using a Faraday cup (FC), and the $^{17}O^-$ and $^{18}O^-$ were measured using an electron multiplier (EM) in the peak jumping mode of the sector magnet. The mass resolution power (MRP) of $M/\Delta M$ was set at ~ 5500 to ensure that the contribution of $^{16}OH^-$ to $^{17}O^-$ was negligible. The $^{16}O^-$ signals

were obtained by subtracting background counts of the FC from the total FC counts of $^{16}O^-$. The EM was operated in the pulse counting mode with a dead time of 48 ns. A typical count rate for $^{16}O^-$ was set as ~ 8×10^7 cps. Each measurement was conducted for 30 cycles of a counting sequence with $^{16}O^-$ for 1 s, $^{17}O^-$ for 2 s, and $^{18}O^-$ for 1 s with a waiting time of 2 s for every mass to stabilize the sector magnetic field.

The oxygen isotopic compositions are reported as per mil deviations relative to standard mean ocean water (SMOW);

$$\delta^{17,18}\mathrm{O}\ (‰) = \left[\left({}^{17,18}\mathrm{O}/{}^{16}\mathrm{O}_{unknown}\right)/\left({}^{17,18}\mathrm{O}/{}^{16}\mathrm{O}_{SMOW}\right) - 1\right] \times 1000 \quad (1)$$

The instrumental mass fractionation was corrected using an olivine crystal from San Carlos, Arizona, USA (Fa_8, $\delta^{17}O_{SMOW}$ = 2.7‰, $\delta^{18}O_{SMOW}$ = 5.2‰; Yurimoto et al., 2011).

2.3.2 Isotopography

The quantitative oxygen isotope distribution (isotopography) on the thin section was performed using an isotope microscope system (Cameca ims-1270 + SCAPS, Fig. 2) at the Hokkaido University (Yurimoto et al., 2003). A static Cs^+ primary beam of 20 keV was homogeneously irradiated on the sample area with an oval shape approximately 70 μm in diameter with a beam current of ~0.5–2 nA. A normal incident electron gun was utilized to compensate positive charging of the sputtered region due to the primary beam irradiation. An accelerating voltage of 10 kV was applied and secondary ions of 10 keV ±75 eV were measured by a stacked CMOS-type active pixel sensor (SCAPS) using the energy band-pass slit in the ims-1270. A contrast aperture of 150 μm in diameter was used. The exit slit was

narrowed enough to eliminate the contribution of interference ions to the isotope images. The isotope image was projected on the SCAPS detector that has 600 × 576 pixels with a stacked electrode for each pixel and directly detects the secondary ions (Takayanagi et al., 2003). Each pixel can store the signal of up to 50,000 ions and the pixel size corresponds to 0.28 μm of the isotope image. The stored charge in the capacitor of a pixel can be read out individually through a readout transistor without destruction of the charge and an operating reset transistor (a non-destructive readout mode). This function realizes the SCAPS detector as an integral-type ion detector. The charge signal was acquired with the PXI system controlled by LabVIEW software (Sakamoto and Yurimoto 2006). The readout time for one image frame was 5.25 s with a noise level of 55 μV corresponding to 1.8 ions in the non-destructive readout mode (Yamamoto et al., 2010).

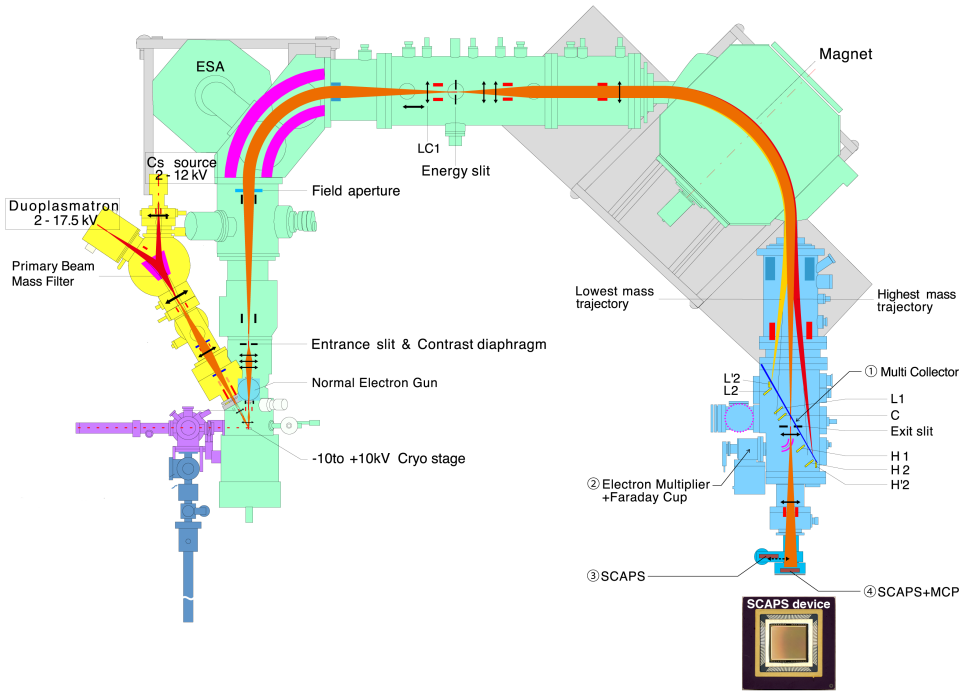

Figure 2. A Schematic diagram of isotope microscope system at the Hokkaido University. A SCAPS ion imager is placed on the projection plane of the secondary ion image.

The typical mass sequence for acquiring the secondary ion images for one cycle was 'reset', $^{27}Al^{16}O^-$, $^{56}Fe^{16}O^-$, $^{24}Mg^{16}O^-$, $^{28}Si^-$, 'reset', $^{16}O^-$, 'reset', $^{18}O^-$ and $^{16}O^-$. The 'reset' images were taken during the resetting operation of the pixel capacitors (a destructive readout mode) and used as the reset frames for the fixed pattern noise correction (Matsumoto et al., 1993; Kunihiro et al., 2001; Nagashima et al., 2001; Takayanagi et al., 2003). The typical measurement times for the secondary ion species during one cycle were 420 s for reset, 25 s for $^{27}Al^{16}O^-$, 50 s for $^{56}Fe^{16}O^-$, 50 s for $^{24}Mg^{16}O^-$, 10 s for $^{28}Si^-$, 420 s for reset, 5 s for $^{16}O^-$, 420 s for reset, 250 s for $^{18}O^-$, and 5 s for $^{16}O^-$. Each isotopograph was calibrated in the non-destructive readout mode. The last part of the analytical cycle ('reset', $^{18}O^-$ and $^{16}O^-$) was repeated several times in order to integrate the secondary ion signals to improve the precisions of isotopograph. The acquired $^{16}O^-$ and $^{18}O^-$ isotopographs were averaged for each isotope after an image shift correction (Sakamoto et al., 2007; Park et al., 2012). The amount of image shift was 1 to 3 pixels corresponding to 0.28 to 0.84 μm on the sample surface. The $\delta^{18}O$ isotopographs were obtained by calculating secondary ion ratios of the $^{18}O/^{16}O$ and normalized to the SMOW scale using $\delta^{18}O$ values of minerals obtained by point analyses. The typical precision (2SD) of the $\delta^{18}O$ isotopographs is 30‰ per pixel corresponding to 0.28 μm × 0.28 μm on the isotope image. An image processing method of moving average with 3 × 3 pixels was applied to the isotope ratio images to reduce the statistical fluctuation of the secondary ions. Therefore, the precision of the isotope ratio is improved to ~10‰ per pixel for the smoothed image. The $\delta^{18}O$ values of the olivine grains in the isotopography were calculated from an 11 × 11 pixels area that corresponds to the beam spot size (approximately 3 × 3 μm^2) for the spot analysis. The spatial resolution of the isotopography is evaluated by the

boundaries between the extremely ^{16}O-rich olivine and the FeO-rich olivine that is defined by the width between 16% and 84% of the oxygen isotopic composition difference across the boundary (Fig. 3). The spatial resolution of the δ^{18}O isotopograph is calculated to be 0.8 μm.

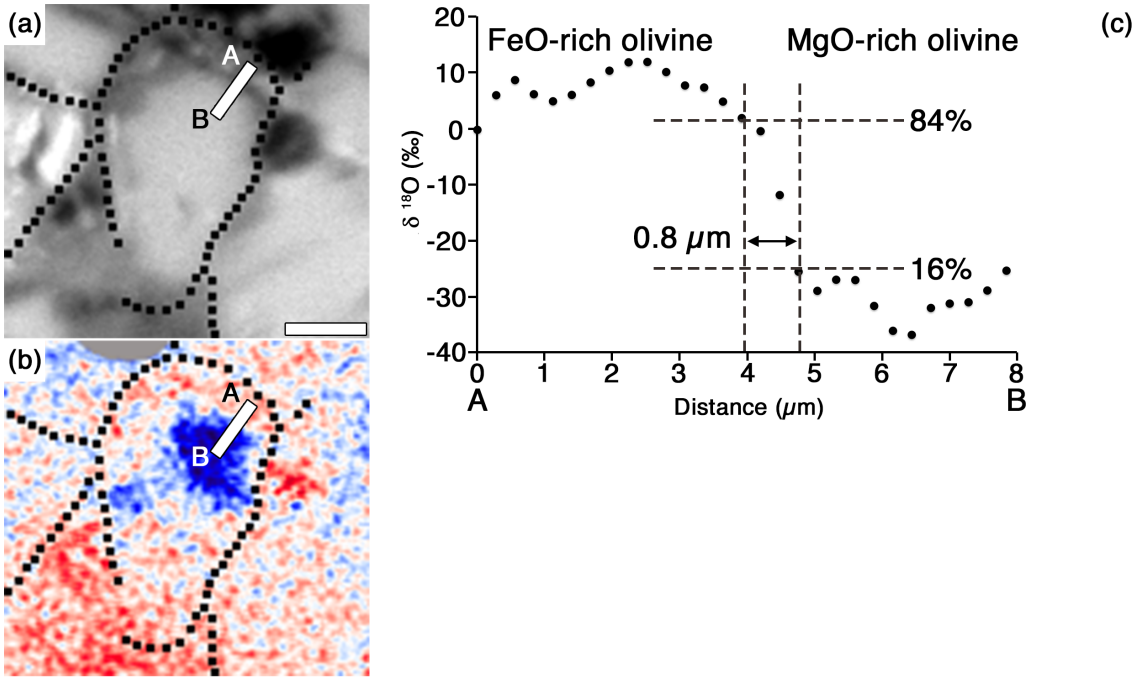

Fig. 3. (a) $^{24}Mg^{16}O^{-}$ isotopograph. (b) δ^{18}O isotopograph. (c) δ^{18}O profile along line A-B between the MgO-rich and FeO-rich olivine. The same isotopographs are used in Fig. 7c to determine the δ^{18}O profile within the MgO-rich olivine. Scale bar is 10 μm.

Chapter 3

RESULTS

3.1 Petrography and mineralogy

3.1.1 Chondrule

The Northwest Africa (NWA) 3118 is the oxidized Allende-like $CV3_{oxA}$ carbonaceous chondrite (Russell et al., 2005). The chondrule studied is completely surrounded by a coarse-grained igneous rim (Fig. 4a). The chondrule has a rounded shape of 1.4 mm diameter with a type I (Mg# (= molar MgO/(MgO + FeO) %) ≥ 90)) porphyritic texture. The chondrule is mainly composed of olivine phenocrysts (Fa_{2-5}) and mesostasis in addition to opaque nodules. The major elemental compositions of these phases are listed in Tables 1−3 (Figs. A1−A3).

The olivine phenocrysts are euhedral and have a core-mantle structure. The grain shapes and sizes are rounded and smaller (20−150 μm) in the core, and an elliptic and larger (200−300 μm) in the mantle. The mesostasis of the chondrule is represented by dendritic plagioclase and augite (Fig. 5). The plagioclase is often replaced by nepheline, a secondary mineral formed during fluid-assisted thermal metamorphism on the CV chondrite parent asteroid. The secondary nepheline is abundant on the periphery (Figs. 4b, c). Opaque phases occur as rounded to sub-rounded nodules consisting of Fe-Ni metal, Fe sulfide, and metal-sulfide aggregates (Fig. 6). The Fe-Ni metal and Fe sulfide are often replaced by magnetite.

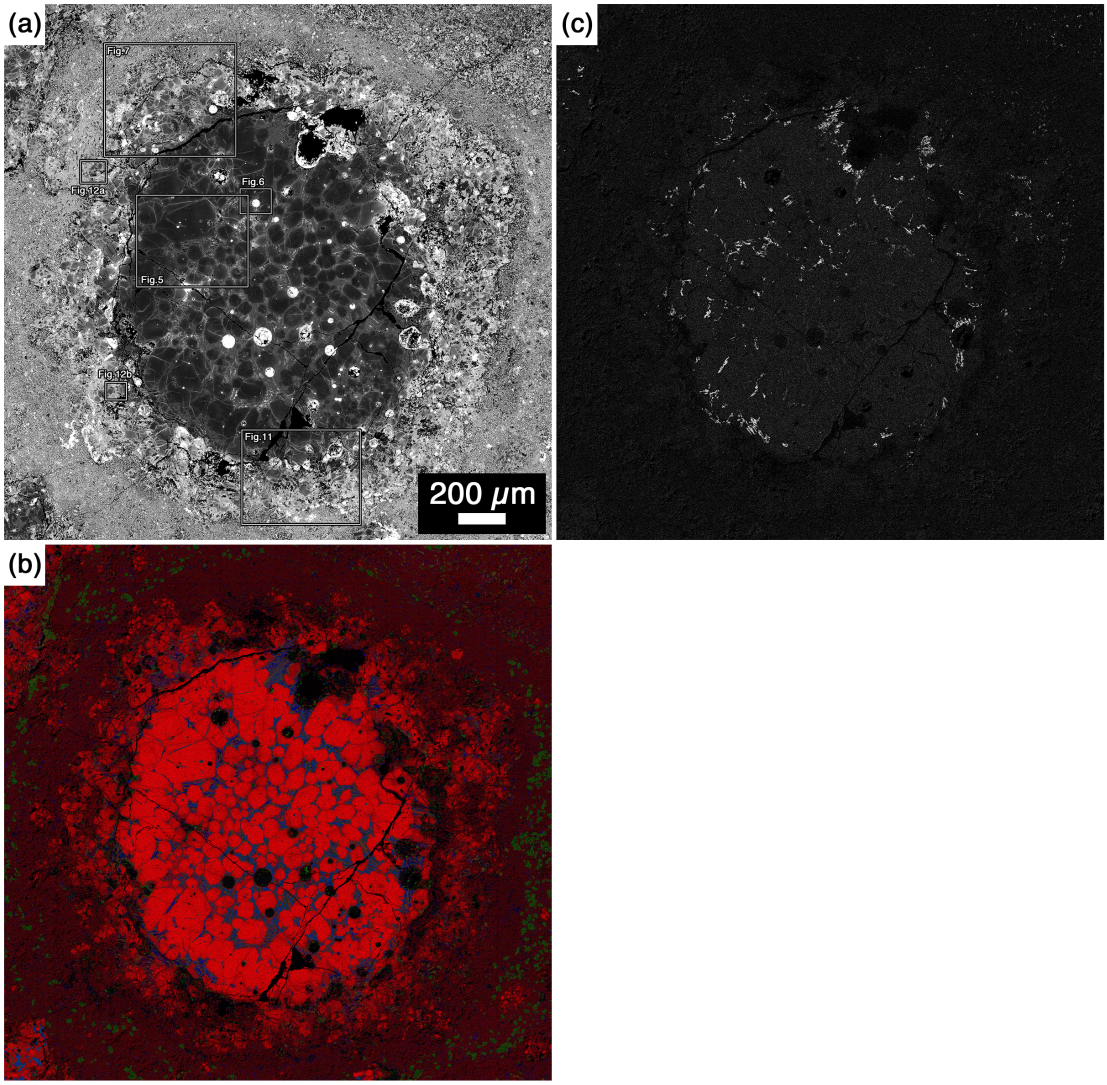

Fig. 4. (a) Back-scattered electron image of a type I chondrule surrounded by the igneous rim in the NWA3118 CV_{oxA} chondrite. The chondrule mainly consists of olivine, mesostasis, magnetite, sulfide and Fe-Ni metal. The areas outlined by squares are enlarged and shown in the figures indicated. (b) Combined X-ray elemental map of Kα lines of Mg (red), Ca (green), and Al (blue). Blue-colored areas are mainly composed of plagioclase and nepheline. (c) X-ray elemental map of Na Kα. White-colored areas are nepheline-rich.

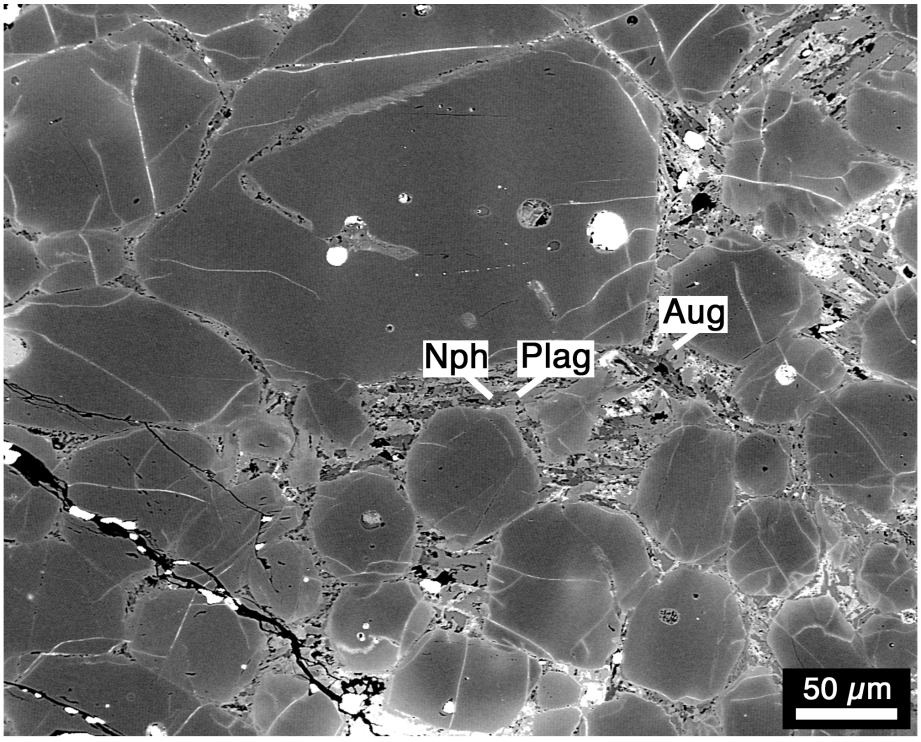

Fig. 5. Back-scattered electron image of boxed area “Fig. 5” of Fig. 4 showing the mesostasis consisting plagioclase (Plag), nepheline (Nph) and augite (Aug). These minerals fill interstices among olivine phenocrysts and have lath shapes or blocky morphology.

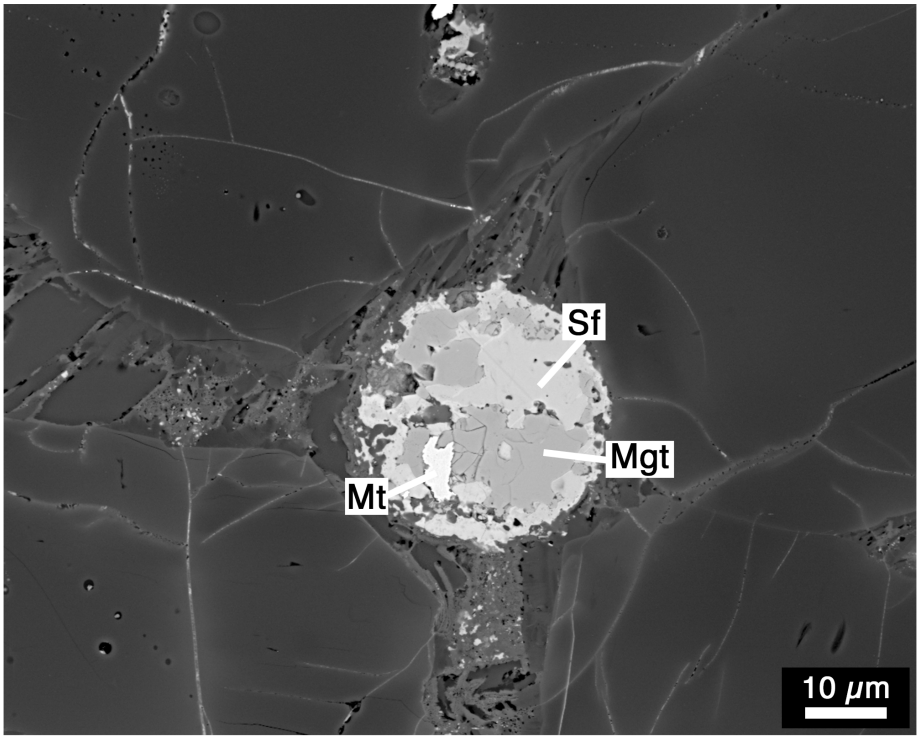

Fig. 6. Back-scattered electron image of boxed area “Fig. 6” of Fig. 4 showing opaque phases in the chondrule. Opaque is a mixture of Fe-Ni metal (Mt), Fe sulfide (Sf) and magnetite (Mgt). The magnetite formed by replacement of Fe-Ni metal and Fe sulfide.

3.1.2 Igneous rim

A coarse-grained igneous rim with thickness up to 400 μm occurs continuously around the chondrule (Fig. 4a). Mechanical cracks occur near the boundary between the chondrule and the coarse-grained rim. The cracks are secondary in origin, formed after the formation of the rim because the cracked olivine-grains show the same crystallographic orientations across the cracks, indicating that they were originally single crystal grains (Figs. 7a, b).

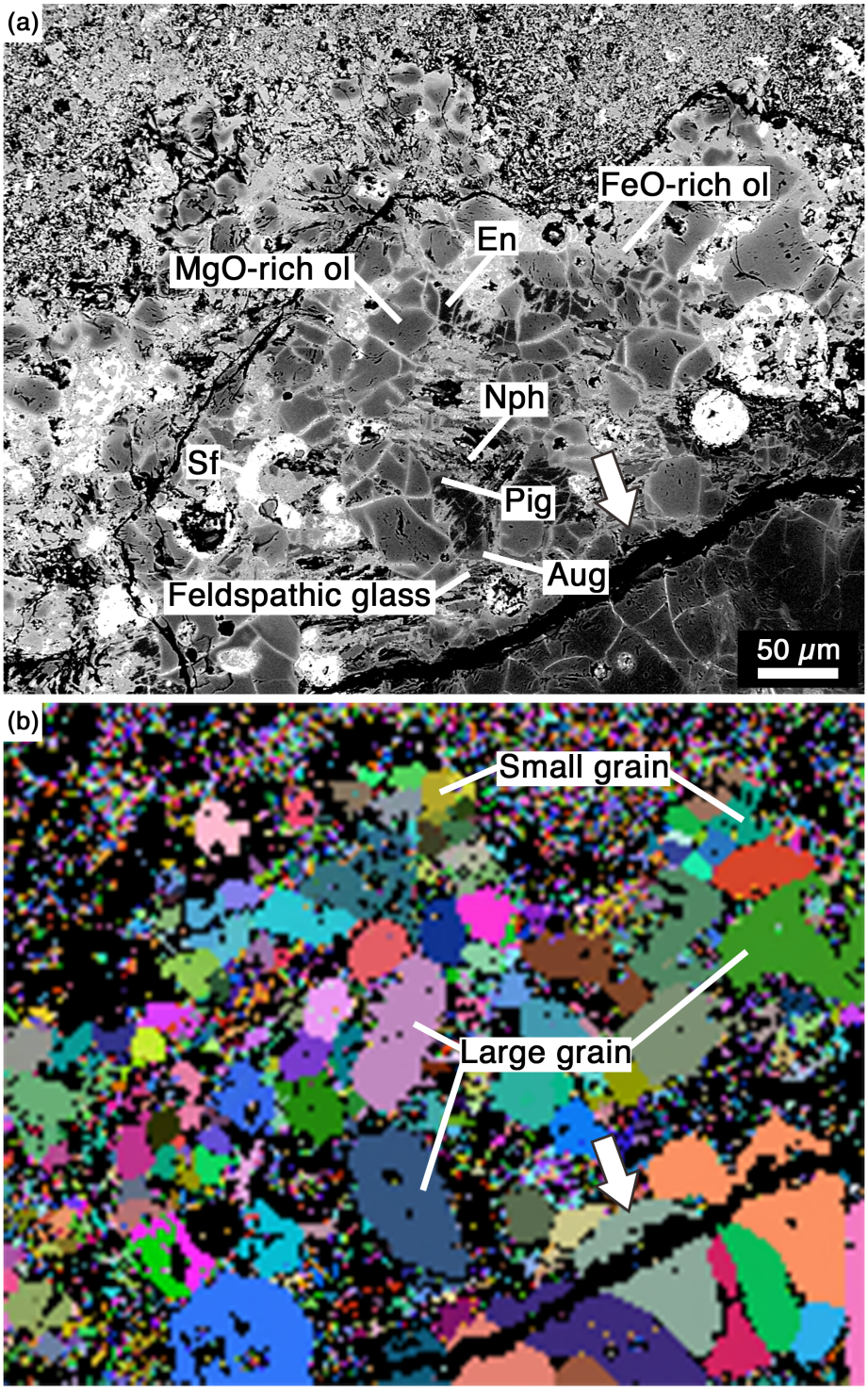

Fig. 7. (a) Back-scattered electron image and (b) EBSD map of boxed area "Fig. 7" in Fig. 4 showing the boundary between the igneous rim and the host chondrule. The igneous rim consists of MgO-rich olivine (MgO-rich ol), FeO-rich olivine (FeO-rich ol), enstatite (En), pigeonite (Pig), sulfide (Sf), augite (Aug), feldspathic glass and nepheline (Nph). Arrow shows that single crystal olivine grains were mechanically broken along a crack.

The coarse-grained rim is mostly dominated by olivine. The olivine grains are enriched in FeO compared with those within the host chondrule. The FeO contents show a bimodal distribution with peaks at MgO-rich ($Fa_{\sim 11-22}$) and FeO-rich ($Fa_{\sim 40-49}$) compositions (Figs. 8, A4 and Table 4). Enstatite, pigeonite, feldspathic glasses, augite, nepheline, and Fe±Ni sulfide (troilite, pyrrhotite or pentlandite) are identified in the rim (Fig. 7a). The major elemental compositions of these minerals are summarized in Tables 5−8 (Figs. A5 and A6).

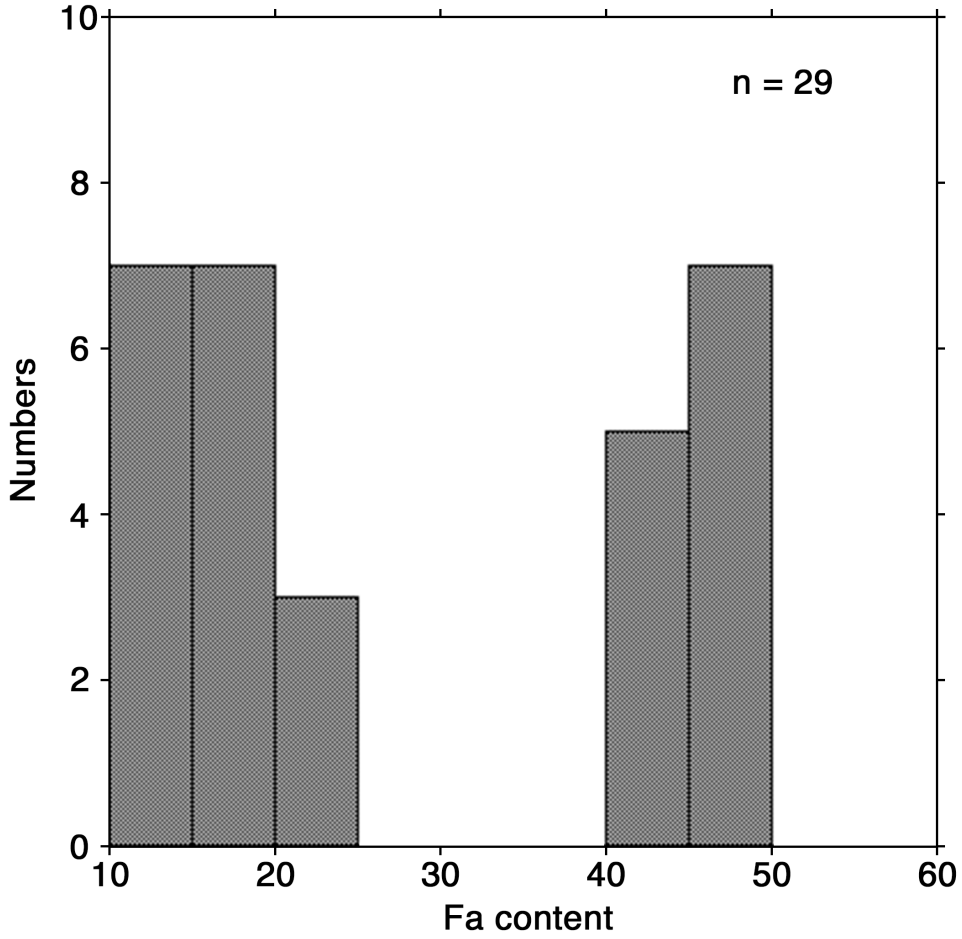

Fig. 8. Modal abundances of Fa compositions for olivine grains in the igneous rim. The distribution shows bimodal (Fa_{11-22} and Fa_{40-49}) distribution. The 29 olivine grains were selected randomly from the igneous rim.

Enstatite and pigeonite ($Fs_{1-4}Wo_{1-2}$ and $Fs_{1-4}Wo_{4-10}$) are subhedral and often partially replaced by FeO-rich olivine (Fig. 9a). Augite ($Fs_{1-5}Wo_{27-42}$) overgrows the enstatite and pigeonite (Fig. 9a), and occurs in the mesostasis of the rim. The rim contains abundant spherical or irregular assemblages of Fe- and Fe-Ni sulfides (troilite, pyrrhotite, and pentlandite), whereas Fe-Ni metal and magnetite are rare (Fig. 9b). They are also replaced by FeO-rich olivine (Fig. 9c). Feldspathic glass and nepheline occur in the mesostasis (Fig. 9a). These petrographic observations are similar to those reported in the Allende meteorite by Brearley and Krot (2013), who showed that metasomatic alteration took place on the parent body.

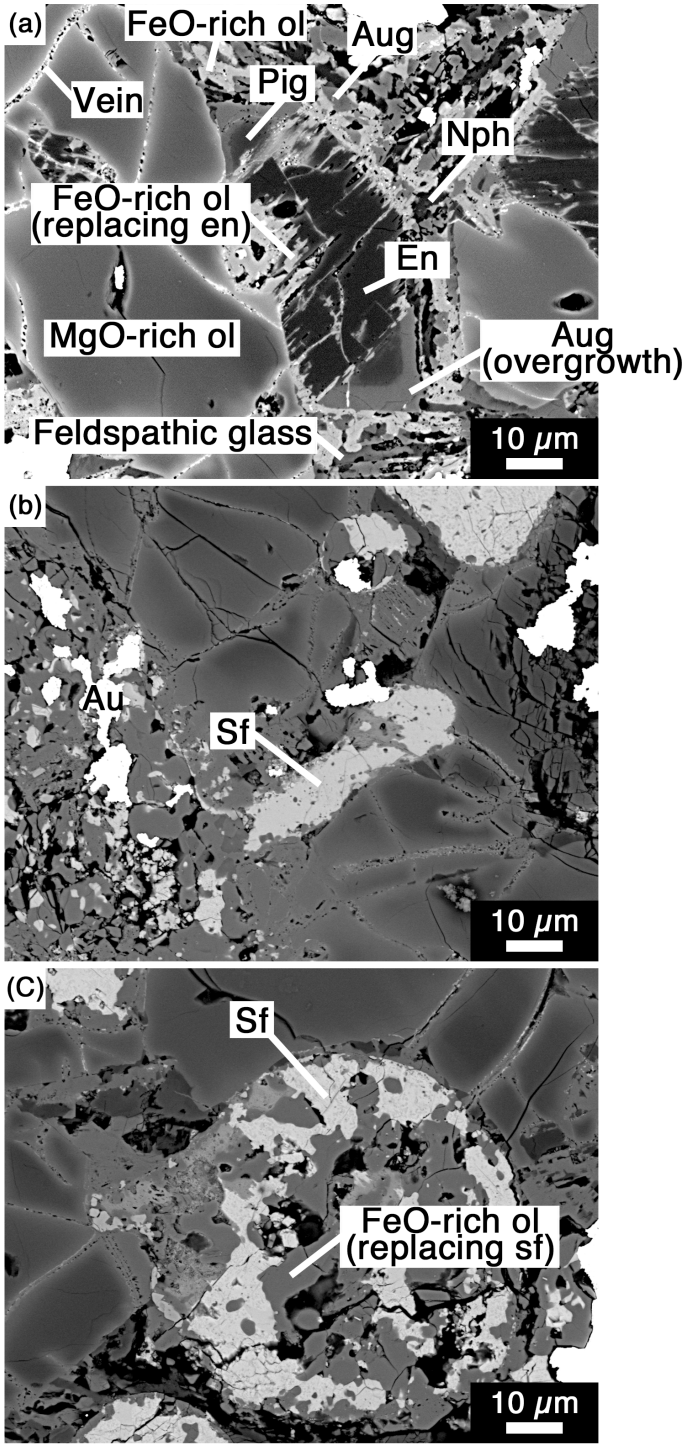

Fig. 9. Back-scattered electron images of the igneous rim. (a) Enstatite (En) are partially replaced by FeO-rich olivine (FeO-rich ol). Veins of FeO-rich olivine infiltrate into the MgO-rich olivine. Augite (Aug) appears as an overgrowth on enstatite and pigeonite (Pig). Feldspathic glass coexists with nepheline in the mesostasis. (b and c) Fe-(Ni) sulfide (troilite, pyrrhotite or pentlandite) shows spherical or irregular shape. Some opaque nodules are pseudomorphed by FeO-rich olivine.

The MgO-rich olivine grains are euhedral to subhedral. Their grain size gradually changes radially from 100–150 μm near the chondrule-rim boundary to 10–50 μm at the rim-matrix boundary (Figs. 7a, b). Some MgO-rich olivine grains are overgrown by FeO-rich olivine with the same crystallographic orientation (Figs. 10a, c). The cracks of the MgO-rich olivine grains are healed by FeO-rich olivine as veins (Figs. 10b, d).

The FeO-rich olivine appears anhedral and fills the spaces among the other minerals in the rim (Fig. 9a). The compositions of FeO-rich olivine gradually change from Fa_{42} at the chondrule-rim boundary to Fa_{48} at the rim-matrix boundary (Fig. 11). The igneous rim is covered with FeO-rich olivine at the matrix-rim boundary (Fig. 12a). The FeO-rich olivines show both smooth and porous surfaces on the polished thin section (Fig. 12b).

The MgO-rich olivine grains in the igneous rim have Fe-Mg chemical zoning near many crystal surfaces. Where there are grains with FeO-rich olivine overgrowths, the zoning gradients occur perpendicular to the surfaces of the MgO-rich olivine (Figs. 13a–f). No Mg-Fe zoning is observed on the sides of the FeO-rich olivines. Gradients in Mg-Fe composition also occur perpendicular to the veins in MgO-rich olivine grains (Figs. 13g–h).

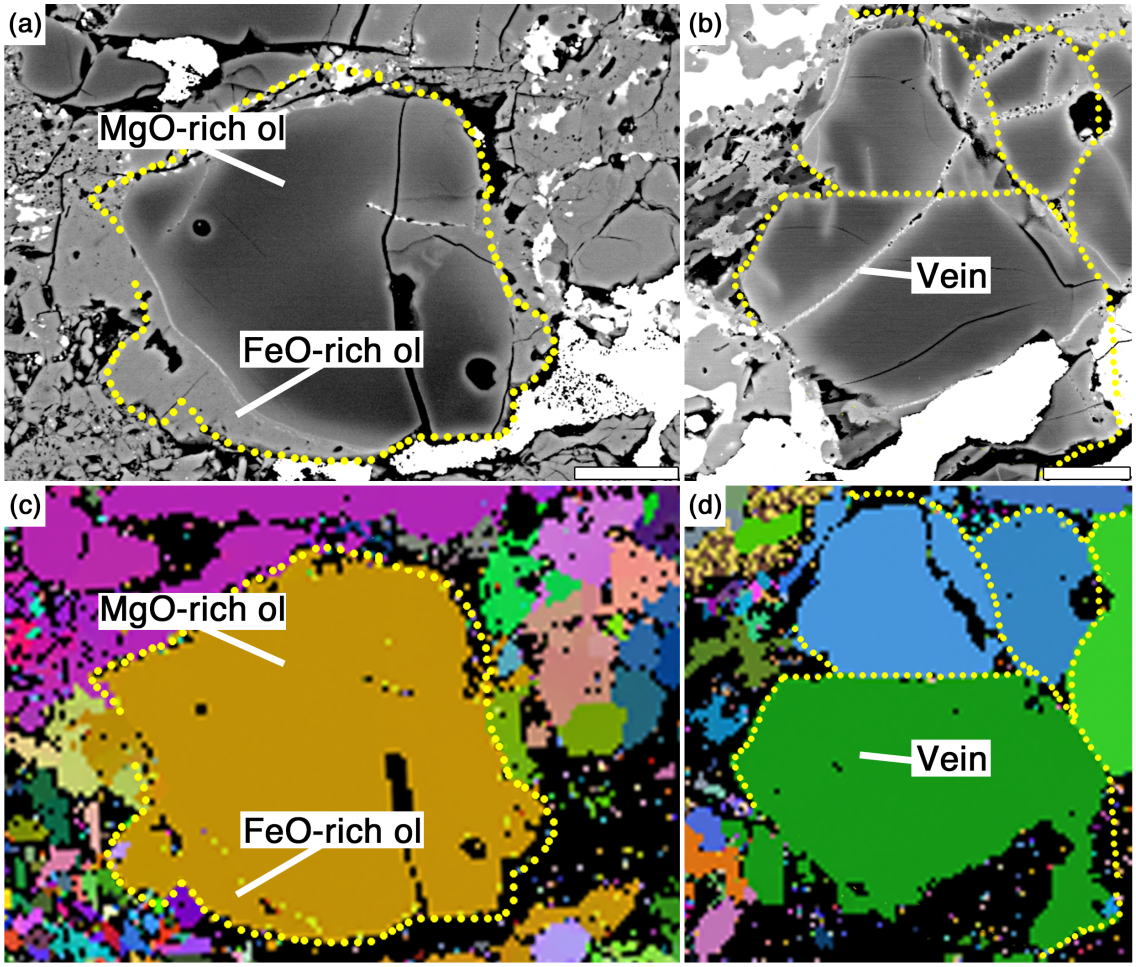

Fig. 10. Back-scattered electron images (a and b) and the EBSD images (c and d) of olivine grains in the igneous rim. Dotted lines represent grain boundaries. Scale bar is 10 μm. In (c), the EBSD images show that the FeO-rich olivine (FeO-rich ol) and MgO-rich olivine have the same crystallographic orientation. In (d), the MgO-rich olivine grains separated by veins have the same crystallographic orientation.

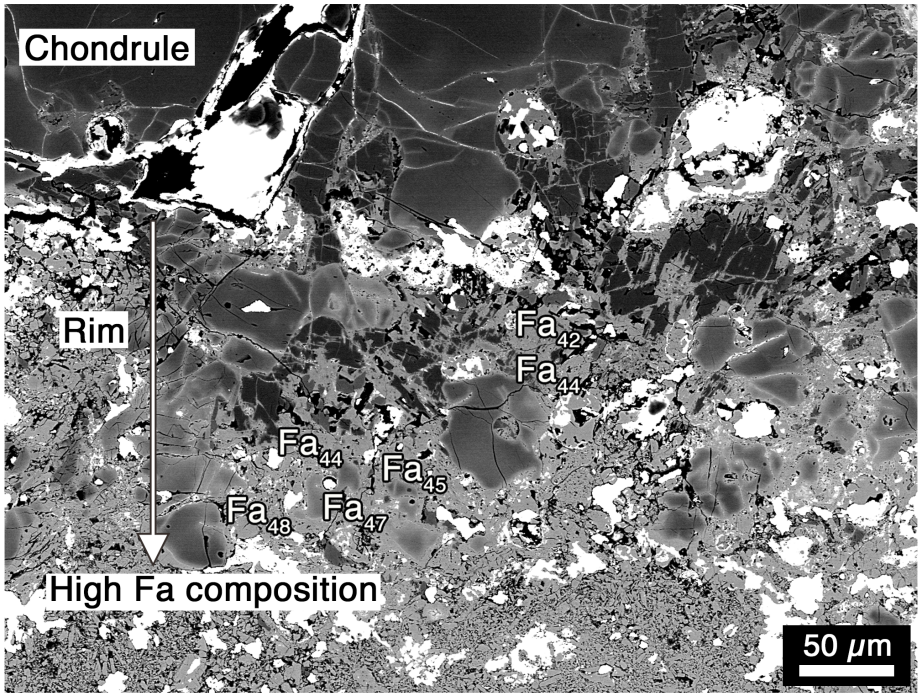

Fig. 11. Back-scattered electron image of boxed area "Fig. 11" in Fig. 4. Fa composition (Fe/(Mg + Fe)) of FeO-rich olivine in igneous rim increases towards the rim-matrix boundary.

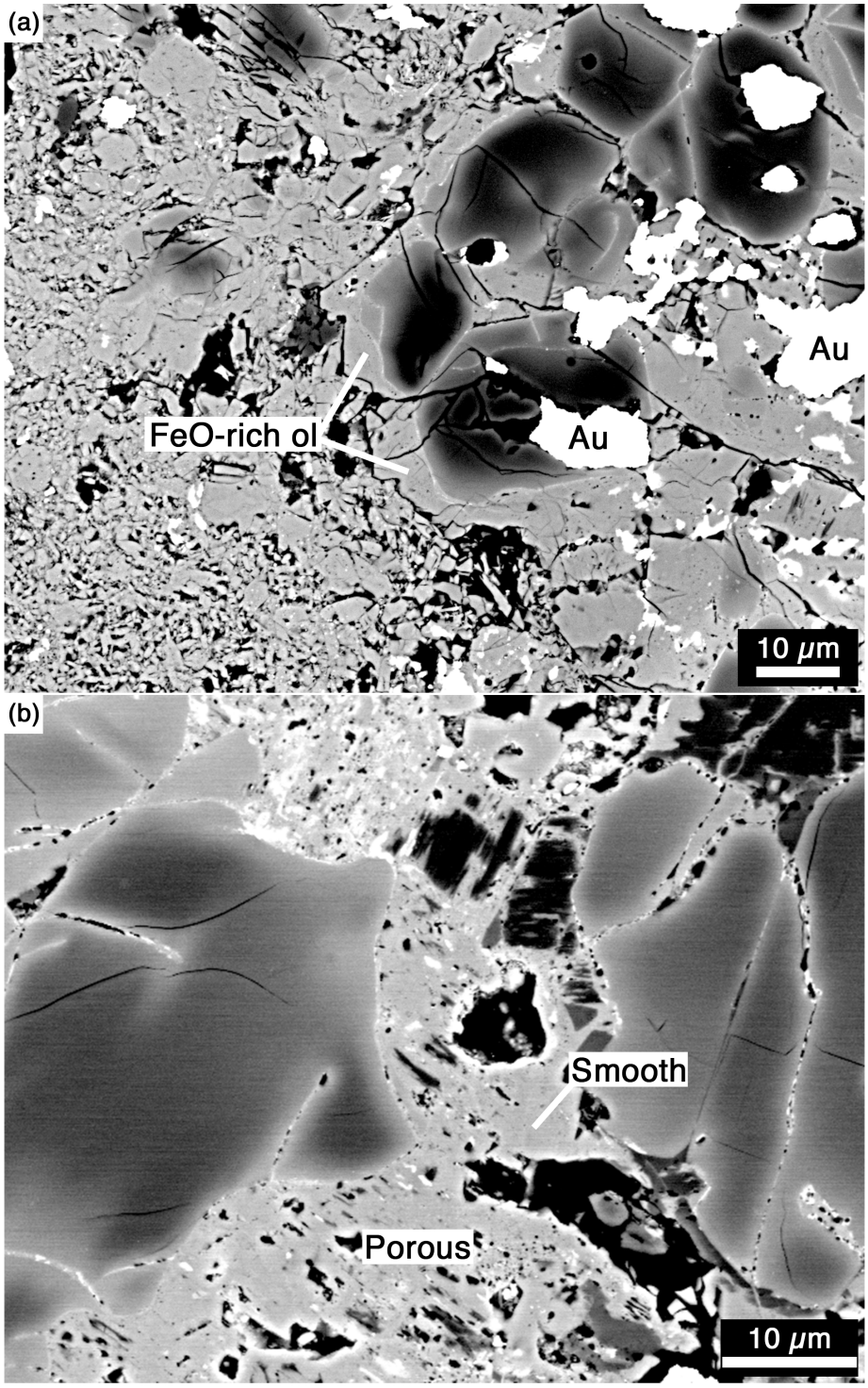

Fig. 12. Back-scattered electron images of boxed area “Fig. 12a” and “Fig. 12b” in Fig. 4. (a) MgO-rich olivine is overgrown by FeO-rich olivine (FeO-rich ol). (b) FeO-rich olivine grains show both porous and smooth textures.

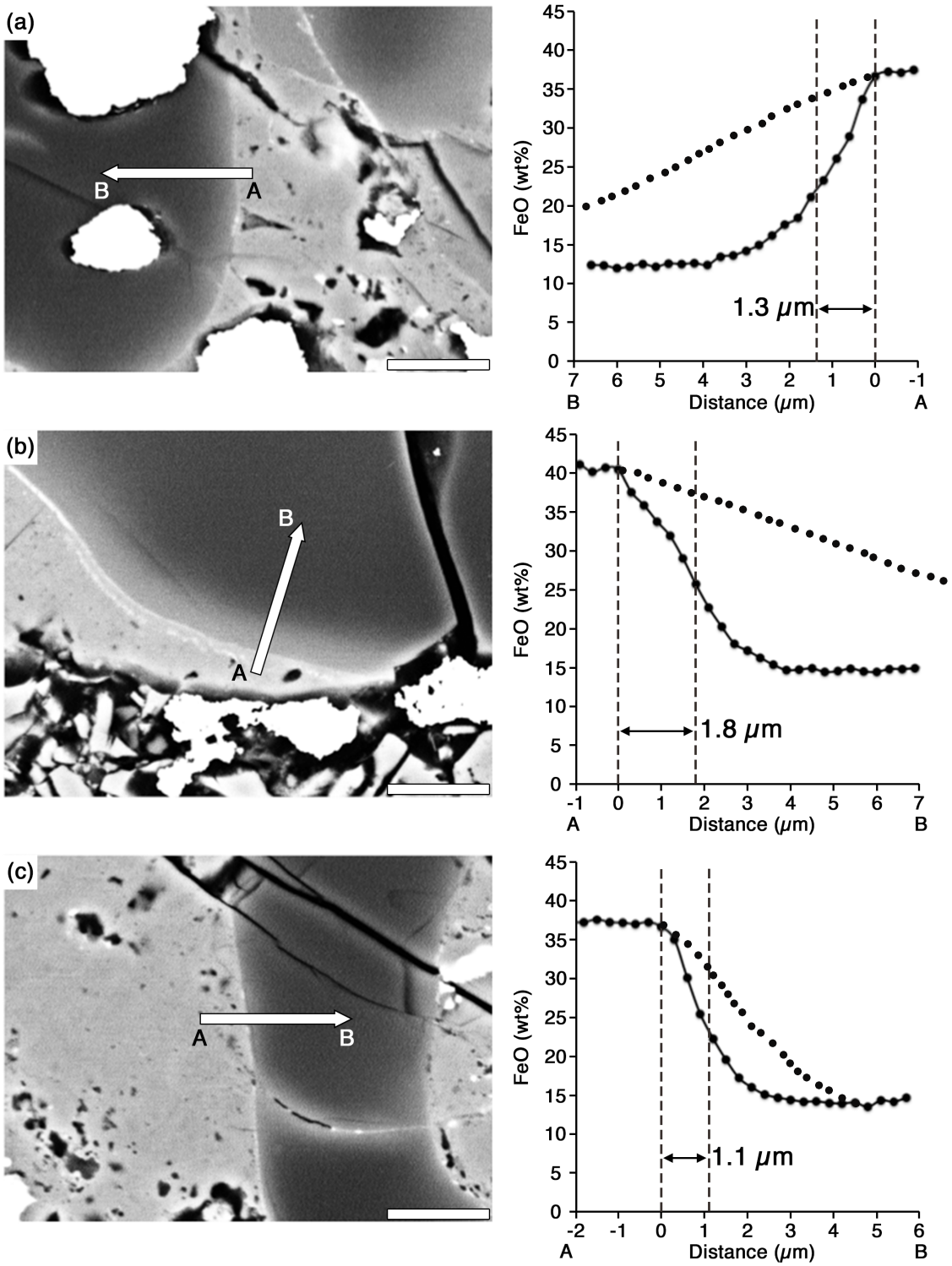

Fig. 13. (a-f) Compositional profiles along a lines crossing the interfaces between FeO-rich olivine (A) and MgO-rich olivine (B). (g–h) Compositional profile across veins in MgO-rich olivine. Interdiffusion distances of the Fe-Mg zoning are shown in diagrams. Hypothetical interdiffusion profiles are shown by dotted lines in each diagram. The hypothetical diffusion is calculated using a spherical body model of constant surface concentration (Crank, 1975). The boundary conditions are as follows: initial concentration is Fa_2 and the final concentration at the center of spherule is Fa_{15}. Measured surface concentration and measured

radius for each olivine are used for calculation. Scale bar is 5 μm.

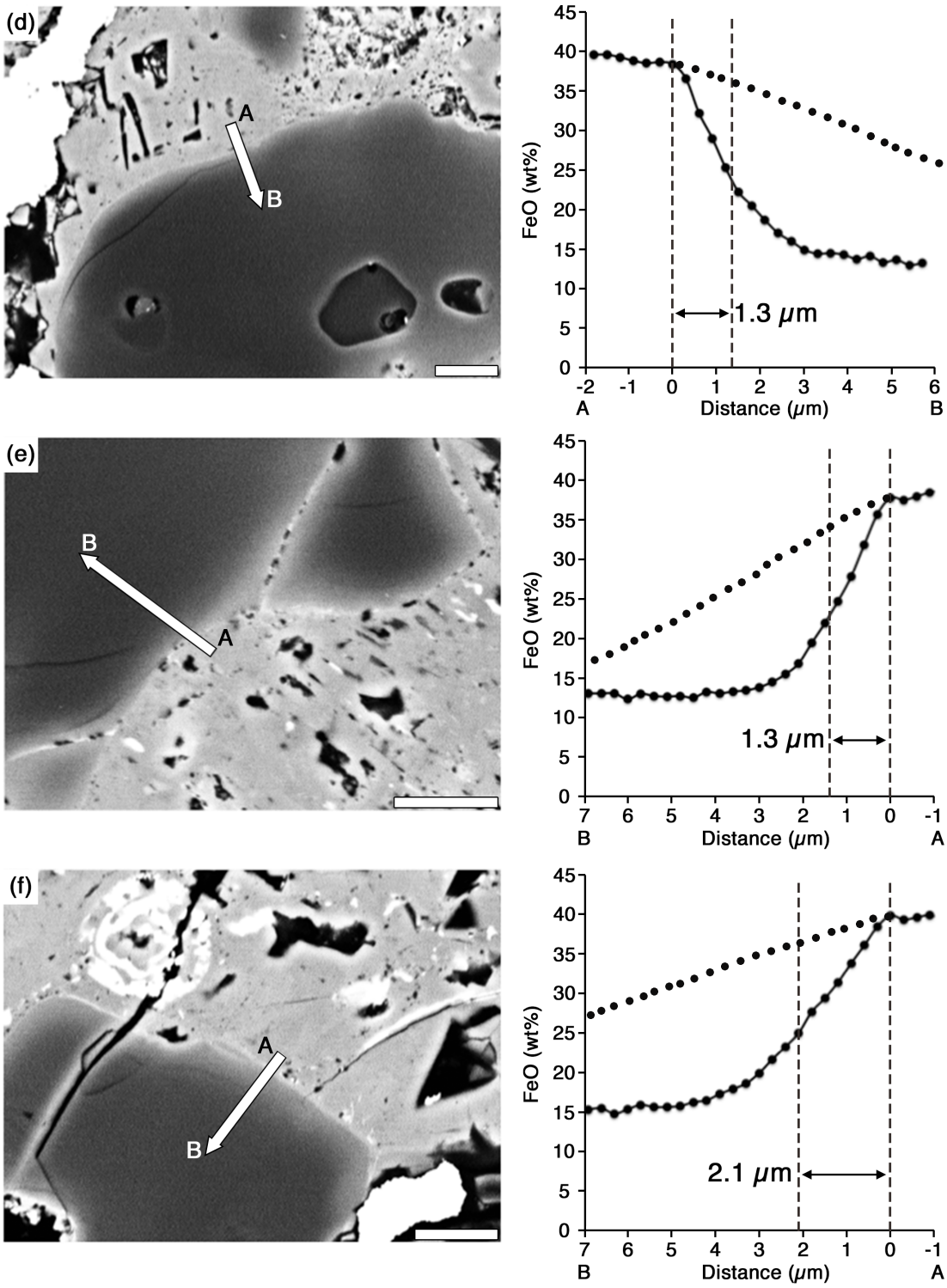

Fig. 13 (continued)

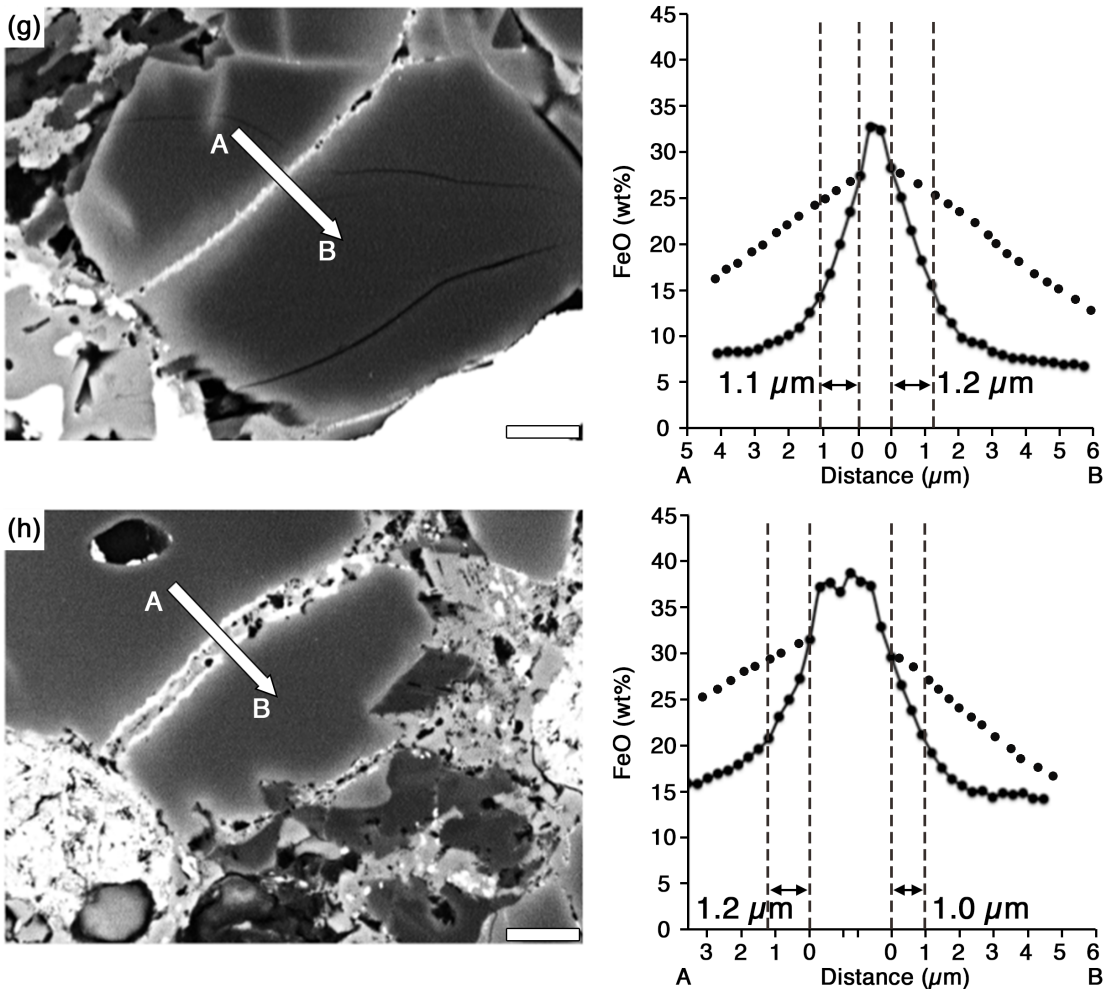

Fig. 13. (continued)

3.1.3 Matrix

The matrix surrounding the igneous rim is predominantly composed of FeO-rich olivine ($Fa_{46–51}$). The olivine composition is similar to the FeO-rich olivine in the igneous rim (Table. 9). The olivine grains show a bimodal size distribution; the coarser-grains (5–10 μm) are either needles-shaped or irregular; the finer-grains (< 1μm) are needle-shaped (Fig. 14a). Neither fayalite (> Fa_{90}) nor phyllosilicates are observed. Sulfides and Ca, Fe-rich silicates are scattered throughout the matrix (Fig. 14b).

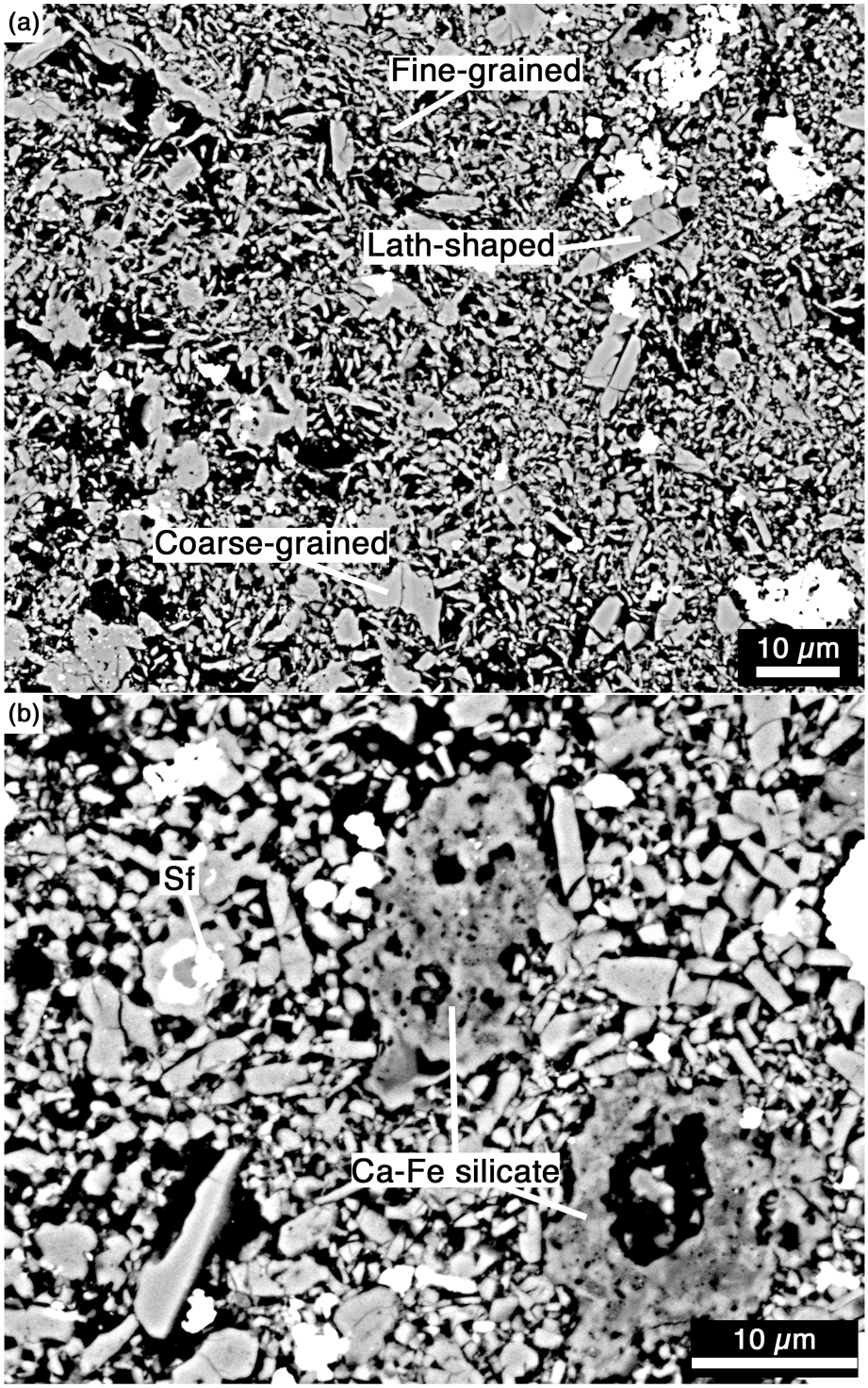

Fig. 14. Back-scattered electron images of matrix. (a) The FeO-rich olivine grains have lash-shaped, coarse-grained and fine-grained morphology. (b) Ca-Fe silicates and sulfide are abundant in matrix.

3.2 Oxygen isotopic compositions of olivine

3.2.1 pot analysis

On the oxygen three-isotope diagram ($\delta^{17}O$ *vs.* $\delta^{18}O$), the composition of olivine phenocrysts in the host chondrule measured by the point analyses plot on a ~ slope-1 line (CCAM) ($\delta^{17}O = -7.6 \pm 2.1‰$, $\delta^{18}O = -3.8 \pm 2.1‰$, 2SD; Fig. 15 and Table 10). The oxygen isotopic compositions of olivines in the igneous rim that were also measured by point analyses are distributed heterogeneously along ~ the slope-1 line (Fig. 15, Table 11 and Fig. A7). The oxygen isotopic compositions of the FeO-rich olivines are ^{16}O-poor ($\delta^{17}O = 2.0 \pm 1.8‰$, $\delta^{18}O = 8.1 \pm 3.6‰$ on average). In contrast, the MgO-rich olivine grains are relatively ^{16}O-rich ($\delta^{17}O = -5.6 \pm 3.2‰$, $\delta^{18}O = -0.7 \pm 3.6‰$ on average). The standard deviations for $\delta^{17}O$ and $\delta^{18}O$ (2SD = 1.8 and 3.6‰, respectively) suggest that the O isotope variation is mass-dependent for the FeO-rich olivine, whereas the variation for MgO-rich olivine appears to be mass-independent with a slope-1 variation (2SD = 3.2 and 3.6‰ for $\delta^{17}O$ and $\delta^{18}O$). One distinct composition ($\delta^{17}O = -18‰$ and $\delta^{18}O = -15‰$) was observed for a MgO-rich olivine grain in the igneous rim. As discussed in the next section, this distinct composition could be a result of a primary beam overlap across areas with two different oxygen isotopic compositions in the MgO-rich olivine, i.e., $\delta^{17}O \sim -6‰$, $\delta^{18}O \sim -1‰$ and $\delta^{17,18}O \sim -30‰$

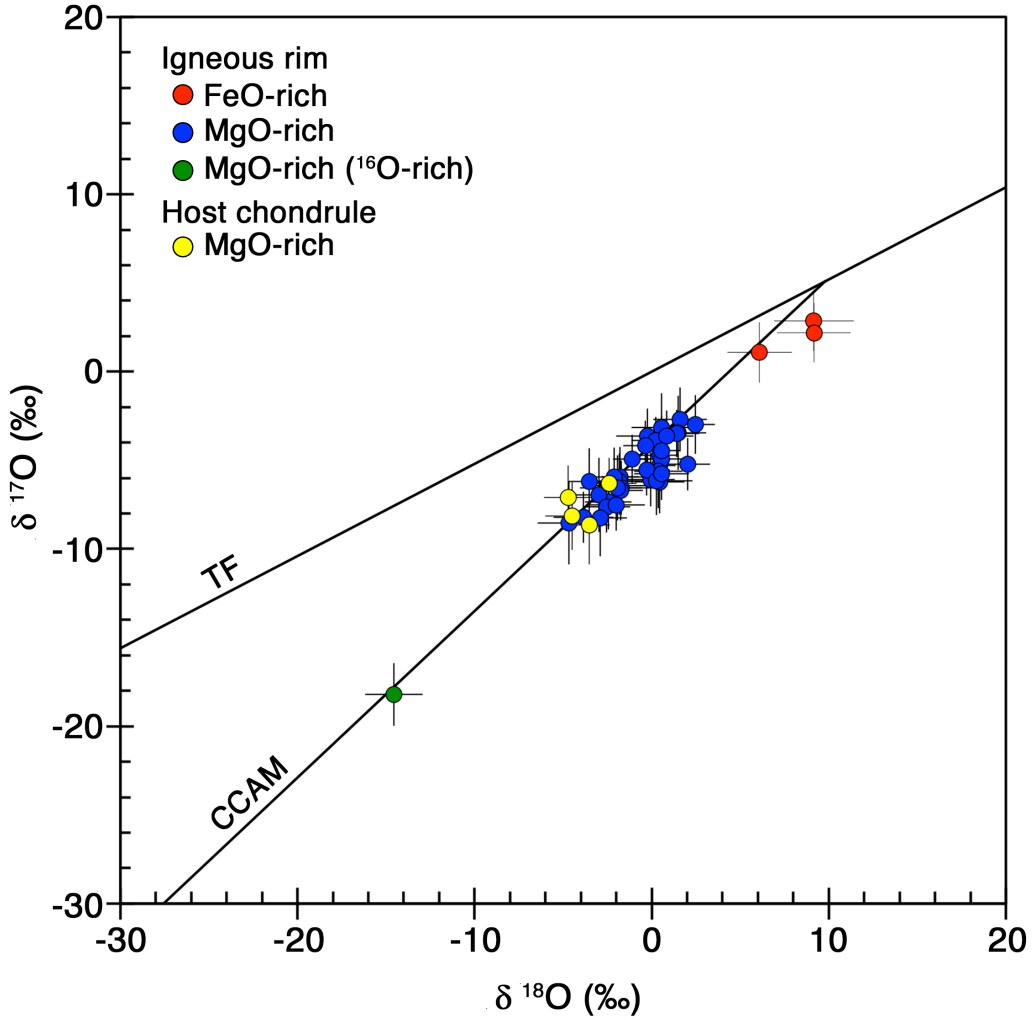

Fig. 15. Oxygen isotopic compositions of olivine in the igneous rim and the host chondrule. Error bar is 2SD. TF: terrestrial fractionation line. CCAM: carbonaceous chondrite anhydrous mineral line.

3.2.1 Isotopograpy

Using isotopography, I discovered that MgO-rich olivine grains in the igneous rim occasionally contain extreme ^{16}O-rich areas in their interiors. The MgO-rich olivine grains containing the extreme ^{16}O-rich areas tend to be present near the boundary between the igneous rim and adjacent matrix, and were not found near the rim-chondrule boundary (Fig. 16).

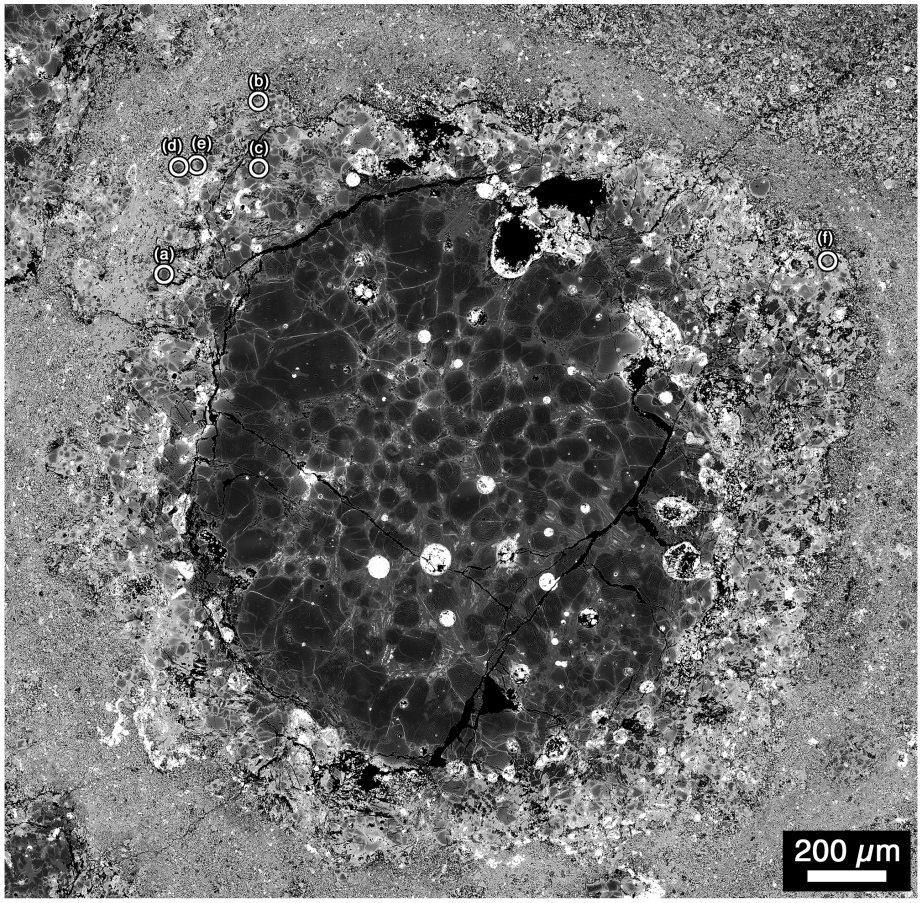

Fig. 16. Distribution of olivine grains containing the extreme ^{16}O-rich areas in the igneous rim. White circles show their positions. The magnified images at locations of circles labeled (a) to (f) show in Fig. 17 with the same labels.

The MgO-rich olivine (about 27 μm in size) in the center of Figure 17a has variable intra-crystalline oxygen-isotope compositions. The oxygen isotopic compositions of MgO-rich olivine in the area that appears dark blue in Figure 7a and the surrounding white - blue area are $\delta^{18}O = -30.6 \pm 3.7‰$ and $-1.9 \pm 2.9‰$, respectively. The extreme ^{16}O-rich area is not chemically distinct from the surrounding MgO-rich olivine. The oxygen isotopic composition of the MgO-rich olivine surrounding the ^{16}O-enriched area is consistent with most of the measured point analyses (i.e., except for the one point analysis with $\delta^{18}O = -14.5‰$; see Fig. 15 and Table 11). The $\delta^{18}O$ for the FeO-rich olivine ($10.4 \pm 3.0‰$) is consistent with those

from point analyses. The ^{16}O-rich analysis shown in Figure 15 ($\delta^{17}O = -18‰$, $\delta^{18}O = -15‰$; analysis number 15 in Table 11) was collected from the boundary between the extreme ^{16}O-rich area and the surrounding olivine (Fig. A7).

The olivine crystal shown in Figure 17b has two different chemical compositions; an upper MgO-rich area and a lower FeO-rich area. The MgO-rich area of the olivine includes an extreme ^{16}O-rich area ($\delta^{18}O = -16.1 \pm 3.3‰$). The upper side of the ^{16}O-rich area directly contacts the MgO-rich olivine, whereas the lower side directly contacts the overgrown FeO-rich olivine. The MgO-rich area of the olivine has Fe-Mg chemical zoning at the boundary with the FeO-rich overgrowth. The $\delta^{18}O$ value in the upper area of the MgO-rich olivine is $-2.3 \pm 3.4‰$. The two different oxygen isotope areas in the MgO-rich olivine are indistinguishable in the chemical compositions. The $\delta^{18}O$ value of the FeO-rich overgrown olivine is $11.1 \pm 3.3‰$.

The MgO-rich olivine (about 27 μm in size; $\delta^{18}O = -2.5 \pm 2.9‰$) in the center of Figure 17c includes two extreme ^{16}O-rich areas. The larger area has $\delta^{18}O$ value of $-33.1 \pm 3.2‰$. These two areas could be connected in three dimensions (above or below the thin section surface) because they have the same crystallographic orientation. A part of the upper boundary of the larger area is directly adjacent to the overgrown FeO-rich olivine (Fig. 3) with $\delta^{18}O$ value of $6.5 \pm 2.6‰$.

The MgO-rich olivine in the center of Figure 17d is about 26 μm in size and partially overgrown by FeO-rich olivine. This olivine includes two extreme ^{16}O-rich areas with $\delta^{18}O$ values of $-30.2 \pm 3.4‰$ and $-28.3 \pm 4.9‰$, respectively. The oxygen isotopic compositions are the same within the measurement error and their crystallographic orientations are also the same. Therefore, these two areas could be one region connected above or below the thin section surface. The surrounding MgO-rich

olivine area has $\delta^{18}O$ value of −1.4 ± 3.1‰ that is typical for the MgO-rich olivine in this igneous rim. The FeO-rich olivine in Figure 17d also has the typical oxygen isotopic composition of $\delta^{18}O$ = 5.9 ± 3.2‰. The olivine grains adjacent to the upper right include two ^{16}O-rich areas with $\delta^{18}O$ values of −15.4 ± 5.1‰ (smaller area) and −24.0 ± 5.0‰ (larger area). Although the olivine grains seem to be FeO-rich, the ^{16}O-rich areas are slightly enriched in MgO composition according to the BSE image suggesting that the extreme ^{16}O-rich areas were originally enriched in MgO. Parts of the FeO-rich olivine outside of the extreme ^{16}O-rich areas have the typical oxygen isotopic composition of FeO-rich olivine in the igneous rim.

The MgO-rich olivine grain ($\delta^{18}O$ = −4.3 ± 2.7‰) on the left side of Figure 17e is about 20 μm in size and includes an extreme ^{16}O-rich area with $\delta^{18}O$ values of −19.8 ± 3.4‰. The MgO-rich olivine is overgrown by FeO-rich olivine with $\delta^{18}O$ value of 6.2 ± 4.0‰. The MgO-rich olivine grain (about 30 μm) on the right side ($\delta^{18}O$ = −1.7 ± 2.7‰) includes an ^{16}O-rich area with $\delta^{18}O$ value of −16.9 ± 3.0‰.

The $\delta^{18}O$ image in Figure 17f was normalized to the SMOW (Standard Mean Ocean Water) scale using the average $\delta^{18}O$ value of the MgO-rich olivine in the rim obtained by spot analyses ($\delta^{18}O$ = −0.7 ± 3.6‰, Table 10) because spot analyses of oxygen isotopes were not applied in this image field. The MgO-rich olivine grain (~35 μm across) is separated by a crack and includes an extreme $\delta^{18}O$ area across the crack ($\delta^{18}O$ = −31.5 ± 4.7‰). The FeO-rich olivine has an oxygen isotopic composition of $\delta^{18}O$ = 12.0 ± 2.0‰.

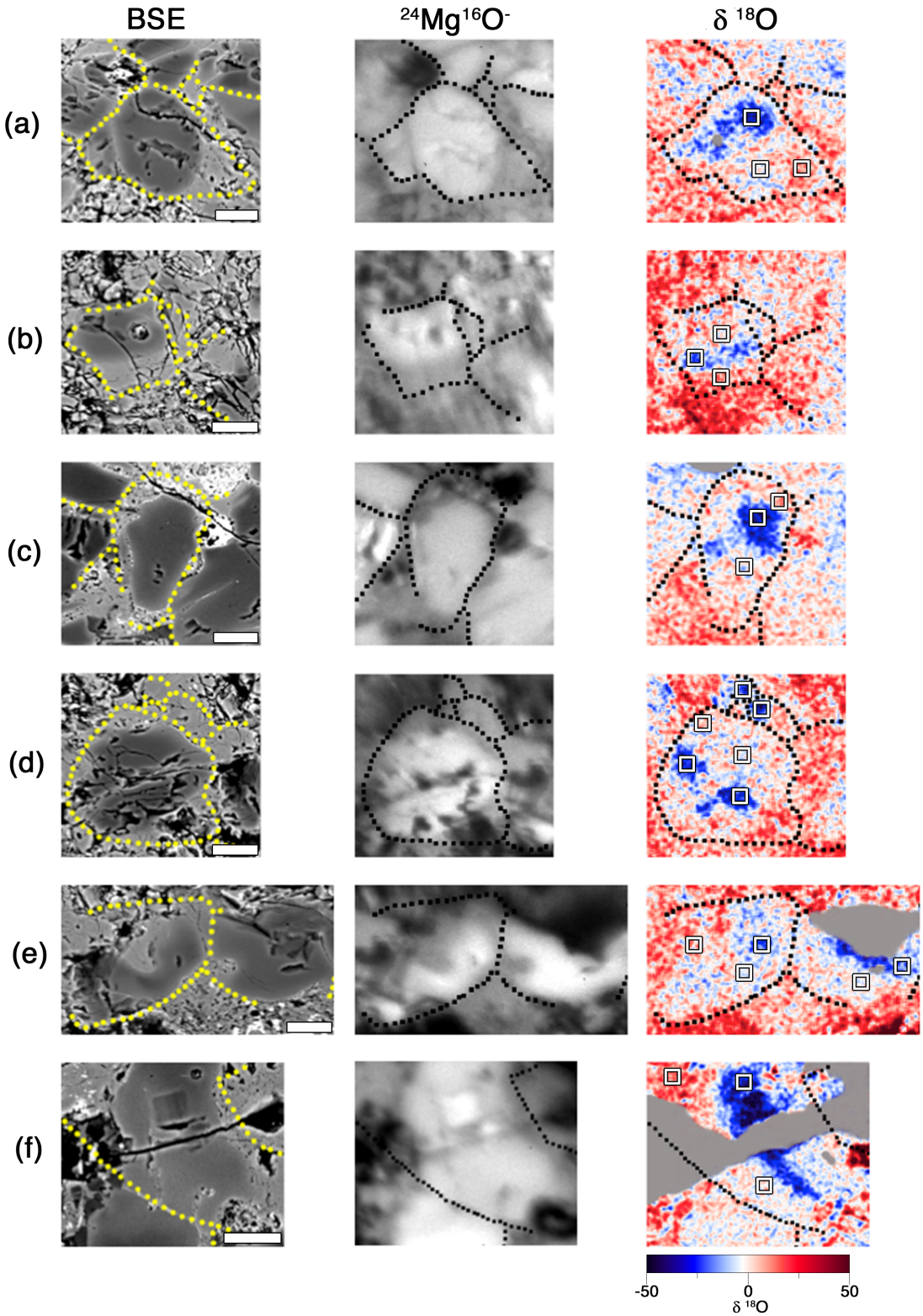

Fig. 17. BSE images, $^{24}Mg^{16}O^-$ and $\delta^{18}O$ isotopograph of olivine containing extreme ^{16}O-rich areas in the igneous rim. Dotted lines represent the grain boundaries determined by EBSD. Scale bar is 10 µm. Areas with artifacts are masked by the gray color. Squares in the $\delta^{18}O$ isotopograph correspond to areas where $\delta^{18}O$ values were calculated (see details in the text).

In summary, most of the oxygen isotopic compositions of the FeO-rich and MgO-rich olivines determined by SCAPS are ~8‰ and ~ −2‰ for $\delta^{18}O$, respectively (Table 12), for all the image fields and these values are consistent with those obtained by the SIMS spot analyses. The MgO rich olivines often include extreme ^{16}O-rich areas with sizes typically less than 10 μm. The oxygen isotopic compositions of the ^{16}O-rich areas are typically $\delta^{18}O \sim -30‰$ (and $\delta^{17}O \sim -30‰$ inferred from combining the results of the point analysis), but tend toward less ^{16}O-rich values for areas having narrow boundaries (<3 μm across) with adjacent ^{16}O-poor olivine. This tendency of oxygen isotopic variation can be interpreted by the spatial resolution of isotopography of this study (Fig. 3), the oxygen self-diffusion discussed in section 4.2, and supports that the ^{16}O-rich areas in this igneous rim have $\delta^{17, 18}O$ values of ~ −30‰.

Chapter 4

DISCUSSION

4.1. Aqueous alteration on the parent body

The occurrences of secondary minerals – FeO-rich olivine (Fa_{40-49}), nepheline, magnetite, and Ca, Fe-rich silicates, and their petrographic textures observed in this study suggest that NWA 3118 experienced extensive aqueous/metasomatic alteration on the CV chondrite parent body (e.g., Krot et al., 1995, 1998, 2004; Maruyama et al., 1999; Maruyama and Yurimoto, 2003; Brearley, 2003). The FeO-rich secondary olivine exhibits textures such as (1) overgrowths around individual MgO-rich olivine grains, (2) veins in the MgO-rich olivine grains, (3) replacement of enstatite and pigeonite, and opaque nodules, and (4) lath-shaped grains in the matrix, which are similar to those observed in the Allende CV_{oxA} chondrite (e.g. Krot et al., 1995, 1998, 2004; Komatsu et al., 2015; Cuvillier et al., 2015) suggesting origin by metasomatic alteration on the CV parent body.

Chemical compositions are different between olivine grains in the igneous rim, $Fa_{\sim 11_22}$, and in the host chondrule, $Fa_{\sim 2_5}$. The characteristics of $Fa_{\sim 11_22}$ might be due to metamorphic processes on the parent body (Huss et al., 2006; Tenner et al., 2015). If the $Fa_{\sim 11_22}$ are the result of metamorphic processes on the parent body, the MgO-rich olivine in the host chondrule in contact with the $Fa_{\sim 11_22}$ olivine also must have similar Fa composition. However, the MgO-rich olivine of the host chondrule has clearly distinct chemical composition, $Fa_{\sim 2_5}$ and the chemical compositions of olivine are abruptly changed at the chondrule-rim boundary (Figs. 7 and A4). If the $Fa_{\sim 11_22}$ are the result of metamorphic processes on the parent body, Fe-Mg interdiffusion

should have occurred in the MgO-rich olivine. I calculated Fe-Mg interdiffusion profiles assuming that Fa composition at the center of olivine grain changed from Fa_2 to Fa_{15} on the parent body. The interdiffusion profiles are inconsistent with compositional zoning in the igneous rim olivine (Fig. 13). Therefore, it is unlikely that the Fa_{11-22} composition of the MgO-rich olivines in the igneous rim was achieved by metamorphic processes on the parent body. The MgO-rich olivines with Fa_{11-22} in the igneous rim are the original composition when the igneous rim formed.

The Fe-Mg chemical zoning between the MgO-rich olivine and adjacent FeO-rich olivine in the igneous rim is an inter-diffusion profiles during the alteration on the parent body, and can be used as a probe to determine timescales and temperature of the alteration (e.g., Weinbruch et al., 1994). I defined the Fe-Mg inter-diffusion distance from the interface ($x_{Fe\text{-}Mg}$ = 0) between the FeO-rich olivine (FeO content = C_1) and MgO-rich olivine (FeO content in the core = C_2) as the distance $x_{Fe\text{-}Mg}$ with the FeO content of $(C_1\text{-}C_2)/e + C_2$ (Fig. 13, Tables 13). For example, in Figue 13a, the Fe-Mg inter-diffusion distance $x_{Fe\text{-}Mg}$ from the FeO-rich olivine with 37 wt% FeO into the MgO-rich olivine with 21 wt% FeO is 1.3 μm. Similarly, the Fe-Mg inter-diffusion distances shown in Figures 13b to 13f are 1.8, 1.1, 1.3, 1.3, and 2.1 μm, respectively.

The diffusion distance from veins of the FeO-rich olivine was also analyzed on both sides across veins into the MgO-rich olivine (Figs. 13g, h). The interface between the vein and MgO-rich olivine is defined as $x_{Fe\text{-}Mg}$ = 0. Diffusion distances of 1.1 μm from 27 wt% FeO to 15 wt% FeO and 1.2 μm from 28 wt% FeO to 15 wt% FeO were obtained on both sides of the vein for the grain shown in Figure 13g.

Similarly, diffusion distances of 1.2 and 1.0 μm were obtained across the vein from 31 to 21 wt% FeO and from 30 to 20 wt% FeO for the grain in Figure 13h.

The interdiffusion distances observed in the olivine grains range from 1.0 μm to 2.1 μm. The longer diffusion distances shown in Figures 13b (1.8 μm) and 13f (2.1 μm) could reflect the anisotropy of Fe-Mg diffusion in olivine that is faster along the c-axis (space group: Pbnm) than along the a- or b-axis (Dohmen and Chakraborty, 2007) although the exact crystal orientation along the diffusion direction was not determined by the EBSD analysis. The Fe-Mg diffusion distance recorded within the MgO-rich olivine in the igneous rim is an average of 1.3 μm regardless of the grain location in the igneous rim (Fig. A4). Our observations of Fe-Mg diffusion agree with those observed in the matrix olivine grains of the Allende CV_{oxA} chondrite (Cuvillier et al., 2015).

The Fe-Mg interdiffusion profiles show that the concentration gradient is present only on the MgO-rich olivine side, not within the overgrown FeO-rich olivine. Cuvillier et al. (2015) proposed that the composition in the FeO-rich olivine is homogeneous because diffusion in FeO-rich olivine is faster than in MgO-rich olivine and the compositional jump derives from resistance that prevents equilibrium at the interface. They also mention that this resistance is not known to occur in olivine grains. Alternatively, the Fe-Mg interdiffusion could have mainly formed in the MgO-rich olivine with dissolved Fe ions in a high-temperature aqueous fluid before precipitation of FeO-rich olivine. The FeO-rich olivine may have precipitated interstitially on the MgO-rich olivine and the intergranular spaces between minerals in the igneous rim after cooling. Fe-Mg diffusion profiles in the Fe-rich olivines, thus, were not appeared due to the slow diffusivity at the low temperature.

The diffusion distances for the Fe-Mg interdiffusion, $x_{\text{Fe-Mg}}$, and O self-diffusion, x_{oxygen}, are approximated as:

$$x_{\text{Fe-Mg}} = \sqrt{2D_{\text{Fe-Mg}}\, t} \quad (2)$$

$$x_{\text{oxygen}} = \sqrt{2D_{\text{oxygen}}\, t} \quad (3)$$

where D is the diffusion coefficient for the corresponding species and t is the time. We ignore the compositional dependence of $D_{\text{Fe-Mg}}$ for simplicity. If these diffusion processes occurred simultaneously in the olivine of the igneous rim, the diffusion distances should be correlated as follows;

$$x_{\text{oxygen}} = x_{\text{Fe-Mg}} \sqrt{\frac{D_{\text{oxygen}}}{D_{\text{Fe-Mg}}}} \quad (4)$$

The average $x_{\text{Fe-Mg}}$ is 1.3 μm in this study and x_{oxygen} is then given as a function of temperature independently from the diffusion time (duration of aqueous alteration). The Fe-Mg inter-diffusion and oxygen self-diffusion coefficients in olivine have been measured in several previous studies. Nakamura and Schmalzried (1984) determined the Fe-Mg inter-diffusion coefficient ($D_{\text{N\&S}}$) at temperatures between 1323 and 1553 K and a composition of Fo_{87}. Chacraborty (1997) also reported the Fe-Mg inter-diffusion coefficient (D_C) at temperatures between 1253 and 1573 K and a composition of Fo_{86}. Their diffusion coefficients were obtained under a controlled oxygen fugacity of $fO_2 = 10^{-12}$ bars. Dohmen et al. (2007) determined the Fe-Mg interdiffusion coefficients of Fo_{86} at temperatures from 973–1473 K. The diffusion coefficients were obtained at fO_2 of 10^{-12} bars at temperatures between 1173–1473 K ($D_{\text{D_hightemp}}$), while those between 973–1123 K were obtained at fO_2 of 10^{-15}–10^{-17} bars ($D_{\text{D_lowtemp}}$). The forsterite content of the MgO-rich olivine in the

igneous rim is adequate to choose these Fe-Mg interdiffusion coefficients in previous studies. However, they need to be extrapolated to lower temperatures because they were determined at temperatures higher than peak metamorphic temperatures inferred for Allende (e.g., Keil, 2000; Ito and Messenger, 2010) and were extrapolated down to 500 K in this study. The Fe-Mg inter-diffusion coefficients (m^2/s), $D_{N\&S}$ (Nakamura and Schmaizried, 1984), D_C (Chakraborty et al., 1997), $D_{D_hightemp}$ (Dohmen et al., 2007), and $D_{D_lowtemp}$ (Dohmen et al., 2007) were expressed as follows:

$$D_{N\&S} = 8.33\times10^{-10} \cdot \exp\left[\frac{-188000}{RT}\right] \quad (5)$$

$$D_C = 5.38\times10^{-9} \cdot \exp\left[\frac{-226000}{RT}\right] \quad (6)$$

$$D_{D_hightemp} = 6.66\times10^{-10} \cdot \exp\left[\frac{-201000}{RT}\right] \quad (7)$$

$$D_{D_lowtemp} = 1.54\times10^{-9} \cdot \exp\left[\frac{-223000}{RT}\right] \quad (8)$$

where T is the temperature (K) and R is the gas constant (8.314 J/mol·K).

The oxygen fugacity, fO_2, for the CV chondrites was estimated to be close to the iron-wustite (IW) oxygen buffer during chondrule formation and close to the fayalite-magnetite-quartz (FMQ) buffer during aqueous alteration (Righeter and Neff, 2007). I assumed that the diffusion occurred under the FMQ buffer during aqueous alteration that is expressed as follows (Myers and Eugster, 1983);

$$\log fO_2 = -\frac{24441.9}{T} + 8.290 \quad (9)$$

The fO_2 corrections for $D_{N\&S}$, D_C, and $D_{D_hightemp}$ to the FMQ were performed assuming that the Fe-Mg interdiffusion is controlled by the vacancy concentration determined by the Fe^{2+}- Fe^{3+} equilibrium in olivine (e.g., Chakraborty et al., 1997). The fO_2 corrected expressions for $D_{Fe\text{-}Mg}$ are given as follows:

$$D_{N\&S} = \left(\frac{fO_{2_}FMQ}{fO_{2_}Ex}\right)^{\frac{1}{6}} \cdot 8.33\times10^{-10} \cdot \exp\left[\frac{-188000}{\mathrm{R}T}\right] \quad (10)$$

$$D_C = \left(\frac{fO_{2_}FMQ}{fO_{2_}Ex}\right)^{\frac{1}{6}} \cdot 5.38\times10^{-9} \cdot \exp\left[\frac{-226000}{\mathrm{R}T}\right] \quad (11)$$

$$D_{D_hightemp} = \left(\frac{fO_{2_}FMQ}{fO_{2_}Ex}\right)^{\frac{1}{6}} \cdot 6.66\times10^{-10} \cdot \exp\left[\frac{-201000}{\mathrm{R}T}\right] \quad (12)$$

where fO_2_FMQ is the oxygen fugacity at the FMQ buffer and fO_2_Ex is that in the experiments. Dohmen et al. (2007) reported that Fe-Mg interdiffusion at low temperatures (below 1173 K) are independent of fO_2, most likely due to a change in the diffusion mechanism where the vacancy concentration is controlled extrinsically by the impurity ions. Thus, the fO_2 correction was not made for $D_{\mathrm{D_lowtemp}}$.

The oxygen self-diffusion coefficients (m^2/s) in olivine, $D_{\mathrm{J_1980}}$ (Jaoul et al., 1980), D_{Re} (Reddy et al., 1980), $D_{\mathrm{J_1983}}$ (Jaoul et al., 1983), $D_{\mathrm{o\&A}}$ (Oishi and Ando, 1984; Ando et al., 1981), D_{A} (Andresson et al., 1989), $D_{\mathrm{G\&J}}$ (Gérard and Jaoul, 1989), D_{Ry} (Ryerson et al., 1989) and $D_{\mathrm{D_2002}}$ (Dohmen et al., 2002) are expressed as follows:

$$D_{\mathrm{J_1980}} = 1.46\times10^{-8} \cdot \exp\left[\frac{-328000}{\mathrm{R}T}\right] \quad (13)$$

$$D_{\mathrm{Re}} = 3.50\times10^{-7} \cdot \exp\left[\frac{-372000}{\mathrm{R}T}\right] \quad (14)$$

$$D_{\mathrm{J_1983}} = 2.30\times10^{-10} \cdot \exp\left[\frac{-293000}{\mathrm{R}T}\right] \quad (15)$$

$$D_{\mathrm{O\&A}} = 2.85\times10^{-6} \cdot \exp\left[\frac{-416000}{\mathrm{R}T}\right] \quad (16)$$

$$D_{\mathrm{A}} = 6.86\times10^{-10} \cdot \exp\left[\frac{-302000}{\mathrm{R}T}\right] \quad (17)$$

$$D_{\mathrm{G\&J}} = 6.7\times10^{-6} \cdot (fO_{2_}FMQ)^{0.34} \cdot \exp\left[\frac{-38000}{T}\right] \quad (18)$$

$$D_{\mathrm{Ry}} = 2.6\times10^{-10} \cdot (fO_2_FMQ)^{0.21} \cdot \exp\left[\frac{-226000}{\mathrm{R}T}\right] \quad (19)$$

$$D_{\mathrm{D_2002}} = 4.57\times10^{-9} \cdot \exp\left[\frac{-338000}{\mathrm{R}T}\right] \quad (20)$$

The diffusivities given by Eqs. (13–17) are independent of fO_2 because they were determined for pure forsterite, and the oxygen fugacity dependence was not determined for $D_{\mathrm{D_2002}}$. I applied all the combinations of $D_{\mathrm{Fe\text{-}Mg}}$ given by Eqs. (8) and (10–12) and D_{oxygen} given by Eqs. (13–20) to Eq. (4) to calculate the possible range of x_{oxygen} for a given $x_{\mathrm{Fe\text{-}Mg}}$ of 1.3 μm.

Figure 18 shows the change of x_{oxygen} with temperature. The x_{oxygen} is widespread over the range from 10^{-7} nm to 0.1 μm at temperatures below 1000 K. Because the parent body of the $\mathrm{CV_{oxA}}$ chondrite was not heated above 1000 K (e.g. Keil, 2000; Ito and Messenger, 2010), x_{oxygen} should be smaller than 0.1 μm. Therefore, the oxygen isotopic compositions in the olivine of NWA3118 should not have been disturbed on the parent body except for a very thin layer (< 0.1μm) of the grain boundary. Because the thickness of the possible oxygen diffusion layer is much smaller than the spatial resolution of the oxygen isotopography (Fig. 3), the thin layer was not observed in this study.

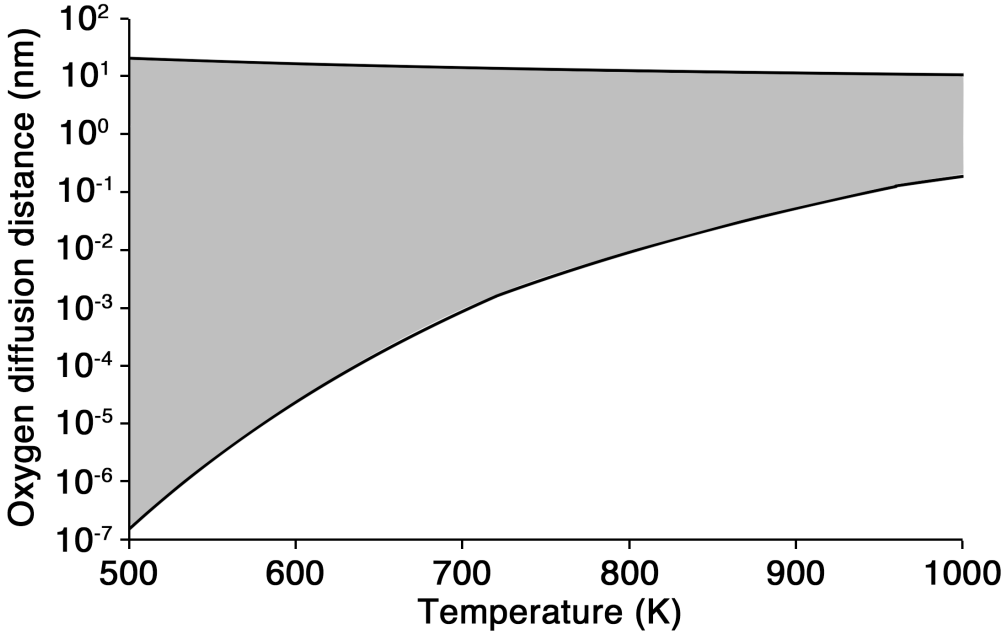

Fig. 18. Range of oxygen self-diffusion distance (nm) as a function of temperature (K) at Fe-Mg inter-diffusion distance of 1.3 μm.

4.2. Oxygen diffusion in MgO-rich olivine

Figure 19 shows the $\delta^{18}O$ profiles at the edge of the extreme ^{16}O-rich area in a MgO-rich olivine single crystal within the igneous rim. The sharpness of the boundary defined by 2SD, a width between 16% and 84% of the compositional difference, is 1.5–2.3 μm. This value is larger than the spatial resolution of the isotopography (0.8 μm, Fig. 3). This indicates that oxygen isotope self-diffusion (~1 μm, Table 14) occurred in the MgO-rich olivine across the boundary between the different oxygen isotopic compositions prior to the parent body accretion. The oxygen isotope self-diffusion distance of ~1 μm may also explain the observation that the oxygen isotopic compositions in the extreme ^{16}O-rich areas tend toward ^{16}O-depletion when the area is smaller than 3 μm across the short side (Fig. 17).

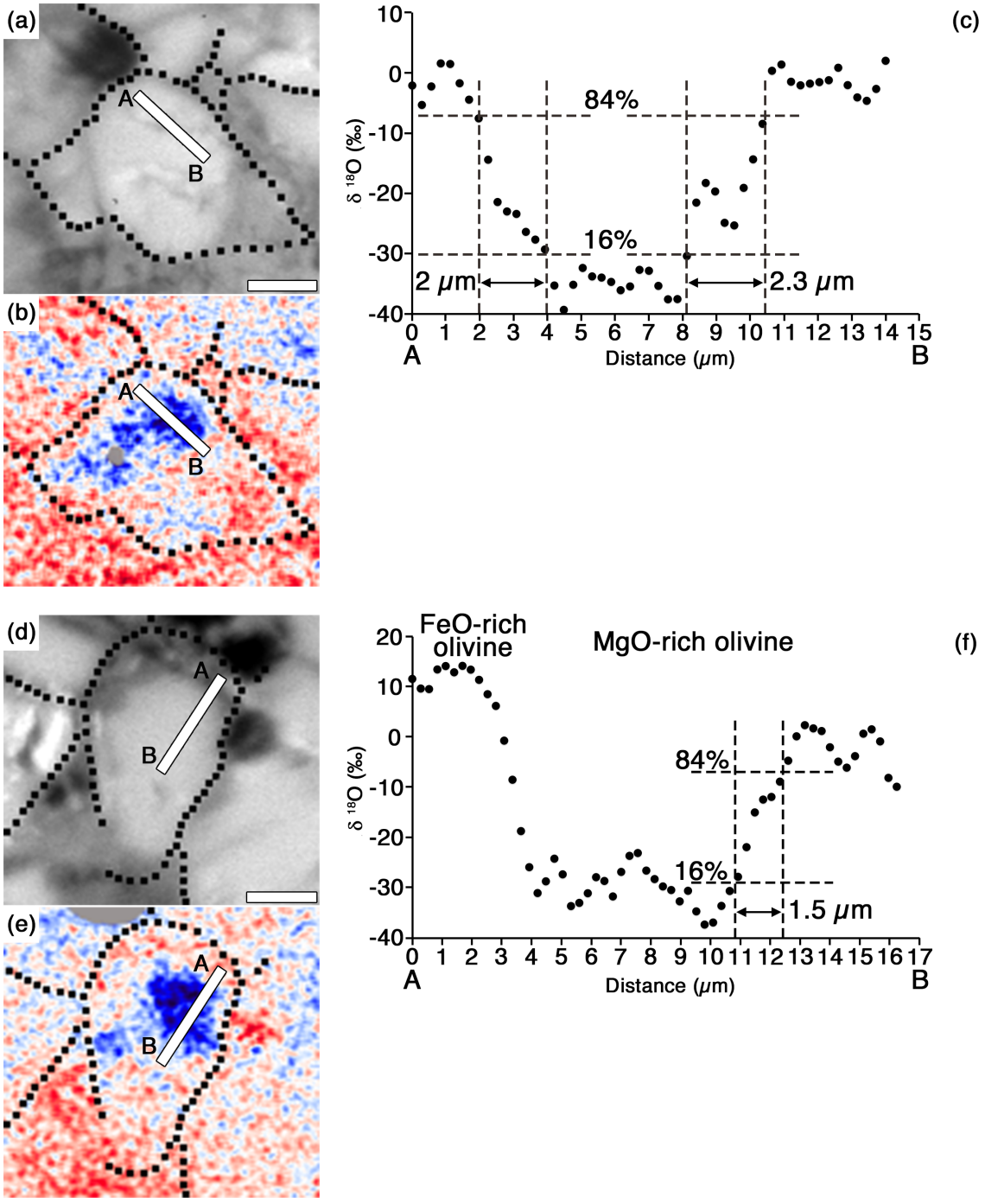

Fig. 19. (a and d) $^{24}Mg^{16}O^{-}$ isotopographs; (b and e) $\delta^{18}O$ isotopograph; (c and f) $\delta^{18}O$ profiles of lines A-B. Scale bar is 10 μm.

Because the MgO-rich olivine of the igneous rim was crystallized from a melt and the extreme ^{16}O-rich areas in the MgO-rich olivine should have been relict crystals in the melt, oxygen isotope exchanges in the ^{16}O-rich areas should have

principally occurred during the igneous rim formation through oxygen self-diffusion in the MgO-rich olivine. I note that forsterite dissolution occurred during the igneous-rim formation from the irregular shapes of extreme ^{16}O-rich areas and forsterite dissolution in chondrule-like melts is a very fast process (Soulié et al. 2017). This suggests that forsterite dissolution might not be a significant effect for the oxygen isotope self-diffusion.

Because the fO_2 during chondrule formation was estimated to be close to the iron-wustite (IW) oxygen buffer (Righeter and Neff, 2007), I assumed that the diffusion occurred under the IW buffer (IW~0) as follows (Myers and Eugster, 1983);

$$\log fO_2 = -\frac{26834.7}{T} + 6.471 \quad (21)$$

I note that chondrule formed under the oxygen fugacity was one or two log units below IW (IW-1–IW-2) (Grossman et al., 2012). This diffusion in fO_2 has no influence on our calculation, even if fO_2 is 2 orders of magnitude (IW-2) lower than our assumption (IW~0). Because our data were normalized to an fO_2 using an exponent of 1/6 for fO_2 dependence of Fe-Mg inter-diffusion in olivine (Dohmen et al., 2007). That is, only an exponent of 1/6 difference affects a diffusion coefficient. Furthermore, the Fe-Mg diffusion distance is proportional to the square root of a diffusion coefficient, indicating the effect of oxygen fugacity difference is not significantly large. The $D_{Fe\text{-}Mg}$ corrected to the IW fO_2 are expressed as follows:

$$D_{N\&S} = \left(\frac{fO_{2_}IW}{fO_{2_}Ex}\right)^{\frac{1}{6}} \cdot 8.33\times10^{-10} \cdot \exp\left[\frac{-188000}{RT}\right] \quad (22)$$

$$D_C = \left(\frac{fO_{2_}IW}{fO_{2_}Ex}\right)^{\frac{1}{6}} \cdot 5.38\times10^{-9} \cdot \exp\left[\frac{-226000}{RT}\right] \quad (23)$$

$$D_{D_hightemp} = \left(\frac{fO_2_IW}{fO_2_Ex}\right)^{\frac{1}{6}} \cdot 6.66\times10^{-10} \cdot \exp\left[\frac{-201000}{\mathrm{R}T}\right] \quad (24)$$

The fO$_2$_IW in the equations is the oxygen fugacity at the IW buffer and the fO$_2$_Ex is the oxygen fugacity in the experiment described above (see details in section 4.1).

The Fe-Mg interdiffusion coefficients in olivine at high temperatures (1673-1873 K) were also determined by Tachibana et al. (2013). The diffusion coefficient was obtained under a controlled fO$_2$ of $10^{-7.5}$ bars and Fo$_{95}$ composition:

$$D_{\mathrm{T}} = 4.84\times10^{-5} \cdot \exp\left[\frac{-323000}{\mathrm{R}T}\right] \quad (25)$$

The diffusion coefficient (m^2/s) after the fO$_2$ correction to IW is given by:

$$D_T = \left(\frac{fO_2_IW}{fO_2_Ex}\right)^{\frac{1}{6}} \cdot 4.84\times10^{-5} \cdot \exp\left[\frac{-323000}{\mathrm{R}T}\right] \quad (26)$$

I calculated the $x_{\mathrm{Fe\text{-}Mg}}$ in olivine for x_{oxygen} = 1 μm using Eq. (4). The $x_{\mathrm{Fe\text{-}Mg}}$ decreases with increasing temperature (Fig. 20) and is estimated to be larger than 10 μm for all the combinations of $D_{\mathrm{Fe\text{-}Mg}}$ and D_{oxygen} up to 2000 K that is an inferred peak temperature of chondrule formation (e.g., Hewins and Connolly, 1996; Hewins et al., 2005).

Because the size of the extreme ^{16}O-rich areas in this study were less than 10 μm across (Fig. 17), the calculated $x_{\mathrm{Fe\text{-}Mg}}$ is large enough to homogenize the Fe-Mg distribution between the ^{16}O-rich areas and the surrounding overgrown MgO-rich olivine. This is consistent with the observations of the homogenous chemical compositions of the MgO-rich olivines with different oxygen isotopic compositions.

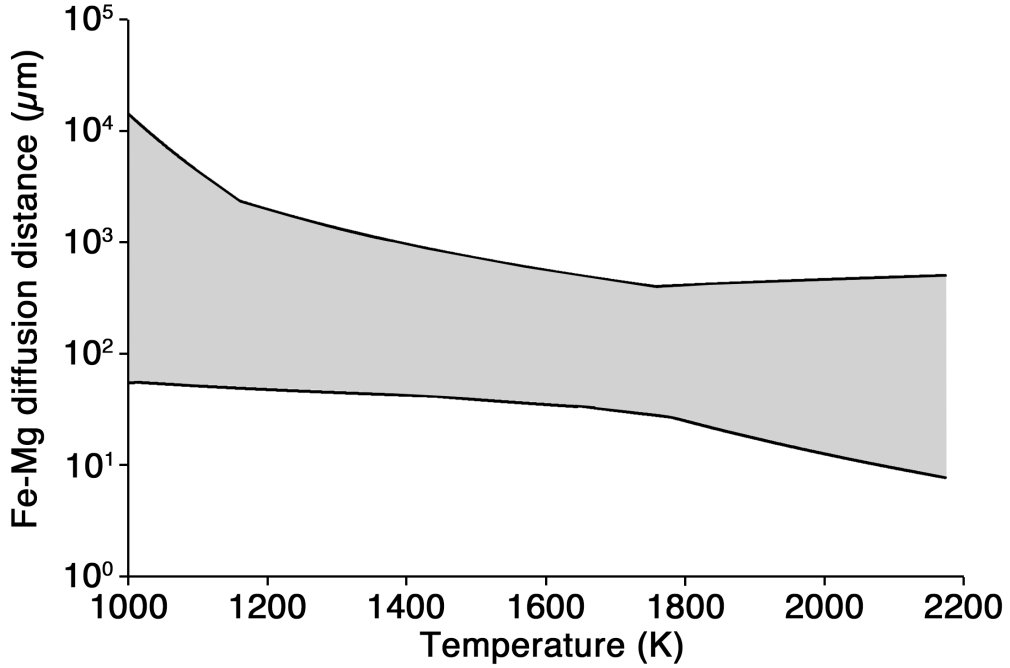

Fig. 20. Range of Fe-Mg interdiffusion distance (μm) as a function of temperature (K) at oxygen self-diffusion distance of 1 μm.

The heating duration for x_{oxygen} = 1 μm within the MgO-rich olivine in the igneous rim was calculated to be from several hours to several days at near liquidus temperature (2000 K) and longer than one year at near solidus temperature (1400 K) (Fig. 21). The estimated heating duration was similar to those for chondrule formation at near liquidus temperature that was molten for up to several tens of hours (e.g., Hewins and Connolly, 1996; Hewins et al., 2005) suggesting that the igneous rim was also formed during transient heating events.

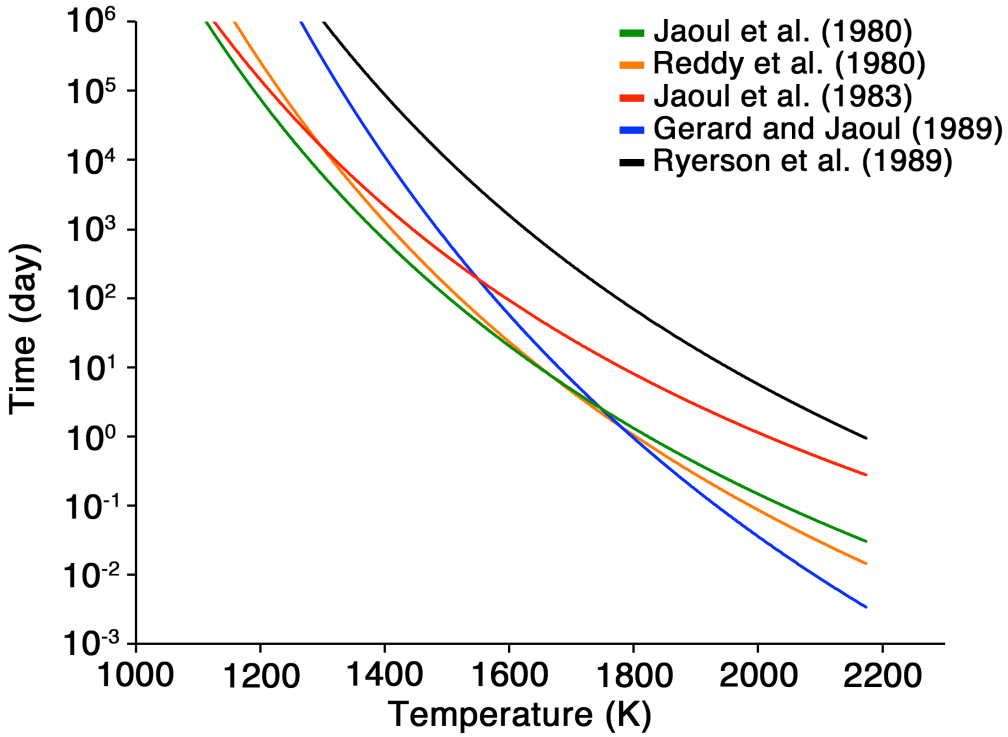

Fig. 21. Range of heating time (day) as a function of temperature (K) at oxygen self-diffusion distance of 1 μm.

Chapter 5

CONCLUSIONS

The igneous rim surrounding a type I chondrule in the Northwest Africa 3118 CV_{oxA} chondrite mainly consists of two types of olivine with MgO-rich (Fa_{11-22}) and FeO-rich (Fa_{40-49}) compositions. The igneous rim contains secondary minerals that were formed by aqueous alteration on the CV chondrite parent body, including FeO-rich olivine, nepheline, and Fe-Ni sulfides.

The oxygen isotopic composition of the FeO-rich olivine ($\delta^{17}O$ = 2.0 ± 1.8‰, $\delta^{18}O$ = 8.1 ± 3.6‰, 2SD), the mass-dependent isotope fractionation, and the porous texture filling between the MgO-rich olivine grains indicate that the FeO-rich olivine precipitated from an ^{16}O-poor aqueous fluid on the CV chondrite parent body. The MgO-rich olivine shows Fe-Mg chemical zoning at the interface with the FeO-rich olivine, indicating that Fe-Mg inter-diffusion occurred during the aqueous alteration on the parent body. The inter-diffusion distance indicates that the oxygen isotopic composition of the MgO-rich olivine ($\delta^{17}O$ = −5.6 ± 3.2‰, $\delta^{18}O$ = −0.7 ± 3.6‰) was not disturbed on the parent body and should preserve the rim formation events in the solar nebula.

The MgO-rich olivine includes distinctly extreme ^{16}O-rich areas ($\delta^{17, 18}O$ = ~ −30‰). These areas are anhedral and less than 10 μm across, indicating that they represent relict grains that survived the igneous rim formation event. The oxygen diffusion distance of about 1 μm in the extreme ^{16}O-rich area constrains that the heating duration of the igneous rim formation was from several hours to several days at about 2000 K, suggesting flash heating events similar to chondrule formation

formed the igneous rim. The MgO-rich olivine grains with $\delta^{18}O$ values of ~ −1‰ overgrew on the extreme ^{16}O-rich relict olivine grains during igneous rim formation.

Table 1. Chemical composition of olivine in the chondrule. Measurement positions are shown in Figure A1.

	#1	#2	#3	#4	#5	#6	#7	#8	#9	#10	#11	#12	#13
Wt.%													
MgO	54.7	54.6	54.4	54.8	54.9	54.5	52.6	53.4	53.8	54.5	55.3	54.8	53.6
SiO_2	42.5	42.6	42.7	43.1	42.3	42.2	42.1	42.1	42.1	42.2	42.8	42.4	42.3
CaO	0.3	n.d.	n.d.	0.3	n.d.	n.d.	0.5	0.3	0.3	n.d.	0.4	0.4	n.d.
Cr_2O_3	n.d.	n.d.	n.d.	n.d.	n.d.	n.d.	n.d.	n.d.	0.3	0.5	n.d.	0.4	n.d.
FeO	2.3	2.6	3.4	2.5	2.2	2.9	4.8	3.7	3.2	2.2	1.6	2.1	4.6
Total	99.8	99.8	100.6	100.7	99.4	99.6	100.0	99.5	99.7	99.4	100.2	100.0	100.5
Cations													
Mg	1.93	1.93	1.91	1.92	1.95	1.93	1.88	1.90	1.91	1.93	1.94	1.93	1.90
Si	1.01	1.01	1.01	1.01	1.01	1.00	1.01	1.01	1.00	1.01	1.01	1.00	1.01
Ca	0.01	n.d.	n.d.	0.01	n.d.	n.d.	0.01	0.01	0.01	n.d.	0.01	0.01	n.d.
Cr	n.d.	n.d.	n.d.	n.d.	n.d.	n.d.	n.d.	n.d.	0.01	0.01	n.d.	0.01	n.d.
Fe	0.04	0.05	0.07	0.05	0.04	0.06	0.10	0.07	0.06	0.04	0.03	0.04	0.09
Total	2.99	2.99	2.99	2.99	3.00	2.99	3.00	2.99	2.99	2.99	2.99	2.99	3.00
Oxygen	4	4	4	4	4	4	4	4	4	4	4	4	4
Fa, mol%	2.0	2.5	3.5	2.5	2.0	3.0	5.1	3.6	3.0	2.0	1.5	2.0	4.5

n.d.: not detected.

Table 2. Chemical composition of nepheline (Nep), plagioclace (plag) and Augite (Aug) in the chondrule. Measurement positions are shown in Figure A2.

	Nph #1	Plag #2	Aug #3
Wt.%			
Na_2O	17.3	2.6	n.d.
MgO	n.d.	0.9	18.6
Al_2O_3	34.6	29.8	3.9
SiO_2	43.2	49.9	51.9
K_2O	1.8	n.d.	n.d.
CaO	2.6	15.3	20.4
TiO_2	n.d.	n.d.	1.5
Cr_2O_3	n.d.	n.d.	1.2
FeO	0.3	1.2	0.8
Total	100.0	99.7	98.3
Cations			
Na	1.59	0.23	n.d.
Mg	n.d.	0.06	1.01
Al	1.93	1.62	0.17
Si	2.05	2.30	1.89
K	0.11	n.d.	n.d.
Ca	0.13	0.76	0.80
Ti	n.d.	n.d.	0.04
Cr	n.d.	n.d.	0.04
Fe	0.01	0.04	0.02
Total	5.82	5.01	3.97
Oxygen	8	8	6

n.d.: not detected.

Table 3. Chemical composition of Fe-Ni metal (Mt), magnetite (Mgt) and sulfide (Sf) in the chondrule. Measurement positions are shown in Figure A3.

	Mt #1	Mt #2	Mt #3	Mt #4	Mt #5	Mt #6	Mt #7
Cr	n.d.	n.d.	n.d.	0.3	0.4	n.d.	n.d.
Fe	30.3	29.9	31.3	30.0	30.3	31.1	31.2
Ni	68.5	67.9	67.9	68.1	67.5	66.6	67.0
Total	98.8	97.8	99.2	98.4	98.2	97.7	98.2

	Mgt #8	Mgt #9	Mgt #10	Mgt #11	Mgt #12	Mgt #13	Mgt #14	Mgt #15	Mgt #16	Mgt #17
MgO	0.4	0.5	0.3	0.3	0.3	0.3	0.6	0.3	0.4	0.5
Al_2O_3	0.9	1.0	0.9	0.9	0.8	0.9	0.8	1.0	1.1	1.0
TiO_2	n.d.	n.d.	n.d.	n.d.	n.d.	n.d.	n.d.	n.d.	0.3	n.d.
SiO_2	0.2	n.d.	0.2	n.d.	0.3	0.3	0.4	0.2	n.d.	0.3
CaO	n.d.	n.d.	n.d.	n.d.	0.3	n.d.	0.2	n.d.	n.d.	n.d.
Cr_2O_3	1.0	0.7	0.9	1.5	1.5	1.4	3.0	1.9	2.2	1.5
Total FeO	91.0	91.1	91.7	90.3	90.5	90.3	87.7	89.0	88.0	90.3
FeO*	30.8	30.5	31.3	30.6	30.9	31.0	30.4	30.7	30.5	31.0
Fe_2O_3*	66.8	67.4	67.1	66.4	66.2	65.9	63.7	64.8	63.9	66.0
NiO	n.d.	n.d.	n.d.	n.d.	n.d.	n.d.	1.2	n.d.	n.d.	n.d.
Total	93.4	93.3	93.9	93.1	93.7	93.2	93.9	92.5	92.0	93.7
Total*	100.1	100.0	100.6	99.7	100.4	99.8	100.3	98.9	98.4	100.3

* FeO and Fe_2O_3 in magnetite were calculated assuming stoichiometry.

Total* is used FeO* and Fe_2O_3* instead of Total FeO.

Table 3. (continued)

	Sf #18	Sf #19
S	33.4	33.3
Fe	62.7	63.7
Total	96.1	97.0

n.d.: not detected.

Table 4. Chemical composition of olivine in the igneous rim. Measurement positions are shown in Figure A4.

	#1	#2	#3	#4	#5	#6	#7	#8	#9	#10	#11	#12	#13	#14	#15
Wt.%															
MgO	46.7	46.7	43.3	46.8	47.5	40.8	47.1	41.9	28.5	25.4	27.9	48.0	42.9	23.7	43.2
Al_2O_3	n.d.	n.d.	n.d.	n.d.	n.d.	n.d.	n.d.	n.d.	n.d.	n.d.	n.d.	n.d.	n.d.	n.d.	n.d.
SiO_2	40.9	40.8	39.7	40.7	40.6	39.3	40.6	39.9	36.5	35.4	36.0	40.9	39.4	35.1	39.4
CaO	n.d.	n.d.	n.d.	n.d.	0.3	n.d.	0.2	n.d.	n.d.	n.d.	n.d.	0.2	n.d.	n.d.	n.d.
Cr_2O_3	n.d.	n.d.	n.d.	n.d.	n.d.	n.d.	n.d.	n.d.	n.d.	n.d.	n.d.	n.d.	n.d.	0.4	n.d.
MnO	n.d.	n.d.	n.d.	n.d.	n.d.	n.d.	n.d.	n.d.	n.d.	n.d.	n.d.	n.d.	n.d.	0.4	n.d.
FeO	13.1	12.9	17.8	12.0	12.0	20.4	12.6	19.1	34.6	38.5	35.8	11.2	17.5	39.9	16.7
NiO	n.d.	n.d.	n.d.	n.d.	n.d.	n.d.	n.d.	n.d.	n.d.	n.d.	n.d.	n.d.	n.d.	0.5	n.d.
Total	100.8	100.4	100.8	99.6	100.4	100.5	100.5	100.9	99.6	99.2	99.7	100.3	99.8	99.8	99.3
Cations															
Mg	1.71	1.72	1.62	1.73	1.75	1.55	1.73	1.58	1.18	1.07	1.16	1.76	1.62	1.01	1.64
Al	n.d.	n.d.	n.d.	n.d.	n.d.	n.d.	n.d.	n.d.	n.d.	n.d.	n.d.	n.d.	n.d.	n.d.	n.d.
Si	1.01	1.01	1.00	1.01	1.00	1.00	1.00	1.01	1.01	1.01	1.00	1.00	1.00	1.00	1.00
Ca	n.d.	n.d.	n.d.	n.d.	0.01	n.d.	0.01	n.d.	n.d.	n.d.	n.d.	0.01	n.d.	n.d.	n.d.
Cr	n.d.	n.d.	n.d.	n.d.	n.d.	n.d.	n.d.	n.d.	n.d.	n.d.	n.d.	n.d.	n.d.	0.01	n.d.
Mn	n.d.	n.d.	n.d.	n.d.	n.d.	n.d.	n.d.	n.d.	n.d.	n.d.	n.d.	n.d.	n.d.	0.01	n.d.
Fe	0.27	0.27	0.37	0.25	0.25	0.44	0.26	0.40	0.80	0.91	0.83	0.23	0.37	0.95	0.36
Ni	n.d.	n.d.	n.d.	n.d.	n.d.	n.d.	n.d.	n.d.	n.d.	n.d.	n.d.	n.d.	n.d.	0.01	n.d.
Total	2.99	3.00	2.99	2.99	3.01	2.99	3.00	2.99	2.99	2.99	2.99	3.00	2.99	2.99	3.00
Oxygen	4	4	4	4	4	4	4	4	4	4	4	4	4	4	4
Fa, mol%	13.6	13.6	18.6	12.6	12.5	22.1	13.1	20.2	40.4	46.0	41.7	11.6	18.6	48.5	18.0

n.d: not detected.

Table 4. (continued)

	#16	#17	#18	#19	#20	#21	#22	#23	#24	#25	#26	#27	#28	#29
Wt.%														
MgO	24.1	26.3	25.0	25.2	45.6	26.2	43.8	24.8	45.0	41.8	48.5	26.7	43.3	25.7
Al_2O_3	n.d.	n.d.	n.d.	n.d.	n.d.	0.3	n.d.	n.d.	n.d.	n.d.	n.d.	n.d.	n.d.	n.d.
SiO_2	34.6	35.5	35.1	35.5	40.4	35.5	39.9	34.3	40.2	39.8	40.9	35.4	39.4	34.8
CaO	0.3	n.d.	n.d.	n.d.	n.d.	n.d.	n.d.	n.d.	0.2	n.d.	n.d.	n.d.	n.d.	n.d.
Cr_2O_3	0.4	n.d.	n.d.	n.d.	n.d.	0.6	n.d.	0.5	n.d.	n.d.	n.d.	n.d.	n.d.	n.d.
MnO	n.d.	n.d.	n.d.	n.d.	n.d.	n.d.	n.d.	0.5	n.d.	n.d.	n.d.	n.d.	n.d.	n.d.
FeO	39.6	37.3	38.4	39.3	14.6	37.2	16.0	38.1	15.0	18.5	10.1	37.0	17.7	37.1
NiO	n.d.	n.d.	n.d.	n.d.	n.d.	n.d.	n.d.	n.d.	n.d.	n.d.	n.d.	n.d.	n.d.	n.d.
Total	99.0	99.1	98.6	100.0	100.6	99.7	99.6	98.2	100.4	100.1	99.5	99.0	100.4	97.5
Cations														
Mg	1.04	1.11	1.07	1.06	1.69	1.10	1.65	1.07	1.67	1.58	1.78	1.12	1.63	1.10
Al	n.d.	n.d.	n.d.	n.d.	n.d.	0.01	n.d.	n.d.	n.d.	n.d.	n.d.	n.d.	n.d.	n.d.
Si	1.00	1.00	1.01	1.00	1.00	1.00	1.01	0.99	1.00	1.01	1.01	1.00	1.00	1.00
Ca	0.01	n.d.	n.d.	n.d.	n.d.	n.d.	n.d.	n.d.	0.01	n.d.	n.d.	n.d.	n.d.	n.d.
Cr	0.01	n.d.	n.d.	n.d.	n.d.	0.01	n.d.	0.01	n.d.	n.d.	n.d.	n.d.	n.d.	n.d.
Mn	n.d.	n.d.	n.d.	n.d.	n.d.	n.d.	n.d.	0.01	n.d.	n.d.	n.d.	n.d.	n.d.	n.d.
Fe	0.95	0.88	0.92	0.93	0.30	0.87	0.34	0.92	0.31	0.39	0.21	0.87	0.37	0.89
Ni	n.d.	n.d.	n.d.	n.d.	n.d.	n.d.	n.d.	n.d.	n.d.	n.d.	n.d.	n.d.	n.d.	n.d.
Total	3.01	2.99	3.00	2.99	2.99	2.99	3.00	3.00	2.99	2.98	3.00	2.99	3.00	2.99
Oxygen	4	4	4	4	4	4	4	4	4	4	4	4	4	4
Fa, mol%	47.7	44.2	46.2	46.7	15.1	44.2	17.1	46.2	15.7	19.8	10.6	43.7	18.5	44.7

n.d: not detected.

Table 5. Chemical composition of feldspathic glass in the igneous rim. Measurement positions are shown in Figure A5.

	#1	#2	#3	#4	#5	#6	#7	#8	#9	#10	#11	#12	#13
Wt.%													
Na_2O	2.8	2.9	3.2	3.5	3.4	2.6	2.8	3.0	2.6	2.6	2.8	2.5	3.0
MgO	0.9	1.0	1.5	1.3	2.7	1.4	0.8	1.1	0.6	0.7	0.7	0.9	0.9
Al_2O_3	29.7	29.8	28.7	30.2	29.4	30.1	30.6	30.0	31.7	30.9	30.9	30.5	30.0
SiO_2	48.7	48.4	48.5	50.8	49.1	48.1	48.1	48.8	48.2	48.6	48.4	48.2	49.3
CaO	14.7	14.9	13.9	13.4	13.4	15.1	15.1	14.7	15.5	15.2	15.3	15.4	15.0
FeO	2.6	2.8	2.3	2.1	3.1	2.2	2.3	2.3	1.1	1.7	1.8	2.6	1.8
Total	99.4	99.6	98.0	101.3	101.0	99.4	99.7	99.9	99.7	99.7	99.9	100.2	100.0
Cations													
Na	0.25	0.26	0.30	0.31	0.30	0.23	0.25	0.27	0.23	0.24	0.25	0.22	0.27
Mg	0.06	0.07	0.10	0.09	0.19	0.09	0.05	0.08	0.04	0.05	0.05	0.06	0.06
Al	1.63	1.63	1.59	1.61	1.59	1.65	1.68	1.64	1.72	1.68	1.68	1.66	1.63
Si	2.27	2.25	2.28	2.30	2.25	2.24	2.23	2.26	2.23	2.25	2.24	2.23	2.27
Ca	0.74	0.74	0.70	0.65	0.66	0.75	0.75	0.73	0.77	0.75	0.76	0.76	0.74
Fe	0.10	0.11	0.09	0.08	0.12	0.09	0.09	0.09	0.04	0.07	0.07	0.10	0.07
Total	5.05	5.06	5.06	5.04	5.11	5.05	5.05	5.07	5.03	5.04	5.05	5.03	5.04
Oxygen	8	8	8	8	8	8	8	8	8	8	8	8	8

Table 6. Chemical compositions of nepheline in the igneous rim. Measurement positions are shown in Figure A5.

	#14	#15	#16	#17	#18	#19	#20	#21	#22	#23	#24	#25	#26
Wt.%													
Na_2O	16.5	17.7	17.6	15.9	16.6	17.4	16.6	17.6	17.0	14.6	17.1	17.2	17.8
MgO	1.9	n.d.	0.4	2.0	0.6	0.4	0.4	0.4	0.3	1.7	0.9	n.d.	n.d.
Al_2O_3	32.2	33.5	34.3	31.4	34.1	35.5	32.9	33.5	33.2	30.7	32.2	34.0	35.5
SiO_2	43.4	44.9	44.3	41.2	42.6	43.0	44.0	45.6	43.9	43.7	45.0	41.7	42.7
K_2O	1.7	1.6	1.7	1.8	2.1	2.1	1.5	1.4	1.7	1.6	1.6	2.2	2.1
CaO	1.9	1.9	1.8	1.9	2.8	2.7	2.3	1.5	1.8	3.0	3.2	2.3	2.2
FeO	2.0	0.8	0.9	3.1	0.8	0.7	0.5	1.2	1.0	1.3	0.8	0.6	0.3
	99.5	100.4	100.9	97.2	99.6	101.7	98.3	101.2	99.0	96.5	100.8	97.8	100.6
Cations													
Na	1.53	1.62	1.6	1.52	1.53	1.58	1.55	1.59	1.57	1.38	1.56	1.62	1.63
Mg	0.14	n.d.	0.03	0.15	0.04	0.02	0.03	0.03	0.02	0.12	0.06	n.d.	n.d.
Al	1.81	1.86	1.89	1.83	1.92	1.96	1.86	1.84	1.87	1.77	1.79	1.95	1.98
Si	2.07	2.11	2.08	2.04	2.04	2.01	2.11	2.12	2.1	2.14	2.12	2.03	2.02
K	0.10	0.09	0.1	0.11	0.13	0.13	0.09	0.08	0.10	0.10	0.10	0.13	0.12
Ca	0.10	0.09	0.09	0.10	0.14	0.13	0.12	0.08	0.09	0.16	0.16	0.12	0.11
Fe	0.08	0.03	0.03	0.13	0.03	0.03	0.02	0.05	0.04	0.05	0.03	0.02	0.01
Total	5.83	5.80	5.82	5.88	5.83	5.86	5.78	5.79	5.79	5.72	5.82	5.87	5.87
Oxygen	8	8	8	8	8	8	8	8	8	8	8	8	8

n.d.: not detected.

Table 7. Chemical composition of enstatite, pigeonite and augite in the igneous rim. Measurement positions are shown in Figure A5.

	#27	#28	#29	#30	#31	#32	#33	#34	#35	#36	#37	#38	#39	#40	#41
Wt.%															
MgO	24.1	21.8	22.5	23.6	20.5	21.6	23.1	37.5	37.8	37.8	37.8	33.6	34.1	18.7	37.2
Al_2O_3	4.3	4.4	4.0	4.3	4.1	4.8	4.4	1.6	1.4	1.3	1.2	2.1	2.1	7.1	1.7
SiO_2	53.4	52.9	52.8	52.0	52.5	52.7	53.6	58.7	58.6	59.0	58.8	57.6	56.0	51.1	58.5
CaO	13.6	15.9	14.2	12.9	17.5	15.6	14.3	0.6	0.6	0.4	0.5	4.0	3.0	19.1	0.6
TiO_2	1.4	1.8	1.6	1.0	1.8	1.4	1.1	0.3	0.3	0.2	0.2	0.4	0.4	1.2	0.3
Cr_2O_3	1.8	1.6	1.9	1.7	1.5	1.9	1.7	0.8	0.8	0.7	0.6	1.1	1.1	1.4	0.7
MnO	0.6	0.6	0.6	0.7	0.5	0.5	0.4	n.d.	n.d.	n.d.	n.d.	n.d.	n.d.	n.d.	n.d.
FeO	1.7	1.9	1.6	2.9	1.5	1.4	1.4	1.1	0.9	1.1	1.2	1.5	2.5	1.1	0.9
NiO	n.d.	n.d.	n.d.	n.d.	n.d.	n.d.	n.d.	n.d.	n.d.	n.d.	n.d.	n.d.	n.d.	n.d.	n.d.
Total	100.7	100.8	99.2	99.0	99.7	99.9	100.0	100.8	100.4	100.5	100.4	100.4	99.1	99.7	100.0
Cations															
Mg	1.26	1.15	1.20	1.26	1.09	1.14	1.21	1.87	1.89	1.89	1.89	1.70	1.76	1.00	1.87
Al	0.18	0.18	0.17	0.18	0.17	0.20	0.18	0.06	0.06	0.05	0.05	0.09	0.09	0.30	0.07
Si	1.87	1.87	1.89	1.87	1.88	1.87	1.89	1.97	1.97	1.98	1.98	1.96	1.93	1.83	1.97
Ca	0.51	0.60	0.54	0.49	0.67	0.59	0.54	0.02	0.02	0.02	0.02	0.15	0.11	0.73	0.02
Ti	0.04	0.05	0.04	0.03	0.05	0.04	0.03	0.01	0.01	0.00	0.01	0.01	0.01	0.03	0.01
Cr	0.05	0.04	0.05	0.05	0.04	0.05	0.05	0.02	0.02	0.02	0.02	0.03	0.03	0.04	0.02
Mn	0.02	0.02	0.02	0.02	0.02	0.01	0.01	n.d.	n.d.	n.d.	n.d.	n.d.	n.d.	n.d.	n.d.
Fe	0.05	0.06	0.05	0.09	0.04	0.04	0.04	0.03	0.03	0.03	0.03	0.04	0.07	0.03	0.03
Ni	n.d.	n.d.	n.d.	n.d.	n.d.	n.d.	n.d.	n.d.	n.d.	n.d.	n.d.	n.d.	n.d.	n.d.	n.d.
Total	3.98	3.97	3.96	3.99	3.96	3.94	3.95	3.98	4.00	3.99	4.00	3.98	4.00	3.96	3.99
Oxygen	6	6	6	6	6	6	6	6	6	6	6	6	6	6	6
En	69.2	63.5	67.0	68.5	60.6	64.4	67.6	97.4	97.4	97.4	97.4	89.9	90.7	56.8	97.4
Fs	2.7	3.3	2.8	4.9	2.2	2.3	2.2	1.6	1.5	1.5	1.5	2.1	3.6	1.7	1.6
Wo	28.0	33.1	30.2	26.6	37.2	33.3	30.2	1.0	1.0	1.0	1.0	7.9	5.7	41.5	1.0

n.d.: not detected.

Table 7. (continued)

	#42	#43	#44	#45	#46	#47	#48	#49	#50	#51	#52	#53	#54	#55	#56
Wt.%															
MgO	33.9	33.5	19.8	19.6	37.2	37.5	38.0	37.9	22.4	19.1	38.0	37.8	35.4	35.5	34.6
Al_2O_3	1.9	2.5	6.3	6.7	1.6	1.5	1.4	1.2	5.7	6.9	0.9	1.2	2.9	2.9	3.3
SiO_2	57.3	56.9	51.4	51.2	58.6	59.0	59.2	59.2	52.5	50.9	59.4	59.3	57.7	57.8	57.2
CaO	2.8	4.0	18.6	18.3	0.6	0.6	0.7	0.6	16.1	18.8	0.6	1.0	2.2	2.6	2.9
TiO_2	0.3	0.4	1.1	1.2	0.3	0.3	0.3	0.3	0.9	1.3	0.3	0.2	0.3	0.4	0.4
Cr_2O_3	1.0	1.2	0.9	1.2	0.7	0.7	0.7	0.5	1.2	1.3	0.5	0.7	0.9	0.9	1.0
MnO	0.4	n.d.	n.d.	n.d.	n.d.	n.d.	n.d.	n.d.	n.d.	0.4	n.d.	n.d.	n.d.	n.d.	n.d.
FeO	1.1	1.1	1.1	1.2	1.2	1.2	1.3	1.3	1.1	0.9	1.6	1.7	1.3	1.3	1.2
NiO	n.d.	n.d.	n.d.	n.d.	n.d.	n.d.	n.d.	n.d.	n.d.	n.d.	n.d.	n.d.	n.d.	n.d.	n.d.
Total	98.7	99.5	99.4	99.3	100.2	100.8	101.5	100.9	100.1	99.5	101.3	101.8	100.7	101.4	100.6
Cations															
Mg	1.74	1.71	1.06	1.05	1.87	1.87	1.88	1.88	1.18	1.02	1.89	1.87	1.78	1.77	1.74
Al	0.08	0.10	0.27	0.28	0.06	0.06	0.06	0.05	0.24	0.29	0.04	0.05	0.12	0.12	0.13
Si	1.97	1.95	1.85	1.84	1.97	1.97	1.97	1.98	1.86	1.83	1.98	1.97	1.94	1.93	1.93
Ca	0.10	0.15	0.72	0.70	0.02	0.02	0.02	0.02	0.61	0.72	0.02	0.04	0.08	0.09	0.10
Ti	0.01	0.01	0.03	0.03	0.01	0.01	0.01	0.01	0.02	0.03	0.01	0.00	0.01	0.01	0.01
Cr	0.03	0.03	0.03	0.03	0.02	0.02	0.02	0.01	0.03	0.04	0.01	0.02	0.02	0.02	0.03
Mn	0.01	n.d.	n.d.	n.d.	n.d.	n.d.	n.d.	n.d.	n.d.	0.01	n.d.	n.d.	n.d.	n.d.	n.d.
Fe	0.03	0.03	0.03	0.04	0.03	0.03	0.04	0.04	0.03	0.03	0.04	0.05	0.04	0.04	0.03
Ni	n.d.	n.d.	n.d.	n.d.	n.d.	n.d.	n.d.	n.d.	n.d.	n.d.	n.d.	n.d.	n.d.	n.d.	n.d.
Total	3.97	3.98	3.99	3.97	3.98	3.98	4.00	3.99	3.97	3.97	3.99	4.00	3.99	3.98	3.97
Oxygen	6	6	6	6	6	6	6	6	6	6	6	6	6	6	6
En	93.0	90.5	58.6	58.7	97.4	97.4	96.9	96.9	64.8	57.6	96.9	95.4	93.7	93.2	93.0
Fs	1.6	1.6	1.7	2.2	1.6	1.6	2.1	2.1	1.6	1.7	2.1	2.6	2.1	2.1	1.6
Wo	5.3	7.9	39.8	39.1	1.0	1.0	1.0	1.0	33.5	40.7	1.0	2.0	4.2	4.7	5.3

n.d.: not detected.

Table 7. (continued)

	#57	#58	#59	#60	#61	#62	#63	#64	#65	#66	#67	#68	#69	#70	#71
Wt.%															
MgO	34.5	20.2	21.2	35.9	33.4	19.5	19.0	20.6	20.3	36.7	37.3	37.9	38.0	34.4	33.5
Al_2O_3	3.5	6.6	6.8	1.8	2.7	7.1	7.5	6.1	5.8	1.5	1.3	1.2	1.4	2.8	2.5
SiO_2	57.2	51.7	51.9	58.3	57.7	51.6	51.6	52.3	52.0	58.1	58.2	59.0	59.3	57.2	57.3
CaO	3.2	17.7	16.8	2.4	5.1	18.9	19.4	17.8	18.3	0.6	0.7	0.6	0.5	2.3	4.4
TiO_2	0.4	0.9	1.2	0.4	0.5	1.2	1.4	1.1	1.1	0.3	0.4	0.2	0.4	0.3	0.4
Cr_2O_3	1.2	1.5	1.3	1.1	1.3	1.5	1.4	1.4	1.3	0.8	0.8	0.8	0.7	1.2	1.2
MnO	n.d.	n.d.	n.d.	n.d.	n.d.	n.d.	n.d.	0.4	0.3	n.d.	n.d.	n.d.	n.d.	n.d.	n.d.
FeO	1.4	1.2	1.1	1.3	1.2	1.3	1.3	1.2	1.4	1.4	1.1	0.9	0.9	1.3	1.1
NiO	n.d.	n.d.	n.d.	n.d.	n.d.	n.d.	n.d.	n.d.	n.d.	n.d.	n.d.	n.d.	n.d.	0.6	n.d.
Total	101.3	99.8	100.2	101.1	101.8	101.1	101.6	100.7	100.5	99.4	99.7	100.6	101.1	100.1	100.3
Cations															
Mg	1.73	1.08	1.12	1.79	1.67	1.03	1.00	1.09	1.08	1.86	1.88	1.89	1.88	1.74	1.70
Al	0.14	0.28	0.28	0.07	0.11	0.30	0.31	0.26	0.24	0.06	0.05	0.05	0.05	0.11	0.10
Si	1.92	1.84	1.84	1.96	1.94	1.82	1.82	1.85	1.85	1.97	1.97	1.97	1.97	1.94	1.95
Ca	0.12	0.68	0.64	0.09	0.18	0.72	0.73	0.67	0.70	0.02	0.02	0.02	0.02	0.08	0.16
Ti	0.01	0.02	0.03	0.01	0.01	0.03	0.04	0.03	0.03	0.01	0.01	0.00	0.01	0.01	0.01
Cr	0.03	0.04	0.04	0.03	0.03	0.04	0.04	0.04	0.04	0.02	0.02	0.02	0.02	0.03	0.03
Mn	n.d.	n.d.	n.d.	n.d.	n.d.	n.d.	n.d.	0.01	0.01	n.d.	n.d.	n.d.	n.d.	n.d.	n.d.
Fe	0.04	0.04	0.03	0.04	0.03	0.04	0.04	0.03	0.04	0.04	0.03	0.02	0.02	0.04	0.03
Ni	n.d.	n.d.	n.d.	n.d.	n.d.	n.d.	n.d.	n.d.	n.d.	n.d.	n.d.	n.d.	n.d.	0.02	n.d.
Total	3.99	3.98	3.98	3.99	3.97	3.98	3.98	3.98	3.99	3.98	3.98	3.97	3.97	3.97	3.98
Oxygen	6	6	6	6	6	6	6	6	6	6	6	6	6	6	6
En	91.5	60.0	62.6	93.2	88.8	57.5	56.5	60.9	59.3	96.9	97.4	97.9	97.9	93.5	89.9
Fs	2.1	2.2	1.7	2.1	1.6	2.2	2.3	1.7	2.2	2.1	1.6	1.0	1.0	2.2	1.6
Wo	6.3	37.8	35.8	4.7	9.6	40.2	41.2	37.4	38.5	1.0	1.0	1.0	1.0	4.3	8.5

n.d.: not detected.

Table 7. (continued)

	#72	#73	#74	#75	#76	#77	#78	#79	#80	#81	#82	#83	#84	#85	#86
Wt.%															
MgO	21.1	37.0	37.6	37.5	34.5	37.2	35.1	37.5	38.2	38.2	38.1	37.0	37.9	38.2	38.2
Al_2O_3	5.3	1.5	1.3	1.4	1.8	1.4	3.6	1.3	1.0	1.2	1.0	0.9	0.9	0.9	0.9
SiO_2	52.5	58.6	58.5	58.2	57.4	58.9	57.0	58.8	59.4	59.1	58.9	58.1	59.4	59.2	59.4
CaO	17.8	0.6	0.5	0.5	3.0	1.1	2.1	0.6	0.5	0.4	0.5	0.6	0.4	0.5	0.4
TiO_2	1.1	0.4	0.4	0.4	0.3	0.3	0.4	0.2	0.3	0.2	0.3	0.3	0.2	0.2	0.1
Cr_2O_3	1.4	0.8	0.6	0.6	0.9	0.6	1.0	0.7	0.5	0.7	0.5	0.6	0.7	0.7	0.4
MnO	n.d.	n.d.	n.d.	n.d.	n.d.	n.d.	n.d.	n.d.	n.d.	n.d.	n.d.	n.d.	n.d.	n.d.	n.d.
FeO	1.2	1.0	0.9	1.0	1.9	0.8	0.9	0.9	1.3	1.4	1.1	3.0	1.3	1.3	1.1
NiO	n.d.	n.d.	n.d.	n.d.	n.d.	n.d.	n.d.	n.d.	n.d.	n.d.	n.d.	n.d.	n.d.	n.d.	n.d.
Total	100.3	100.0	99.6	99.5	99.9	100.2	100.0	100.0	101.2	101.2	100.4	100.5	100.9	100.8	100.6
Cations															
Mg	1.12	1.86	1.89	1.89	1.75	1.86	1.77	1.88	1.90	1.90	1.90	1.86	1.89	1.90	1.91
Al	0.22	0.06	0.05	0.06	0.07	0.05	0.14	0.05	0.04	0.05	0.04	0.04	0.04	0.03	0.04
Si	1.86	1.97	1.97	1.97	1.96	1.98	1.93	1.98	1.98	1.97	1.98	1.97	1.98	1.98	1.99
Ca	0.68	0.02	0.02	0.02	0.11	0.04	0.08	0.02	0.02	0.01	0.02	0.02	0.02	0.02	0.01
Ti	0.03	0.01	0.01	0.01	0.01	0.01	0.01	0.00	0.01	0.00	0.01	0.01	0.01	0.00	0.00
Cr	0.04	0.02	0.02	0.02	0.02	0.02	0.03	0.02	0.01	0.02	0.01	0.02	0.02	0.02	0.01
Mn	n.d.	n.d.	n.d.	n.d.	n.d.	n.d.	n.d.	n.d.	n.d.	n.d.	n.d.	n.d.	n.d.	n.d.	n.d.
Fe	0.04	0.03	0.02	0.03	0.06	0.02	0.03	0.02	0.04	0.04	0.03	0.08	0.04	0.04	0.03
Ni	n.d.	n.d.	n.d.	n.d.	n.d.	n.d.	n.d.	n.d.	n.d.	n.d.	n.d.	n.d.	n.d.	n.d.	n.d.
Total	3.99	3.97	3.98	4.00	3.98	3.98	3.99	3.97	4.00	3.99	3.99	4.00	4.00	3.99	3.99
Oxygen	6	6	6	6	6	6	6	6	6	6	6	6	6	6	6
En	60.9	97.4	97.9	97.4	91.1	96.9	94.1	97.9	96.9	97.4	97.4	94.9	96.9	96.9	97.9
Fs	2.2	1.6	1.0	1.5	3.1	1.0	1.6	1.0	2.0	2.1	1.5	4.1	2.1	2.0	1.5
Wo	37.0	1.0	1.0	1.0	5.7	2.1	4.3	1.0	1.0	0.5	1.0	1.0	1.0	1.0	0.5

n.d.: not detected.

Table 7. (continued)

	#87	#88	#89	#90	#91	#92	#93	#94	#95	#96	#97	#98	#99	#100	#101
Wt.%															
MgO	37.3	37.9	33.6	34.4	20.7	21.7	37.2	37.6	37.4	37.3	37.4	37.9	19.9	18.7	37.3
Al_2O_3	1.3	1.1	2.5	2.1	3.5	3.8	1.3	1.0	1.0	1.1	0.9	0.9	6.9	7.1	1.3
SiO_2	58.5	59.0	57.5	57.8	53.2	53.1	58.6	58.6	58.4	58.4	58.4	59.1	50.9	50.3	58.6
CaO	0.5	0.5	4.4	3.7	18.5	16.5	0.5	0.5	0.4	0.6	0.3	0.4	17.4	18.1	0.6
TiO_2	0.3	0.3	0.6	0.4	1.5	1.3	0.2	0.3	0.2	0.3	0.1	0.1	0.9	1.2	0.2
Cr_2O_3	0.8	0.8	1.2	1.1	1.1	1.2	0.9	0.7	0.5	0.6	0.4	0.4	1.4	1.3	0.7
MnO	n.d.	n.d.	0.4	n.d.	0.3	0.5	n.d.	n.d.	n.d.	n.d.	n.d.	n.d.	0.7	0.5	n.d.
FeO	1.7	1.2	1.2	1.2	0.9	1.6	1.3	1.2	1.3	1.2	1.2	1.1	1.4	1.4	1.1
NiO	n.d.	n.d.	n.d.	n.d.	n.d.	n.d.	n.d.	n.d.	n.d.	n.d.	n.d.	n.d.	n.d.	n.d.	n.d.
Total	100.2	100.8	101.4	100.6	99.6	99.7	100.0	99.8	99.2	99.4	98.7	99.9	99.3	98.6	99.7
Cations															
Mg	1.87	1.89	1.69	1.74	1.10	1.15	1.87	1.89	1.89	1.88	1.90	1.90	1.07	1.01	1.88
Al	0.05	0.04	0.10	0.08	0.15	0.16	0.05	0.04	0.04	0.04	0.03	0.04	0.29	0.30	0.05
Si	1.97	1.97	1.94	1.96	1.90	1.90	1.97	1.98	1.98	1.98	1.99	1.99	1.83	1.82	1.98
Ca	0.02	0.02	0.16	0.13	0.71	0.63	0.02	0.02	0.01	0.02	0.01	0.01	0.67	0.70	0.02
Ti	0.01	0.01	0.01	0.01	0.04	0.03	0.00	0.01	0.00	0.01	0.00	0.00	0.02	0.03	0.00
Cr	0.02	0.02	0.03	0.03	0.03	0.03	0.02	0.02	0.01	0.02	0.01	0.01	0.04	0.04	0.02
Mn	n.d.	n.d.	0.01	n.d.	0.01	0.02	n.d.	n.d.	n.d.	n.d.	n.d.	n.d.	0.02	0.01	n.d.
Fe	0.05	0.03	0.03	0.03	0.03	0.05	0.04	0.03	0.04	0.03	0.04	0.03	0.04	0.04	0.03
Ni	n.d.	n.d.	n.d.	n.d.	n.d.	n.d.	n.d.	n.d.	n.d.	n.d.	n.d.	n.d.	n.d.	n.d.	n.d.
Total	3.99	3.98	3.97	3.98	3.97	3.97	3.97	3.99	3.97	3.98	3.98	3.98	3.98	3.95	3.98
Oxygen	6	6	6	6	6	6	6	6	6	6	6	6	6	6	6
En	96.4	97.4	89.9	91.6	59.8	62.8	96.9	97.4	97.4	97.4	97.4	97.9	60.1	57.7	97.4
Fs	2.6	1.5	1.6	1.6	1.6	2.7	2.1	1.5	2.1	1.6	2.1	1.5	2.2	2.3	1.6
Wo	1.0	1.0	8.5	6.8	38.6	34.4	1.0	1.0	0.5	1.0	0.5	0.5	37.6	40.0	1.0

n.d.: not detected.

Table 7. (continued)

	#102	#103	#104	#105	#106	#107	#108	#109	#110	#111	#112	#113
Wt.%												
MgO	37.2	37.1	36.9	36.7	37.7	37.8	37.3	19.6	21.0	18.7	19.1	18.9
Al_2O_3	1.3	1.4	1.5	1.5	1.5	1.4	1.2	6.3	4.5	6.0	6.3	6.7
SiO_2	58.3	57.8	58.6	58.2	58.6	58.9	58.7	52.5	53.0	51.9	51.6	51.4
CaO	0.5	0.5	0.6	0.7	0.7	0.5	0.6	19.8	17.8	19.5	19.5	19.3
TiO_2	0.3	0.1	0.2	0.3	0.4	0.5	0.3	1.1	0.9	1.2	1.2	1.2
Cr_2O_3	0.8	0.7	0.7	0.6	0.7	0.8	0.4	1.2	1.1	1.2	1.0	1.2
MnO	n.d.	n.d.	n.d.	n.d.	n.d.	n.d.	n.d.	n.d.	0.4	n.d.	n.d.	n.d.
FeO	1.2	1.3	0.8	0.7	1.0	0.8	1.0	0.7	0.8	1.3	0.7	0.7
NiO	n.d.	n.d.	n.d.	n.d.	n.d.	n.d.	n.d.	n.d.	n.d.	n.d.	n.d.	n.d.
Total	99.5	99.0	99.2	98.7	100.5	100.7	99.5	101.1	99.5	99.8	99.4	99.5
Cations												
Mg	1.88	1.89	1.86	1.86	1.88	1.88	1.88	1.03	1.12	1.00	1.02	1.01
Al	0.05	0.06	0.06	0.06	0.06	0.06	0.05	0.26	0.19	0.26	0.27	0.28
Si	1.97	1.97	1.98	1.98	1.96	1.97	1.98	1.85	1.89	1.86	1.85	1.84
Ca	0.02	0.02	0.02	0.03	0.02	0.02	0.02	0.75	0.68	0.75	0.75	0.74
Ti	0.01	0.00	0.01	0.01	0.01	0.01	0.01	0.03	0.02	0.03	0.03	0.03
Cr	0.02	0.02	0.02	0.02	0.02	0.02	0.01	0.03	0.03	0.03	0.03	0.03
Mn	n.d.	n.d.	n.d.	n.d.	n.d.	n.d.	n.d.	n.d.	0.01	n.d.	n.d.	n.d.
Fe	0.03	0.04	0.02	0.02	0.03	0.02	0.03	0.02	0.02	0.04	0.02	0.02
Ni	n.d.	n.d.	n.d.	n.d.	n.d.	n.d.	n.d.	n.d.	n.d.	n.d.	n.d.	n.d.
Total	3.98	4.00	3.97	3.98	3.98	3.98	3.98	3.97	3.96	3.97	3.97	3.95
Oxygen	6	6	6	6	6	6	6	6	6	6	6	6
En	97.4	96.9	97.9	97.4	97.4	97.9	97.4	57.2	61.5	55.9	57.0	57.1
Fs	1.6	2.1	1.1	1.0	1.6	1.0	1.6	1.1	1.1	2.2	1.1	1.1
Wo	1.0	1.0	1.1	1.6	1.0	1.0	1.0	41.7	37.4	41.9	41.9	41.8

n.d.: not detected.

Table 8. Chemical compositions of Fe-(Ni) sulfides in the igneous rim. Measurement positions are shown in Figure A6.

	#1	#2	#3	#4	#5	#6	#7	#8	#9	#10	#11	#12	#13	#14	#15	#16	#17	#18
S	33.1	31.0	30.9	33.9	33.6	31.1	31.1	33.3	33.9	33.7	33.8	33.5	31.7	33.8	33.4	31.1	31.5	31.0
Fe	63.0	46.4	45.6	63.4	63.1	46.5	45.8	63.3	63.3	62.8	63.2	63.1	47.6	63.6	64.0	46.6	44.5	45.0
Ni	n.d.	18.5	18.6	n.d.	n.d.	17.5	18.6	n.d.	n.d.	n.d.	n.d.	n.d.	15.6	n.d.	n.d.	16.6	19.6	18.8
Total	96.1	95.9	95.1	97.3	96.7	95.1	95.5	96.6	97.2	96.5	96.9	96.6	95.0	97.3	97.3	94.2	95.6	94.8

n.d.: not detected.

Table 9. Chemical composition of olivine in matrix.

	#1	#2	#3	#4	#5	#6	#7	#8	#9	#10	#11	#12	#13	#14	#15
Wt.%															
MgO	24.5	23.7	23.5	23.9	25.5	23.8	24.5	25.4	25.4	23.0	23.4	22.8	24.1	24.5	24.1
SiO_2	35.3	34.3	34.7	34.7	35.7	35.4	34.9	35.6	35.4	35.0	34.7	34.6	35.5	35.4	35.5
CaO	n.d.	n.d.	0.3	n.d.	n.d.	n.d.	n.d.	n.d.	n.d.	n.d.	n.d.	n.d.	n.d.	n.d.	n.d.
FeO	40.7	40.2	41.3	41.3	39.5	42.0	40.2	39.4	38.8	41.9	40.8	42.0	40.6	41.6	40.9
Total	100.5	98.2	99.8	99.9	100.6	101.2	99.6	100.4	99.5	99.9	98.8	99.3	100.2	101.4	100.5
Cations															
Mg	1.03	1.03	1.01	1.02	1.07	1.00	1.04	1.07	1.07	0.98	1.01	0.98	1.02	1.03	1.02
Si	1.00	1.00	1.00	0.99	1.00	1.00	1.00	1.00	1.00	1.00	1.00	1.00	1.01	1.00	1.01
Ca	n.d.	n.d.	0.01	n.d.	n.d.	n.d.	n.d.	n.d.	n.d.	n.d.	n.d.	n.d.	n.d.	n.d.	n.d.
Fe	0.96	0.98	0.99	0.99	0.93	0.99	0.96	0.93	0.92	1.01	0.99	1.02	0.96	0.98	0.97
Total	2.99	3.01	3.01	3.00	3.00	2.99	3.00	3.00	2.99	2.99	3.00	3.00	2.99	3.01	3.00
Oxygen	4	4	4	4	4	4	4	4	4	4	4	4	4	4	4
Fa, mol%	48.2	48.8	49.5	49.3	46.5	49.7	48.0	46.5	46.2	50.8	49.5	51.0	48.5	48.8	48.7

n.d.: not detected.

Table 10. Oxygen isotopic composition of olivine in the chondrule.

	$\delta^{17}O$	2σ	$\delta^{18}O$	2σ	$\Delta^{17}O$	2σ
Chondrule						
	-8.7	2.2	-3.5	1.2	-6.8	2.3
	-8.1	1.9	-4.5	1.5	-5.8	1.9
	-7.1	1.8	-4.7	1.4	-4.7	1.9
	-6.3	1.5	-2.4	1.6	-5.1	1.4

Table 11. Oxygen isotopic composition of olivine in the igneous rim. Measurement positions are shown in Figure A7.

	Anal#	$\delta^{17}O$	2σ	$\delta^{18}O$	2σ	$\Delta^{17}O$	2σ
FeO-rich olivine							
	1	1.1	1.7	6.1	1.8	-2.1	1.7
	32	2.9	1.7	9.2	2.3	-1.9	1.6
	40	2.2	1.7	9.2	2.1	-2.6	1.8
MgO-rich olivine							
	2	-5.9	1.7	-1.8	1.1	-5.0	1.6
	3	-6.4	1.7	-1.8	1.5	-5.5	1.4
	4	-8.2	1.4	-3.9	1.7	-6.2	1.7
	5	-5.3	1.1	0.5	0.9	-5.5	1.0
	6	-6.2	1.6	-1.8	1.2	-5.3	1.7
	7	-7.4	1.6	-2.4	1.3	-6.1	1.5
	8	-6.6	1.5	-1.7	1.2	-5.7	1.6
	9	-8.5	2.3	-4.7	1.8	-6.1	2.0
	10	-3.6	1.6	-0.2	1.8	-3.5	1.6
	11	-7.0	2.1	-3.0	1.4	-5.4	2.2
	12	-6.7	1.7	-1.7	1.2	-5.8	2.0
	13	-5.9	1.7	-2.1	1.6	-4.8	2.0
	14	-4.9	1.4	-1.1	1.1	-4.4	1.7
	16	-2.7	1.8	1.6	1.5	-3.5	1.8
	17	-3.5	2.1	1.5	1.6	-4.2	2.1
	18	-4.7	1.5	0.4	1.1	-5.0	1.4
	19	-3.5	1.3	1.4	1.3	-4.2	1.5
	20	-6.1	1.5	0.0	1.3	-6.1	1.4
	21	-3.1	1.9	0.6	1.7	-3.4	2.1
	22	-4.9	1.9	0.5	1.4	-5.2	1.9
	23	-6.6	1.8	-1.9	2.1	-5.6	1.3
	24	-6.2	1.8	0.5	1.4	-6.5	1.9
	25	-5.6	2.1	0.4	1.4	-5.8	2.0
	26	-5.6	1.4	-0.3	1.3	-5.4	1.6
	27	-3.9	1.3	0.2	1.4	-4.0	1.5
	28	-4.2	1.4	-0.4	1.2	-4.0	1.7
	29	-3.6	1.5	0.9	1.5	-4.1	1.4
	30	-5.2	1.5	2.0	1.3	-6.3	1.5
	31	-3.0	1.7	2.5	1.1	-4.3	1.6
	33	-6.2	1.9	0.3	2.0	-6.3	2.1
	34	-5.8	1.5	0.6	1.6	-6.1	1.6
	35	-4.5	2.0	0.6	1.1	-4.7	1.8
	36	-7.6	1.4	-2.6	1.3	-6.3	1.7
	37	-8.3	2.2	-2.9	1.5	-6.8	2.2
	38	-6.2	1.9	-3.5	1.2	-4.4	1.9
	39	-7.5	1.5	-2.0	1.6	-6.5	1.8
^{16}O-MgO-rich olivine							
	15	-18.2	1.8	-14.5	1.6	-10.6	1.8

Table 12. Oxygen isotopic composition of olivine in the igneous rim from SCAPS.

	FeO-rich ol		MgO-rich ol		^{16}O-MgO-rich ol	
	$\delta^{18}O$	2σ	$\delta^{18}O$	2σ	$\delta^{18}O$	2σ
(a)	10.4	3.0	-1.9	2.9	-30.6	3.7
(b)	11.1	3.3	-2.3	3.4	-16.1	3.3
(c)	6.5	2.6	-2.5	2.9	-33.1	3.2
(d)	5.9	3.2	-1.4	3.1	-30.2	3.4
					-28.3	4.9
					-15.4	5.1
					-24.0	5.0
(e)	6.2	4.0	-4.3	2.7	-19.8	3.4
			-1.7	2.7	-16.9	3.0
(f)	12.0	2.0	-0.7	3.6	-31.5	4.7

Table 13. Chemical composition of olivine along line profiles. Measurement positions are indicated in Figure A4.

(a)	Distance (µm)	MgO	Al_2O_3	SiO_2	SO_3	CaO	TiO_2	Cr_2O_3	MnO	FeO	Total
#1	-0.9	27.3	n.d	35.2	1.3	n.d	n.d	n.d	n.d	37.5	101.2
#2	-0.6	27.4	0.4	35.6	n.d	n.d	0.4	n.d	0.5	37.1	101.4
#3	-0.3	27.9	n.d	35.7	n.d	n.d	n.d	0.4	n.d	37.3	101.3
#4	0	28.8	n.d	35.9	n.d	n.d	n.d	0.5	n.d	36.7	101.9
#5	0.3	31.5	n.d	36.5	n.d	n.d	n.d	0.5	n.d	33.7	102.2
#6	0.6	34.2	n.d	37.8	n.d	n.d	n.d	n.d	n.d	29.0	100.9
#7	0.9	36.9	n.d	38.8	n.d	n.d	n.d	n.d	n.d	26.1	101.8
#8	1.2	39.1	n.d	38.7	n.d	n.d	n.d	n.d	n.d	23.3	101.1
#9	1.5	40.9	n.d	39.9	n.d	n.d	n.d	n.d	n.d	21.2	102.0
#10	1.8	42.7	n.d	39.9	n.d	n.d	n.d	n.d	n.d	18.5	101.0
#11	2.1	43.8	n.d	40.1	n.d	n.d	n.d	n.d	n.d	17.6	101.5
#12	2.4	44.3	n.d	40.3	n.d	n.d	n.d	n.d	n.d	16.2	100.9
#13	2.7	45.3	n.d	40.7	n.d	n.d	n.d	n.d	n.d	15.0	100.9
#14	3.0	45.8	n.d	40.8	n.d	n.d	n.d	n.d	n.d	14.3	100.9
#15	3.3	46.4	n.d	41.1	n.d	n.d	n.d	n.d	n.d	13.7	101.2
#16	3.6	46.9	n.d	40.9	n.d	n.d	n.d	n.d	n.d	13.5	101.3
#17	3.9	46.9	n.d	41.1	n.d	n.d	n.d	n.d	n.d	12.5	100.5
#18	4.2	47.0	n.d	41.0	n.d	0.3	n.d	n.d	n.d	12.7	101.0
#19	4.5	47.2	n.d	41.2	n.d	n.d	n.d	n.d	n.d	12.6	101.0
#20	4.8	47.6	n.d	41.1	n.d	n.d	n.d	n.d	n.d	12.6	101.4
#21	5.1	47.2	n.d	40.9	n.d	n.d	n.d	n.d	n.d	12.2	100.2
#22	5.4	47.7	n.d	41.5	n.d	0.3	n.d	n.d	n.d	12.6	102.0
#23	5.7	47.5	n.d	41.0	n.d	n.d	n.d	n.d	n.d	12.2	100.8
#24	6.0	47.4	n.d	41.2	n.d	n.d	n.d	n.d	n.d	12.0	100.7
#25	6.3	47.2	n.d	41.6	n.d	0.3	n.d	n.d	n.d	12.4	101.4
#26	6.6	48.0	n.d	41.2	n.d	n.d	n.d	n.d	0.4	12.4	101.9

n.d.: not detected.

(b)	Distance (μm)	MgO	Al_2O_3	SiO_2	CaO	Cr_2O_3	FeO	Total
#1	-0.9	23.1	n.d.	34.0	n.d.	1.2	41.1	99.3
#2	-0.6	22.5	0.9	33.2	n.d.	2.0	40.1	98.7
#3	-0.3	23.1	1.0	33.4	n.d.	1.8	40.7	100.0
#4	0	24.1	1.0	33.7	0.3	1.9	40.4	101.5
#5	0.3	26.9	n.d.	35.3	n.d.	0.9	37.5	100.6
#6	0.6	28.8	n.d.	36.3	n.d.	n.d.	35.8	100.9
#7	0.9	30.7	n.d.	36.4	n.d.	n.d.	33.7	100.7
#8	1.2	32.6	n.d.	37.2	n.d.	n.d.	31.9	101.6
#9	1.5	34.9	n.d.	37.9	n.d.	n.d.	29.0	101.7
#10	1.8	37.5	n.d.	38.3	n.d.	n.d.	25.7	101.5
#11	2.1	39.7	n.d.	38.6	n.d.	n.d.	22.7	100.9
#12	2.4	41.5	n.d.	39.6	n.d.	n.d.	20.2	101.3
#13	2.7	42.7	n.d.	39.8	n.d.	n.d.	18.0	100.5
#14	3.0	44.3	n.d.	40.2	n.d.	n.d.	17.2	101.6
#15	3.3	44.4	n.d.	40.3	n.d.	n.d.	16.2	100.9
#16	3.6	45.0	n.d.	40.1	n.d.	n.d.	15.4	100.4
#17	3.9	44.7	n.d.	40.4	n.d.	n.d.	14.7	99.8
#18	4.2	45.2	n.d.	40.5	n.d.	n.d.	14.7	100.4
#19	4.5	45.9	n.d.	40.7	n.d.	n.d.	14.9	101.5
#20	4.8	45.2	n.d.	40.0	n.d.	n.d.	14.4	99.6
#21	5.1	45.0	n.d.	40.7	n.d.	n.d.	14.5	100.3
#22	5.4	45.2	n.d.	40.5	n.d.	n.d.	14.9	100.6
#23	5.7	45.2	n.d.	40.0	n.d.	n.d.	14.5	99.7
#24	6.0	45.6	n.d.	40.4	n.d.	n.d.	14.4	100.4
#25	6.3	45.1	n.d.	40.0	n.d.	n.d.	14.8	99.9
#26	6.6	44.8	n.d.	40.3	n.d.	n.d.	14.8	99.9
#27	6.9	45.0	n.d.	40.2	n.d.	n.d.	14.9	100.1

n.d.: not detected.

(c)	Distance (μm)	MgO	Al_2O_3	SiO_2	CaO	Cr_2O_3	FeO	Total
#1	-1.8	27.0	1.1	35.8	n.d.	0.5	37.1	101.5
#2	-1.5	26.5	1.0	35.4	n.d.	0.6	37.4	100.9
#3	-1.2	26.9	1.5	35.0	n.d.	0.9	37.1	101.4
#4	-0.9	27.3	0.9	35.5	n.d.	0.5	37.0	101.1
#5	-0.6	26.9	0.9	35.3	n.d.	0.7	36.8	100.6
#6	-0.3	27.4	1.0	35.4	n.d.	0.8	37.1	101.6
#7	0	27.6	1.7	34.5	n.d.	1.3	36.5	101.6
#8	0.3	28.8	0.8	35.9	n.d.	1.2	34.9	101.5
#9	0.6	31.9	n.d.	37.2	n.d.	0.5	29.9	99.5
#10	0.9	35.3	n.d.	38.3	n.d.	n.d.	25.3	98.9
#11	1.2	38.5	n.d.	38.7	n.d.	n.d.	22.1	99.3
#12	1.5	40.9	n.d.	39.5	0.3	n.d.	19.4	100.1
#13	1.8	42.4	n.d.	39.8	n.d.	n.d.	17.1	99.3
#14	2.1	43.8	n.d.	40.7	n.d.	n.d.	15.9	100.4
#15	2.4	44.9	n.d.	40.7	n.d.	n.d.	15.0	100.5
#16	2.7	45.8	n.d.	40.6	n.d.	n.d.	14.6	101.0
#17	3.0	46.0	n.d.	40.8	n.d.	n.d.	14.3	101.1
#18	3.3	46.3	n.d.	41.1	n.d.	n.d.	14.1	101.4
#19	3.6	46.2	n.d.	41.1	n.d.	n.d.	14.1	101.3
#20	3.9	46.3	n.d.	40.7	n.d.	n.d.	13.9	100.9
#21	4.2	46.5	n.d.	40.8	n.d.	n.d.	13.8	101.0
#22	4.5	46.5	n.d.	40.8	n.d.	n.d.	13.9	101.2
#23	4.8	46.4	n.d.	40.7	n.d.	n.d.	13.4	100.5
#24	5.1	46.4	n.d.	40.9	n.d.	n.d.	14.2	101.5
#25	5.4	46.4	n.d.	41.0	n.d.	n.d.	14.0	101.4
#26	5.7	46.4	n.d.	40.8	n.d.	n.d.	14.6	101.8

n.d.: not detected.

(d)	Distance (μm)	MgO	Al_2O_3	SiO_2	Cr_2O_3	MnO	FeO	Total
#1	-1.8	25.5	0.6	35.5	0.6	n.d	39.6	101.8
#2	-1.5	25.8	0.7	35.7	n.d	n.d	39.5	101.8
#3	-1.2	25.5	0.7	35.5	0.6	n.d	39.2	101.5
#4	-0.9	25.6	0.5	35.3	0.5	n.d	38.8	100.6
#5	-0.6	26.1	0.6	35.6	0.5	n.d	38.5	101.4
#6	-0.3	26.3	n.d	36.0	n.d	0.5	38.6	101.4
#7	0	26.7	0.5	35.6	0.5	n.d	38.3	101.7
#8	0.3	27.9	0.6	36.0	0.6	n.d	36.5	101.6
#9	0.6	31.2	n.d	37.4	n.d	n.d	32.2	100.7
#10	0.9	33.7	n.d	37.5	n.d	n.d	29.0	100.2
#11	1.2	36.0	n.d	38.1	n.d	n.d	25.3	99.5
#12	1.5	37.9	n.d	39.1	n.d	n.d	22.2	99.2
#13	1.8	40.1	n.d	39.3	n.d	n.d	20.5	99.9
#14	2.1	41.5	n.d	39.7	n.d	n.d	18.7	100.0
#15	2.4	42.7	n.d	40.0	n.d	n.d	17.1	99.8
#16	2.7	44.2	n.d	40.6	n.d	n.d	16.1	100.8
#17	3.0	44.6	n.d	40.3	n.d	n.d	15.0	99.9
#18	3.3	45.6	n.d	41.2	n.d	n.d	14.5	101.3
#19	3.6	46.0	n.d	41.0	n.d	n.d	14.6	101.6
#20	3.9	46.3	n.d	41.0	n.d	n.d	14.4	101.7
#21	4.2	46.4	n.d	41.1	n.d	n.d	13.8	101.3
#22	4.5	46.5	n.d	41.0	n.d	n.d	14.2	101.7
#23	4.8	46.7	n.d	40.6	n.d	n.d	13.4	100.6
#24	5.1	46.6	n.d	40.9	n.d	n.d	13.7	101.2
#25	5.4	47.2	n.d	40.8	n.d	n.d	13.1	101.1
#26	5.7	47.2	n.d	41.2	n.d	n.d	13.3	101.7

n.d.: not detected.

(e)	Distance (μm)	MgO	Al_2O_3	SiO_2	CaO	TiO_2	Cr_2O_3	FeO	Total
#1	-0.9	25.5	2.4	34.4	n.d.	n.d.	n.d.	38.4	100.7
#2	-0.6	22.9	8.6	30.7	n.d.	n.d.	0.8	37.9	100.9
#3	-0.3	24.9	6.2	32.3	n.d.	n.d.	0.5	37.5	101.3
#4	0	25.7	4.5	32.3	n.d.	0.4	0.5	37.7	101.1
#5	0.3	29.5	2.9	34.1	n.d.	0.5	0.8	35.7	103.5
#6	0.6	33.1	1.5	36.2	n.d.	n.d.	0.5	31.8	103.0
#7	0.9	36.3	0.7	38.0	n.d.	n.d.	n.d.	27.8	102.8
#8	1.2	39.4	n.d.	38.6	n.d.	n.d.	n.d.	24.7	102.6
#9	1.5	41.4	n.d.	39.7	n.d.	n.d.	n.d.	21.9	103.0
#10	1.8	43.3	n.d.	40.2	n.d.	n.d.	n.d.	19.4	102.8
#11	2.1	44.0	n.d.	39.9	n.d.	n.d.	n.d.	16.8	100.7
#12	2.4	45.5	n.d.	40.8	n.d.	n.d.	n.d.	15.4	101.7
#13	2.7	45.9	n.d.	40.6	n.d.	n.d.	n.d.	14.5	101.0
#14	3.0	46.3	n.d.	40.8	n.d.	n.d.	n.d.	13.8	100.8
#15	3.3	46.6	n.d.	41.2	n.d.	n.d.	n.d.	13.4	101.1
#16	3.6	47.4	n.d.	40.9	n.d.	n.d.	n.d.	13.3	101.6
#17	3.9	47.4	n.d.	41.0	n.d.	n.d.	n.d.	13.0	101.5
#18	4.2	47.9	n.d.	40.8	n.d.	n.d.	n.d.	13.2	101.9
#19	4.5	47.5	n.d.	41.1	n.d.	n.d.	n.d.	12.5	101.1
#20	4.8	47.8	n.d.	40.8	0.3	n.d.	n.d.	12.7	101.6
#21	5.1	47.4	n.d.	41.1	n.d.	n.d.	n.d.	12.6	101.1
#22	5.4	47.3	n.d.	40.7	n.d.	n.d.	n.d.	12.7	100.7
#23	5.7	47.6	n.d.	41.0	n.d.	n.d.	n.d.	13.0	101.6
#24	6.0	47.0	n.d.	40.9	n.d.	n.d.	n.d.	12.3	100.2
#25	6.3	47.3	n.d.	41.2	n.d.	n.d.	n.d.	13.0	101.5
#26	6.6	47.0	n.d.	41.1	0.3	n.d.	n.d.	13.0	101.4
#27	6.9	47.1	n.d.	40.9	n.d.	n.d.	n.d.	13.1	101.1

n.d.: not detected.

(f)	Distance (μm)	MgO	Al_2O_3	SiO_2	CaO	Cr_2O_3	MnO	FeO	Total
#1	-0.9	25.6	n.d.	35.7	n.d.	n.d.	n.d.	39.9	101.2
#2	-0.6	25.2	n.d.	35.3	n.d.	0.4	n.d.	39.7	100.7
#3	-0.3	25.2	n.d.	35.0	n.d.	0.5	n.d.	39.4	100.1
#4	0	24.8	0.6	34.2	0.3	1.7	n.d.	39.9	101.5
#5	0.3	25.1	0.7	34.3	n.d.	2.4	n.d.	38.5	101.1
#6	0.6	27.7	n.d.	35.3	n.d.	1.0	n.d.	36.1	100.1
#7	0.9	29.8	n.d.	36.7	n.d.	0.6	n.d.	33.9	100.9
#8	1.2	31.5	n.d.	37.1	n.d.	n.d.	n.d.	31.4	100.0
#9	1.5	33.5	n.d.	38.0	n.d.	n.d.	n.d.	29.4	100.9
#10	1.8	35.4	n.d.	38.6	n.d.	n.d.	n.d.	27.7	101.6
#11	2.1	37.1	n.d.	38.8	n.d.	n.d.	n.d.	25.0	100.8
#12	2.4	38.3	n.d.	39.4	n.d.	n.d.	n.d.	23.3	101.0
#13	2.7	40.0	n.d.	39.4	n.d.	n.d.	n.d.	21.7	101.1
#14	3.0	41.1	n.d.	40.0	n.d.	n.d.	n.d.	19.9	101.0
#15	3.3	42.0	n.d.	39.7	n.d.	n.d.	n.d.	18.6	100.3
#16	3.6	42.4	n.d.	39.9	n.d.	n.d.	n.d.	17.9	100.2
#17	3.9	43.1	n.d.	40.3	n.d.	n.d.	n.d.	17.3	100.6
#18	4.2	43.5	n.d.	40.1	n.d.	n.d.	n.d.	16.5	100.0
#19	4.5	44.2	n.d.	40.5	n.d.	n.d.	n.d.	16.2	100.9
#20	4.8	44.5	n.d.	40.1	n.d.	n.d.	n.d.	15.8	100.3
#21	5.1	44.6	n.d.	40.2	n.d.	n.d.	n.d.	15.6	100.5
#22	5.4	44.9	n.d.	40.6	n.d.	n.d.	n.d.	15.6	101.2
#23	5.7	44.9	n.d.	40.4	n.d.	n.d.	n.d.	15.9	101.1
#24	6.0	45.3	n.d.	40.5	n.d.	n.d.	n.d.	15.3	101.1
#25	6.3	45.1	n.d.	40.6	n.d.	n.d.	n.d.	14.8	100.5
#26	6.6	45.3	n.d.	40.7	n.d.	n.d.	n.d.	15.5	101.5
#27	6.9	45.3	n.d.	40.4	n.d.	n.d.	n.d.	15.3	101.0

n.d.: not detected.

(g)	Distance (μm)	MgO	Al_2O_3	SiO_2	CaO	Cr_2O_3	FeO	Total
#1	4.2	50.0	n.d.	42.0	n.d.	n.d.	8.2	100.2
#2	3.9	50.6	n.d.	41.8	n.d.	n.d.	8.4	100.8
#3	3.6	50.4	n.d.	42.2	n.d.	n.d.	8.3	101.0
#4	3.3	50.5	n.d.	42.2	n.d.	n.d.	8.4	101.0
#5	3.0	50.3	n.d.	41.8	n.d.	n.d.	8.6	100.7
#6	2.7	50.4	n.d.	41.9	n.d.	n.d.	9.2	101.6
#7	2.4	50.1	n.d.	42.0	n.d.	n.d.	9.6	101.6
#8	2.1	49.7	n.d.	41.6	0.2	n.d.	10.1	101.7
#9	1.8	48.7	n.d.	41.7	n.d.	n.d.	11.0	101.4
#10	1.5	48.3	n.d.	41.4	n.d.	n.d.	12.7	102.4
#11	1.2	46.7	n.d.	40.9	n.d.	n.d.	14.3	102.0
#12	0.9	44.9	n.d.	40.1	n.d.	n.d.	16.8	101.8
#13	0.6	42.5	n.d.	40.1	n.d.	n.d.	20.0	102.6
#14	0.3	40.0	n.d.	38.9	n.d.	0.4	23.6	102.9
#15	0	36.4	0.7	37.5	n.d.	1.7	27.4	103.6
#16	-0.3	31.4	1.7	33.0	n.d.	7.9	32.7	106.8
#17	-0.3	30.2	1.7	32.8	n.d.	7.1	32.3	104.1
#18	0	32.3	0.9	34.8	n.d.	3.1	28.3	99.3
#19	0.3	35.0	n.d.	36.5	n.d.	1.5	25.1	98.1
#20	0.6	38.2	n.d.	37.9	n.d.	0.8	21.5	98.3
#21	0.9	40.9	n.d.	38.8	n.d.	n.d.	18.2	97.9
#22	1.2	43.0	n.d.	39.9	n.d.	n.d.	15.6	98.5
#23	1.5	44.7	n.d.	40.8	n.d.	n.d.	12.9	98.3
#24	1.8	46.2	n.d.	40.4	n.d.	n.d.	11.5	98.1
#25	2.1	47.8	n.d.	41.3	n.d.	n.d.	9.9	99.0
#26	2.4	49.0	n.d.	41.8	n.d.	n.d.	9.4	100.1
#27	2.7	49.6	n.d.	41.7	n.d.	n.d.	9.2	100.5

n.d.: not detected.

(continued)

(g)	Distance (μm)	MgO	Al_2O_3	SiO_2	CaO	Cr_2O_3	FeO	Total
#28	3.0	50.1	n.d.	41.9	n.d.	n.d.	8.4	100.4
#29	3.3	50.6	n.d.	41.8	0.2	n.d.	8.0	100.7
#30	3.6	51.0	n.d.	41.8	n.d.	n.d.	7.7	100.4
#31	3.9	51.1	n.d.	41.9	n.d.	n.d.	7.6	100.6
#32	4.2	51.2	n.d.	41.8	n.d.	n.d.	7.4	100.5
#33	4.5	51.5	n.d.	42.3	n.d.	n.d.	7.3	101.1
#34	4.8	51.1	n.d.	41.5	n.d.	n.d.	7.2	99.8
#35	5.1	51.5	n.d.	42.6	n.d.	n.d.	6.9	101.0
#36	5.4	51.6	n.d.	41.8	n.d.	n.d.	7.0	100.4
#37	5.7	51.5	n.d.	42.1	n.d.	n.d.	6.8	100.4

n.d.: not detected.

(h)	Distance (μm)	MgO	Al_2O_3	SiO_2	SO_3	Cr_2O_3	FeO	NiO	Total
#1	3.6	44.5	n.d	40.4	n.d	n.d	15.9	n.d	100.8
#2	3.3	44.5	n.d	40.4	n.d	n.d	15.8	n.d	100.6
#3	3.0	44.4	n.d	40.1	n.d	n.d	16.4	n.d	100.9
#4	2.7	44.6	n.d	40.8	n.d	n.d	16.9	n.d	102.2
#5	2.4	43.9	n.d	40.4	n.d	n.d	17.2	n.d	101.6
#6	2.1	43.4	n.d	40.0	n.d	n.d	17.9	n.d	101.3
#7	1.8	42.6	n.d	39.6	n.d	n.d	18.7	n.d	100.9
#8	1.5	42.3	n.d	40.0	n.d	n.d	19.6	n.d	101.9
#9	1.2	41.0	n.d	39.7	n.d	n.d	20.7	n.d	101.4
#10	0.9	40.1	n.d	39.0	n.d	n.d	23.1	n.d	102.1
#11	0.6	38.1	n.d	38.4	1.2	n.d	25.0	n.d	102.7
#12	0.3	35.7	n.d	37.0	3.4	n.d	27.2	n.d	103.3
#13	0	31.5	0.6	33.6	9.3	0.6	31.4	2.0	109.0
#14	-0.3	18.9	1.2	20.3	39.6	0.7	37.1	15.2	132.9
#15	-0.6	21.9	2.0	27.0	17.0	0.7	37.6	4.1	110.2
#16	-0.9	21.0	1.9	28.7	9.6	0.8	36.6	1.9	100.5
#17	-1.2	23.4	2.7	29.0	8.4	1.2	38.6	1.3	104.6
#18	-0.9	23.6	2.2	28.6	11.9	1.0	37.7	2.3	107.2
#19	-0.6	25.6	1.0	29.7	16.2	0.5	37.3	4.1	114.2
#20	-0.3	28.7	0.6	33.2	8.4	n.d	32.8	1.9	105.6
#21	0	31.5	n.d	35.6	3.4	n.d	29.5	n.d	100.0
#22	0.3	34.1	n.d	37.2	1.3	n.d	26.5	n.d	99.1
#23	0.6	36.7	n.d	38.5	n.d	n.d	23.8	n.d	99.0
#24	0.9	38.7	n.d	39.1	n.d	n.d	21.1	n.d	98.9
#25	1.2	40.4	n.d	39.6	n.d	n.d	19.2	n.d	99.1
#26	1.5	41.7	n.d	40.1	n.d	n.d	17.5	n.d	99.3
#27	1.8	43.3	n.d	40.2	n.d	n.d	16.3	n.d	99.8

n.d.: not detected.

(continued)

(h)	Distance (μm)	MgO	Al_2O_3	SiO_2	SO_3	Cr_2O_3	FeO	NiO	Total
#28	2.1	44.1	n.d	40.1	n.d	n.d	15.6	n.d	99.8
#29	2.4	44.5	n.d	40.2	n.d	n.d	14.9	n.d	99.6
#30	2.7	45.3	n.d	40.8	n.d	n.d	15.0	n.d	101.1
#31	3.0	45.5	n.d	40.4	n.d	n.d	14.4	n.d	100.2
#32	3.3	46.1	n.d	40.4	n.d	n.d	14.8	n.d	101.3
#33	3.6	45.9	n.d	40.8	n.d	n.d	14.6	n.d	101.3
#34	3.9	46.0	n.d	40.5	n.d	n.d	14.8	n.d	101.3
#35	4.2	45.8	n.d	40.4	n.d	n.d	14.2	n.d	100.5
#36	4.5	45.9	n.d	40.5	n.d	n.d	14.1	n.d	100.5

Table 14. Oxygen diffusion distance from $\delta^{18}O$ isotopograph.

	analysis No	diffusion distance
(a)	1	3.4
	2	2.1
	3	2.9
	4	1.8
	5	1.5
	6	2.2
	7	1.8
(b)	1	2.4
	2	1.7
	3	1.5
(c)	1	1.5
	2	2.7
	3	2.0
	4	1.5
(d)	1	1.8
	2	1.6
	3	2.5
	4	1.5
	5	2.2
	6	1.5
(f)	1	1.4
	2	2.2
	3	2.2
	average	2.0
	SD	0.5

REFERENCES

Amelin Y., Krot A. N., Hutcheon I. D. and Ulyanov A. N. (2002) Lead isotopic ages of chondrules and Calcium-Aluminum-rich inclusions. *Science* **297**, 1678–1683.

Allen J. S., Nozette S. and Wilkening L. L. (1980) A study of chondrule rims and chondrule irradiation records in unequilibrated ordinary chondrites. *Geochimica et Cosmochimica Acta* **44**, 1161–1175.

Andersson K., Borchardt G., Scherrer S. and Weber S. (1989) Self-diffusion in Mg_2SiO_4 (forsterite) at high temperature, *Fresen. Z. Analytische Chemie* **333**, 383–385.

Ando K., Kurokawa H. and Oishi Y. (1981) Self-diffusion coefficient of oxygen in single-crystal forsterite. *Journal of the American Ceramic Society* C-30.

Ashworth J.R. (1977) Matrix textures in unequilibrated ordinary chondrites. *Earth and Planetary Science Letters* **35**, 25–34.

Brearley A. J. (2003) Nebular versus parent-body processing. Meteorites, Comets, and Planets, ed. by A. M. Davis. Oxford, Elsevire-Pergamon, 247–269 (Treatise on Geochemistry, ed. by H. D. Holland and K. K. Turekian, Vol. 1).

Brearley A. J. and Krot A. N. (2013) Metasomatism in the early solar system: The record from chondritic meteorites. In *Metasomatism and the Chemical Transformation of Rock Lecture Notes in Earth System Sciences*. 659–789.

Chakraborty S. (1997) Rates and mechanisms of Fe-Mg interdiffusion in olivine at 980°C-1300°C. *Journal of Geophysical Research* **102**, 12317–12331.

Connelly J. N., Bizzarro M., Krot A. N., Nordlund Å, Wielandt D. and Ivanova M. A. (2012) The absolute chronology and thermal processing of solids in the solar protoplanetary disk. *Science* **338**, 651–655.

Cuvillier P., Leroux H., Jacob D. and Hirel P. (2015) Fe-Mg interdiffusion profiles in rimmed forsterite grains in the Allende matrix: Time-temperature constraints for the parent body metamorphism. *Meteoritics & Planetary Science* **50**, 1529–1545.

Dohmen R., Chakraborty S. and Becker H.-W. (2002) Si and O diffusion in olivine and implications for characterizing plastic flow in the mantle. *Geophysical Research Letters* **29**, 26-1–26-4.

Dohmen R., Becker H.-W. and Chakraborty S. (2007) Fe-Mg diffusion in olivine I:

Experimental determination between 700°C and 1,200°C as a function of composition, crystal orientation and oxygen fugacity. *Physics and Chemistry of Minerals* **34**, 389–407.

Dohmen R. and Chakraborty S. (2007) Fe-Mg diffusion in olivine II: Point defect chemistry, change of diffusion mechanisms and a model for calculation of diffusion coefficients in natural olivine. *Physics and Chemistry of Minerals* **34**, 409–430.

Gérard O. and Jaoul O. (1989) Oxygen diffusion in San Carlos olivine. *Journal of Geophysical Research* **94**, 4119–4128.

Gooding J. L., Keil K., Fukuoka T. and Schimit R. A. (1980) Elemental abundances in chondrules from unequilibrated chondrites: Evidence for chondrule origin by melting of pre-existing materials. *Earth and Planetary Science Letters* **50**, 171–180.

Grossman J. N. and Wasson J. T. (1982) Evidence for primitive nebular components in chondrules from the Chainpur chondrite. *Geochimica et Cosmochimica Acta* **46**, 1081–1099.

Grossman L. (1972) Condensation in the primitive solar nebula. *Geochimica et Cosmochimica Acta* **36**, 597–619.

Grossman L., Fedkin A. V. and Simon S. B. (2012) Formation of the first oxidized iron in the solar system. *Meteoritics & Planetary Science* **47**, 2160–2169.

Hewins R. H. (1996) Chondrules and the protoplanetary disk: an overview. In *Chondrules and the Protoplanetery Disk* (eds. by Hewins R. H., Jones R. H. and Scotte E. R. D.), pp. 3–9. Cambridge University Press.

Hewins R. H., Connolly Jr. H. C., Lofgren G. E. and Libourel G. (2005) Experimental constraints on chondrule formation. In Chondrites and the Protoplanetary Disk (eds. by Krot A. N., Scott E. R. D. and Reipurth B) ASP Conference Series 341. pp. 286–316.

Huss G. R., Rubin A. E. and Grossman J. N. (2006) Thermal metamorphism in chondrites. In Meteorites and the Early Solar System II (eds. by Lauretta, D.S. and McSween, H.Y.), pp. 567-586. University of Arizona, Houston.

Ito M. and Messenger S. (2010) Thermal metamorphic history of a Ca, Al-rich inclusion constrained by high spatial resolution Mg isotopic measurements with NanoSIMS 50L. *Meteoritics & Planetary Science* **45**, 583–595.

Jaoul O., Froidevaux C., Durham W. B. and Michaut M. (1980) Oxygen self-diffusion in forsterite: Implications for the high-temperature creep

mechanism. *Earth and Planetary Science Letters* **47**, 391–397.

Jaoul O., Houlier B. and Abel F. (1983) Study of ^{18}O diffusion in magnesium orthosilicate by nuclear microanalysis, *Journal of Geophysical Research* **88**, 613–624.

Keil K. (2000) Thermal alteration of asteroids: evidence from meteorites. P*lanetary and Space Science* **48**, 887–903.

King T. V. V. and King E. A. (1981) Accretionary dark rims in unequilibrated chondrites. *Icarus* **48**, 460–472.

Komatsu M., Fagan T. J., Mikouchi T., Petaev M. I. and Zolensky M.E. (2015) LIME silicates in amoeboid olivine aggregates in carbonaceous chondrites: Indicator of nebular and asteroidal processes. *Meteoritics & Planetary Science* **50**, 1271–1294.

Krot A. N. and Wasson J. T. (1995) Igneous rims on low-FeO and high-FeO chondrules in ordinary chondrites. *Geochimica et Cosmochimica Acta* **59**, 4951–4966.

Krot A. N., Scott E. R. D. and Zolensky M. E. (1995) Mineralogical and chimerical modification of components in CV3 condrites: Nebular or asteroidal processing? *Meteoritics* **30**, 748–776.

Krot A. N., Petaev M. I., Scott E. R. D., Choi B.-G., Zolensky M. E. and Keil K. (1998) Progressive alteration in CV3 chondrites: More evidence for asteroidal alteration. *Meteoritics & Planetary Science* **33**, 1065–1085.

Krot A. N., Petaev M. I. and Bland P. A. (2004) Multiple formation mechanisms of ferrous olivine in CV carbonaceous chondrites during fluid-assisted metamorphism. *Antarctic Meteorite Research* **17**, 153–171.

Kunihiro T., Nagashima K., Takayanagi I., Nakamura J., Kosaka K. and Yurimoto H. (2001) Noise characteristics of stacked CMOS active pixel sensor for charged particles. *Nuclear Instruments and Methods in Physics Research* **470,** 512–519.

Maruyama S., Yurimoto H. and Sueno S. (1999) Oxygen isotope evidence regarding the formation of spinel-bearing chondrules. *Earth and Planetary Science Letters* **169**, 165–171.

Maruyama S. and Yurimoto H. (2003) Relationship among O, Mg isotopes and the petrography of two spinel-bearing compound chondrules. *Geochimica et Cosmochimica Acta* **67**, 3943–3957.

Matsumoto K., Yurimoto H., Kosaka K., Miyata K., Nakamura T. and Sueno S. (1993) A novel ion imager for secondary ion mass spectrometry. *IEEE*

TRANSACTIONS ON ELECTRON DEVICES **40**, 82–85.

Myers J. and Eugster H.P. (1983) The system Fe-Si-O: oxygen buffer calibrations to 1,500 K. *Contributions to Mineralogy and Petrology* **82**, 75–90.

Nagashima K., Kunihiro T., Takayanagi I., Nakamura J., Kosaka K. and Yurimoto H. (2001) Output characteristics of stacked CMOS-type active pixel sensor for charged particles. *Surface and interface analysis* **31**, 131–137.

Nagashima K., Takeda Y., Itoh S. and Yurimoto H. (2003) ^{16}O-rich olivine in igneous rim of type I chondrule from CR2 chondrite. 66th Annual meeting of the Meteoritical Society, 5140 (abstract).

Nagashima K., Krot A. N. and Huss G. R. (2011) Oxygen-Isotope Compositions of Chondrules and Matrix Grains in Kakangari Chondrite. *Workshop on Formation of the First Solids in the Solar System*, 9049 (abstract).

Nagashima K., Krot A. N., Libourel G. and Huss G. R. (2013) Magnesian porphyritic chondrules surrounded by ferroan igneous rims from CR chondrite GRA 95229. 44th Lunar and Planetary Science Conference, 1780 (abstract).

Nagashima K., Krot A. N. and Huss G. R. (2015) Oxygen-isotope compositions of chondrule phenocrysts and matrix grains in Kakangari K-grouplet chondrite: Implication to a chondrule-matrix genetic relationship. *Geochimica et Cosmochimica Acta* **151**, 49–67.

Nakamura A. and Schmalzried H. (1984) On the Fe^{2+}-Mg^{2+}-interdiffusion in olivine (II). *Ber Bunsenges Phys Chem* **88**, 140–145.

Oishi Y. and Ando K. (1984) Oxygen self-diffusion coefficient in single-crystal forsterite. *In Materials Science of the Earth's Interior* (ed. by Sunagawa I.). Terra Science Publishing Company, Tokyo, Japan, pp. 271–280.

Park C., Wakaki S., Sakamoto N., Kobayashi S. and Yurimoto H. (2012) Oxygen isotopic composition of the solar nebula gas inferred from high-precision isotope imaging of melilite crystals in an Allende CAI. *Meteoritics & Planetary Science* **47**, 2070–2083.

Reddy K. P. R., Oh S. M., Major Jr., L. D. and Cooper A. R. (1980) Oxygen diffusion in forsterite. *Journal of Geophysical Research* **85**, 322–326.

Righter K. and Neff K. E. (2007) Temperature and oxygen fugacity constraints on CK and R chondrites and implications for water and oxidation in the early solar system. *Polar science* **1**, 25–44.

Russell S. S., Zolensky M., Righter K., Folco L., Jones R., Connolly Jr. H. C., Grady M. M. and Grossman J. N. (2005) The Meteoritical Bulletin, No. 89, 2005

September. *Meteoritics & Planetary Science* **40**, 201–263.

Rubin A. E. (1984) Coarse-grained chondrule rims in type 3 chondrites. *Geochimica et Cosmochimica Acta* **48**, 1779–1789.

Rubin A. E. and Wasson J. T. (1987) Chondrules, matrix and coarse-grained chondrule rims in the Allende meteorite: Origin, interrelationships, and possible precursor components. *Geochimica et Cosmochimica Acta* **51**, 1923–1937.

Ryerson F. J., Durham W.B., Cherniak D. J. and Lanford W. A. (1989). Oxygen diffusion in olivine: Effect of oxygen fugacity and implications for creep, *Journal of Geophysical Research* **94**, 4105–4118.

Sakamoto N. and Yurimoto H. (2006) Highly sensitive ion imaging system using direct combination of a stacked-type solid-state imager and a microchannel plate driven by LabVIEW software. *Surface and interface analysis* **38**, 1760–1762.

Sakamoto N., Seto Y., Itoh S., Kuramoto K., Fujino K., Nagashima K., Krot A. N. and Yurimoto H. (2007) Remnants of the early solar system water enriched in heavy oxygen isotopes. *Science* **317**, 231–233.

Scott E. R. D., Rubin A. E., Taylor G. J. and Keil K. (1984) Matrix material in type 3 chondrites - Occurrence, heterogeneity and relationship with chondrules. *Geochimica et Cosmochimica Acta* **48**, 1741–1757.

Soulié C., Libourel G. and Tissandier L. (2017) Olivine dissolution in molten silicates: An experimental study with application to chondrule formation. *Meteoritics & Planetary Science* **52**, 225–250.

Tachibana S., Tamada S., Kawasaki H., Ozawa K. and Nagahara H. (2013) Interdiffusion of Mg-Fe in olivine at 1,400-1,600 °C and 1 atm total pressure. *Physics and Chemistry of Minerals* **40**, 511–519.

Takayanagi I., Nakamura J., Fossum E. R., Nagashima K., Kunihoro T. and Yurimoto H. (2003) Dark current reduction in stacked-type CMOS-APS for charged particle imaging. *IEEE TRANSACTIONS ON ELECTRON DEVICES* **50**, 70–76.

Takeda Y., Itoh S. and Yurimoto H. (2002) Oxygen isotopic composition in a CR chondrule. *Japan Geoscience Union Meeting* (abstract).

Tenner T. J., Nakashima D., Ushikubo T., Kita N. T. and Weisberg M. K. (2015) Oxygen isotope ratios of FeO-poor chondrules in CR3 chondrites: Influence of dust enrichment and H_2O during chondrule formation. *Geochimica et Cosmochimica Acta* **148**, 228–250.

Tenner T. J., Ushikubo T., Nakashima D., Schrader D. L., Weisberg M. K., Kimura M. and Kita N. (2018) Oxygen isotope characteristics of chondrules from recent studies by secondary ion mass spectrometry. In Chondrules (eds. by Russell S. S., Connolly Jr. H. C., Krot A. N.), pp. 196–246, Cambridge University Press

Weinbruch S., Armstrong J. and Palme H. (1994) Constraints on the thermal history of the Allende parent body as derived from olivine-spinel thermometry and Fe/Mg interdiffusion in olivine. *Geochimica et Cosmochimica Acta* **58**, 1019–1030.

Yamamoto K., Sakamoto N. and Yurimoto H. (2010) Analysis of the noise properties of a solid-state SCAPS ion imager and development of software noise reduction. *Surface and interface analysis* **42**, 1603–1605.

Yurimoto H., Nagashima K., and Kunihiro T. (2003) High precision isotope micro-imaging of materials. *Applied Surface Science* **203-204**, 793–797.

Yurimoto H., Krot A. N., Choi B.-G., Aléon J., Kunihiro T. and Brearley A. J. (2008) Oxygen isotopes in chondritic components. In Oxygen in the Solar System (ed. by MacPherson G. J.). Reviews in Mineralogy and Geochemistry, vol. 68. Mineralogical Society of America, Washington, DC. pp. 141–186.

Yurimoto H., Abe K., Abe M., Ebihara M., Fujimura A., Hashiguchi M., Hashizume K., Ireland T. R., Itoh S., Katayama J., Kato C., Kawaguchi J., Kawasaki N., Kitajima F., Kobayashi S., Meike T., Mukai T., NagaoK., Nakamura T., Naraoka H., Noguchi T., Okazaki R., Park C., Sakamoto N., Seto Y., Takei M., Tsuchiyama A., Uesugi M., Wakaki S., Yada T., Yamamoto K., Yoshikawa M. and Zolensky M. E. (2011) Oxygen isotopic compositions of asteroidal materials returned from Itokawa by the Hayabusa mission. *Science* **333,** 1116–1119.

APPENDIX

Appendix 1. Quantitative analysis locations of olivine in the chondrule.....86

Appendix 2. Quantitative analysis locations of nepheline, plagioclace and augite in the chondrule.....87

Appendix 3. Quantitative analysis locations of Fe-Ni metal, Fe sulfide and metal sulfide in the chondrule.....88

Appendix 4. Quantitative analysis locations of olivine in the igneous rim.....90

Appendix 5. Quantitative analysis locations of feldspathic glass, nepheline, enstatite, pigeonite and augite in the igneous rim 93

Appendix 6. Quantitative analysis locations of Fe-Ni sulfide in the igneous rim..99

Appendix 7. Measurement locations for oxygen isotopes of olivine in the igneous rim.....104

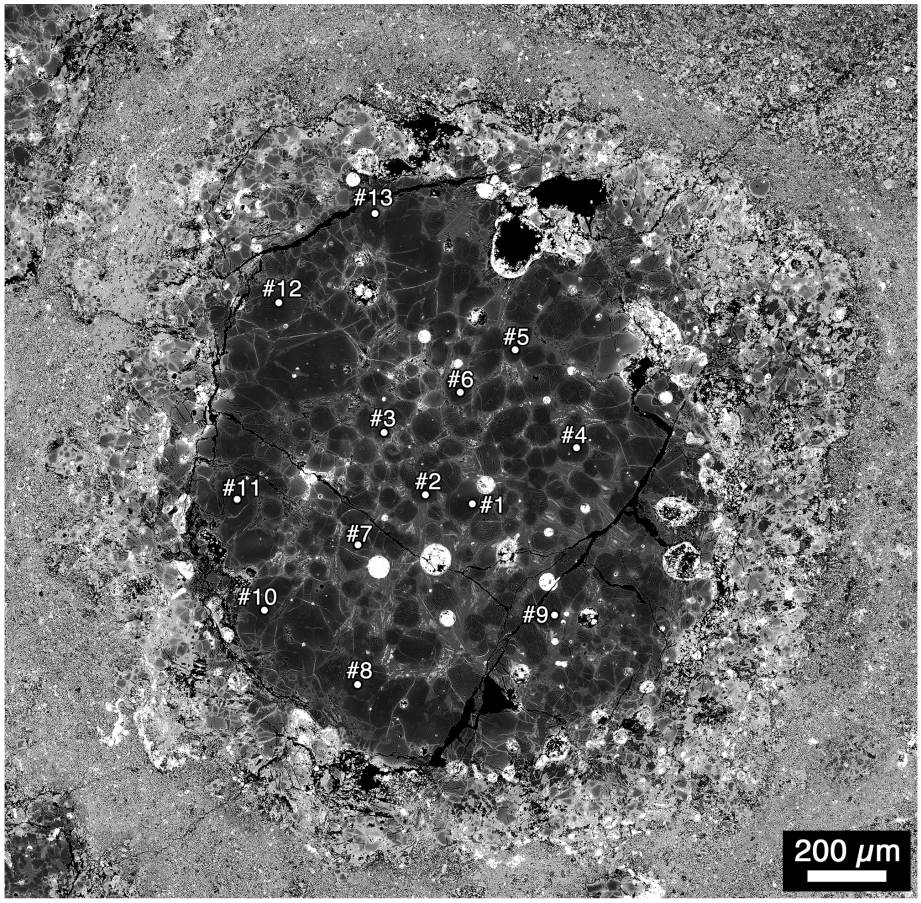

Fig. A1. Back-scattered electron images of type I chondrule surrounded by FeO-rich igneous rim in NWA3118 CV chondrite. White circles show locations of quantitative analyses of olivine in the chondrule. Numbers correspond to Table 1.

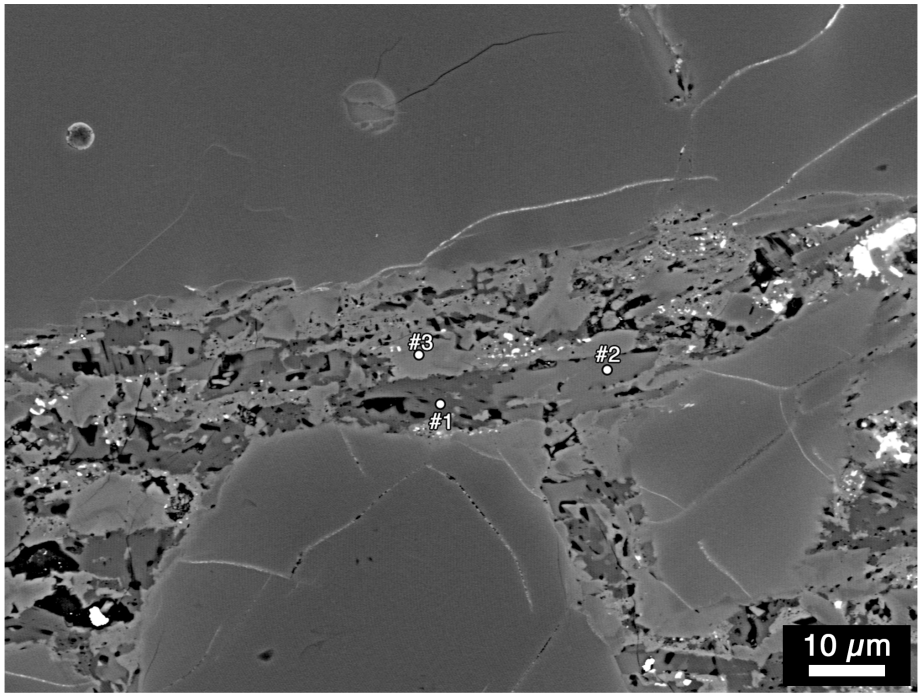

Fig. A2. White circles show locations of quantitative analyses of nepheline, plagioclace and augite in the chondrule. Numbers correspond to Table 2.

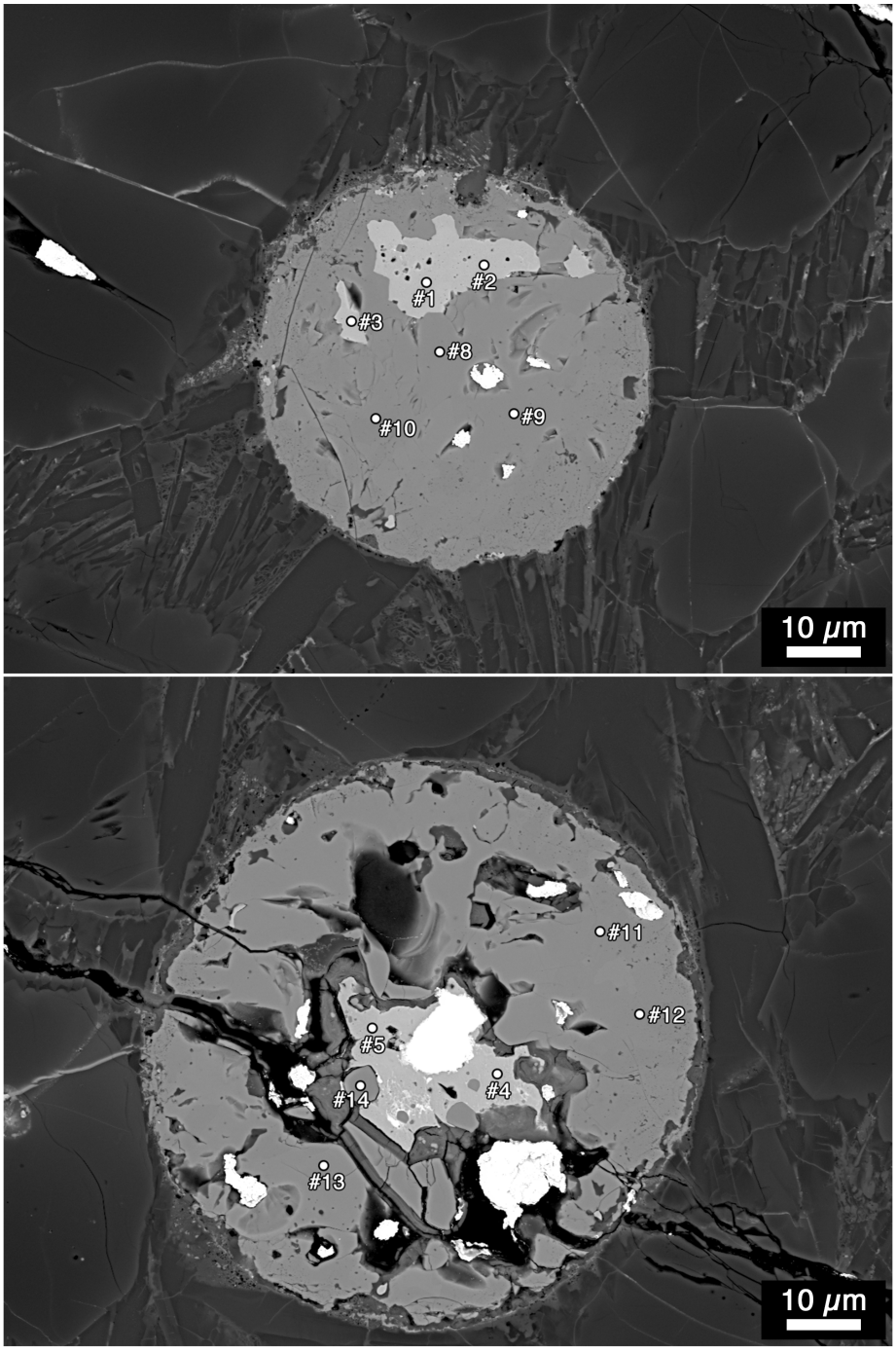

Fig. A3. White circles show locations of quantitative analyses of Fe-Ni metal, Fe sulfide and metal sulfide in the chondrule. Numbers correspond to Table 3.

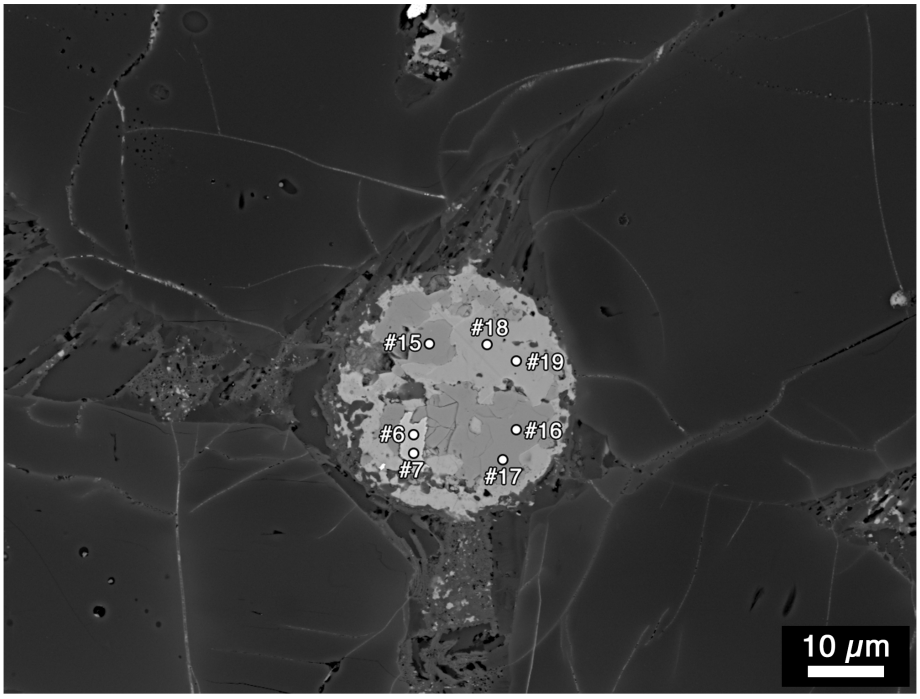

Fig. A3. (continued)

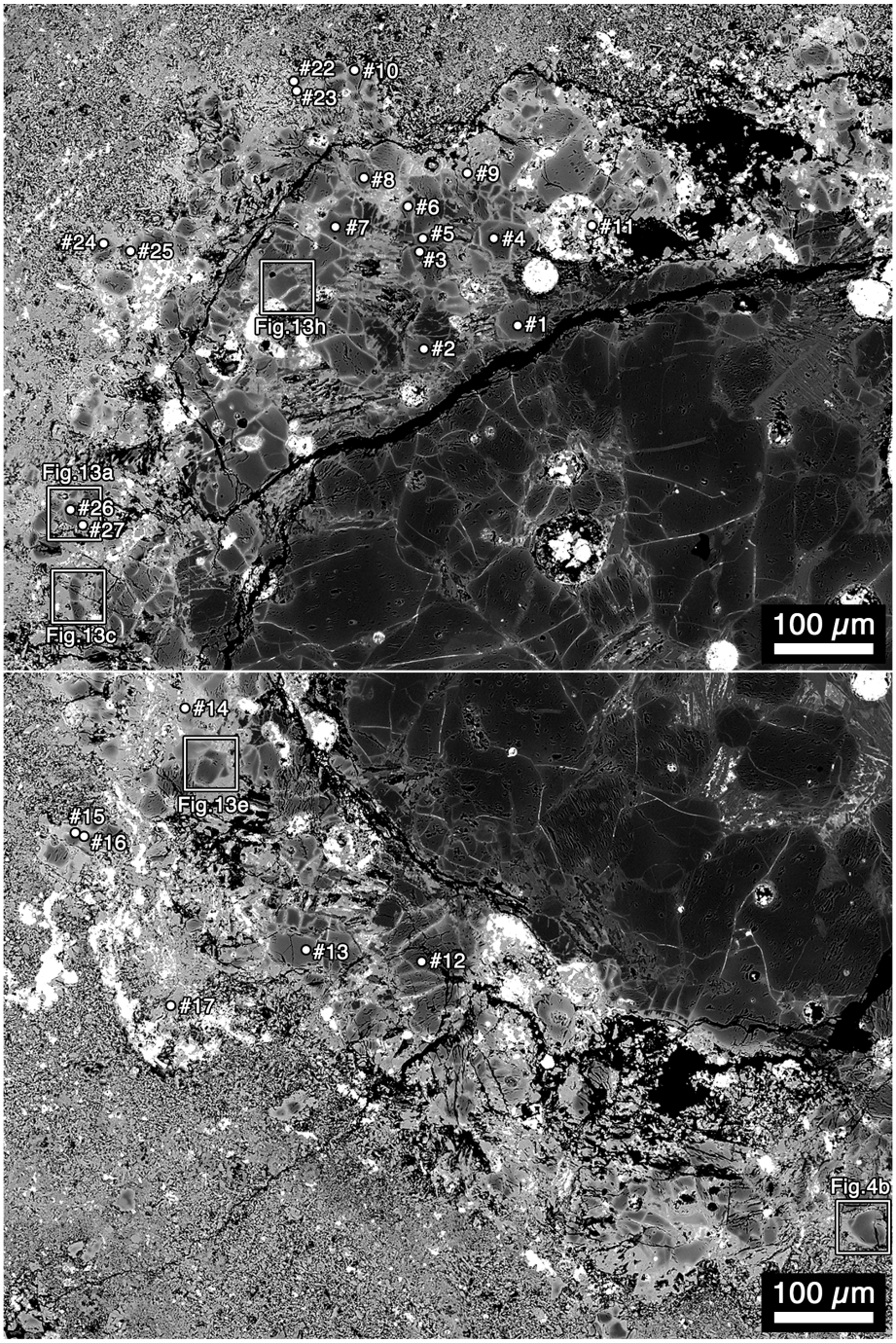

Fig. A4. White circles show locations of quantitative analyses of olivine in the igneous rim. Numbers correspond to Table 4. White squares indicate locations of line profile analyses shown in Fig. 13.

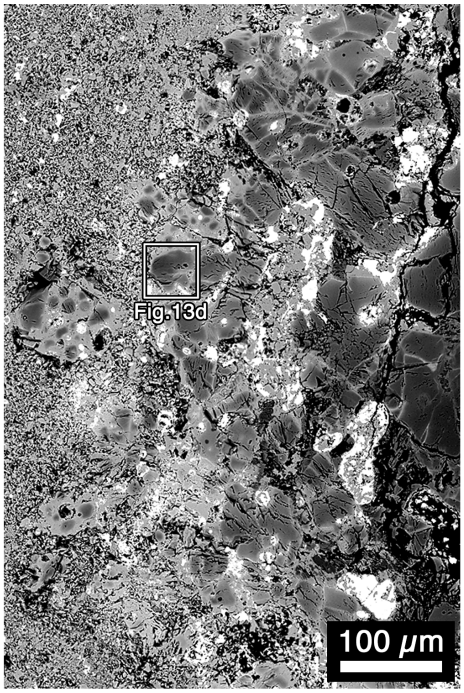

Fig. A4. (Continued)

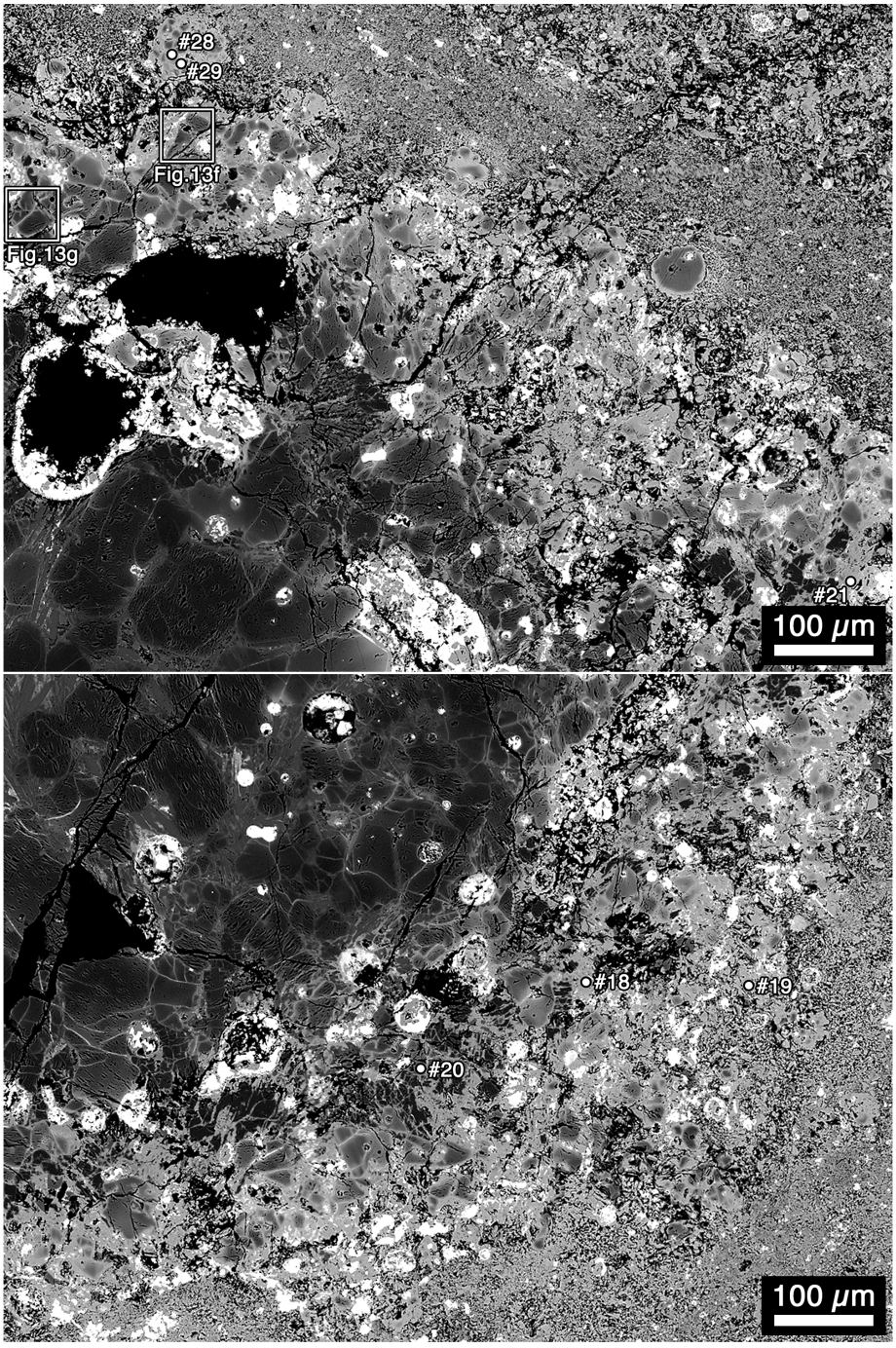

Fig. A4. (Continued)

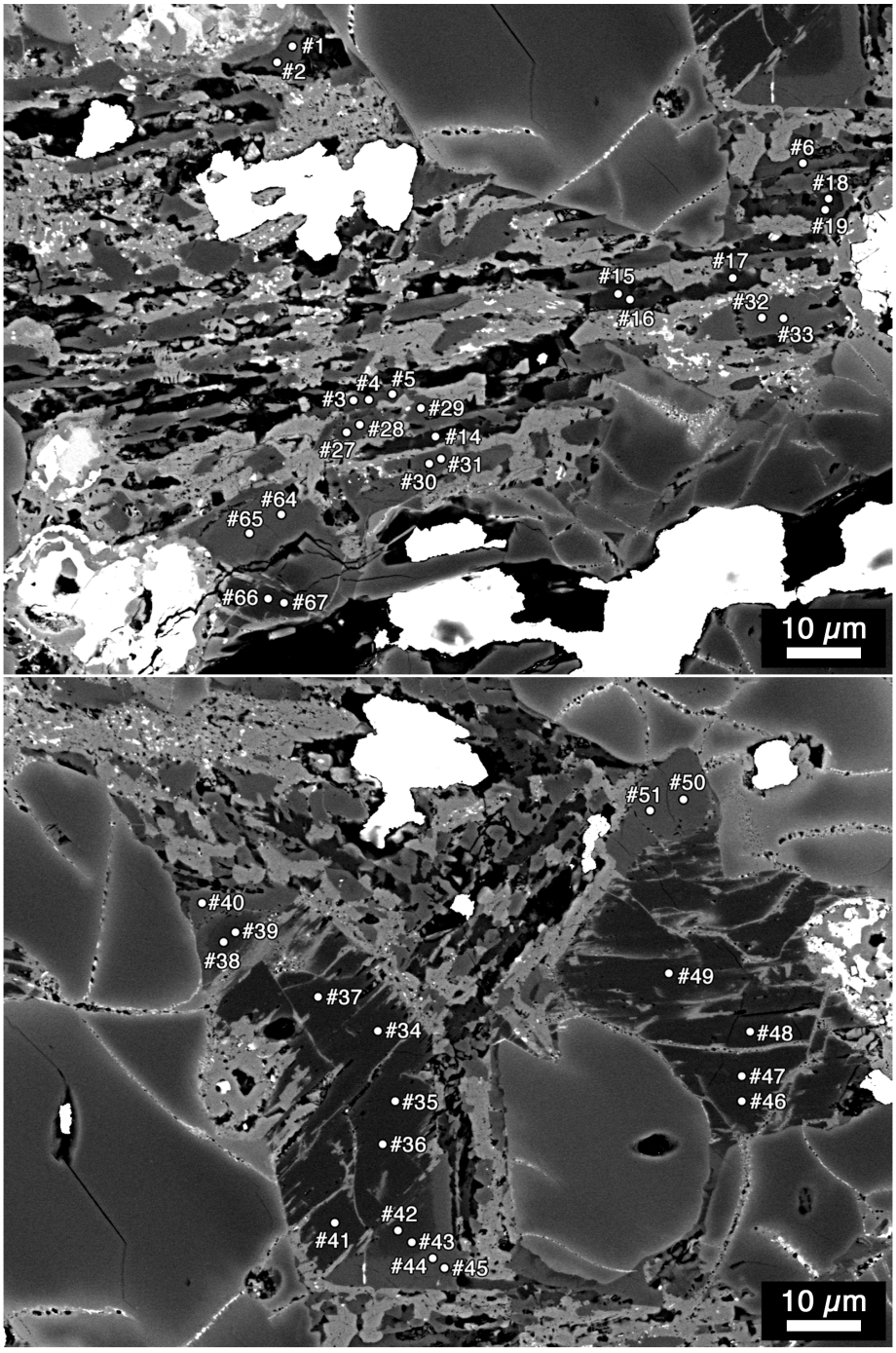

Fig. A5. White circles show locations of quantitative analyses of feldspathic glass, nepheline, enstatite, pigeonite and augite in the igneous rim. Numbers correspond to Tables 5-7.

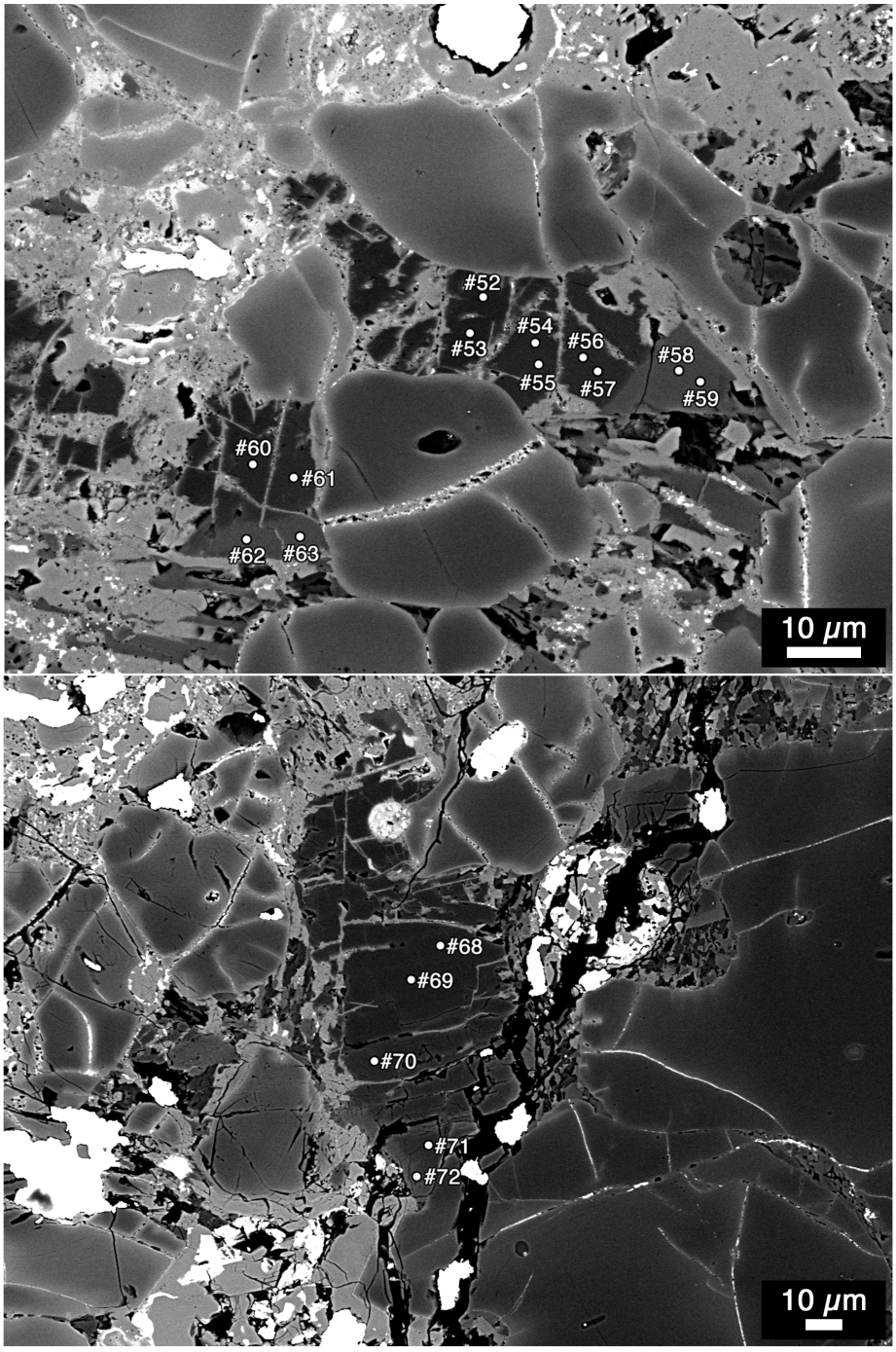

Fig. A5. (Continued)

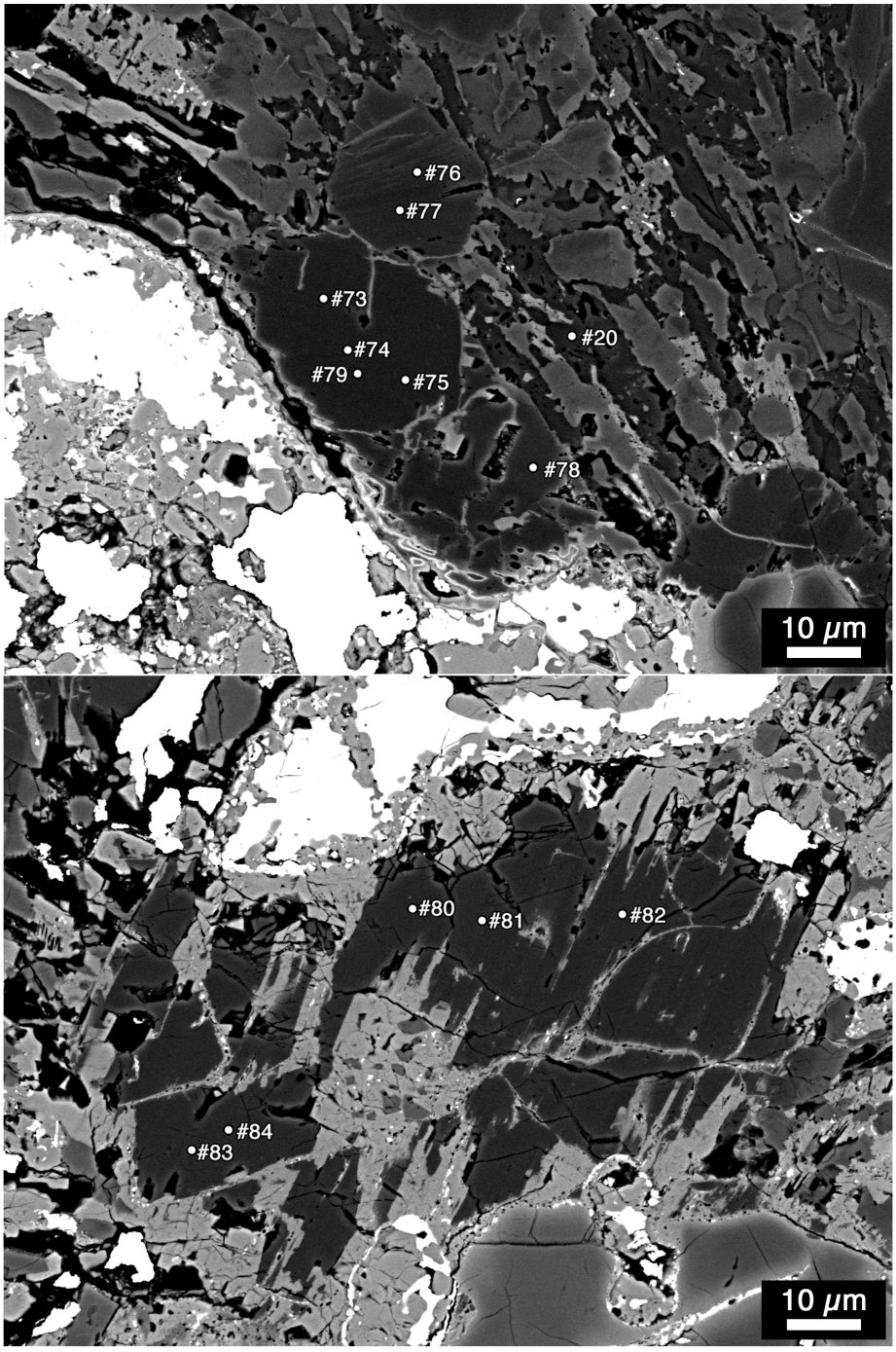

Fig. A5. (Continued)

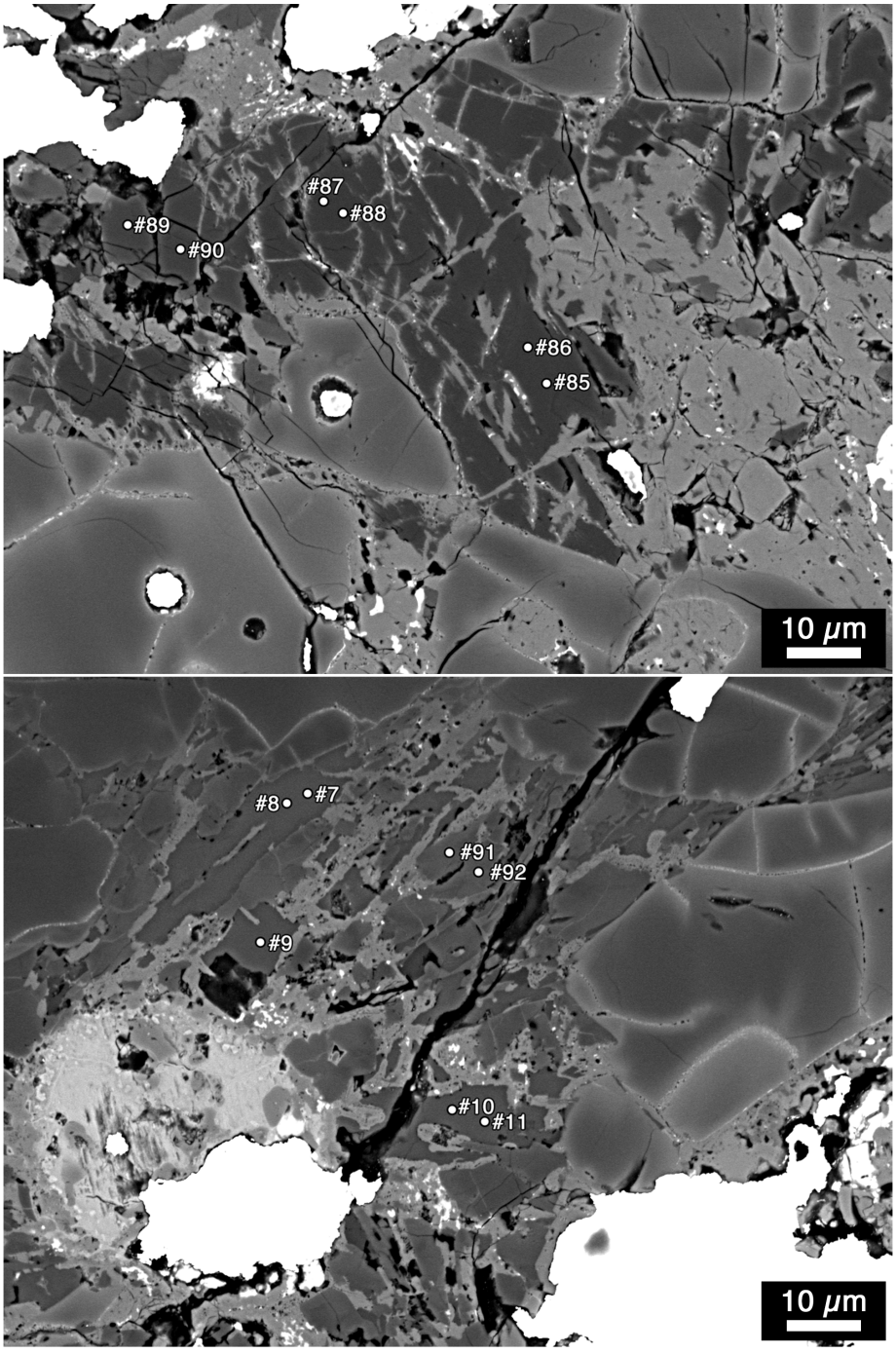

Fig. A5. (Continued)

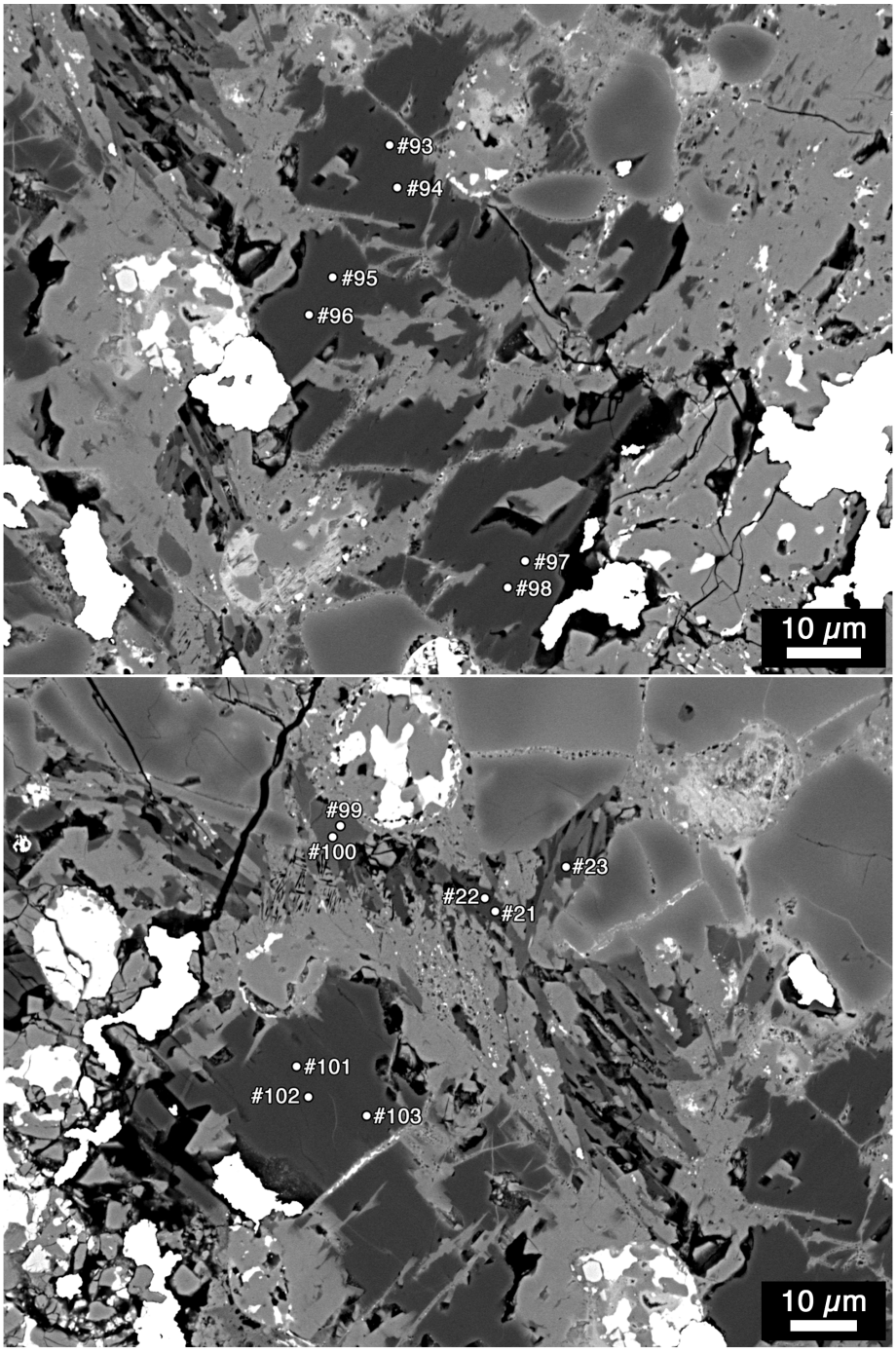

Fig. A5. (Continued)

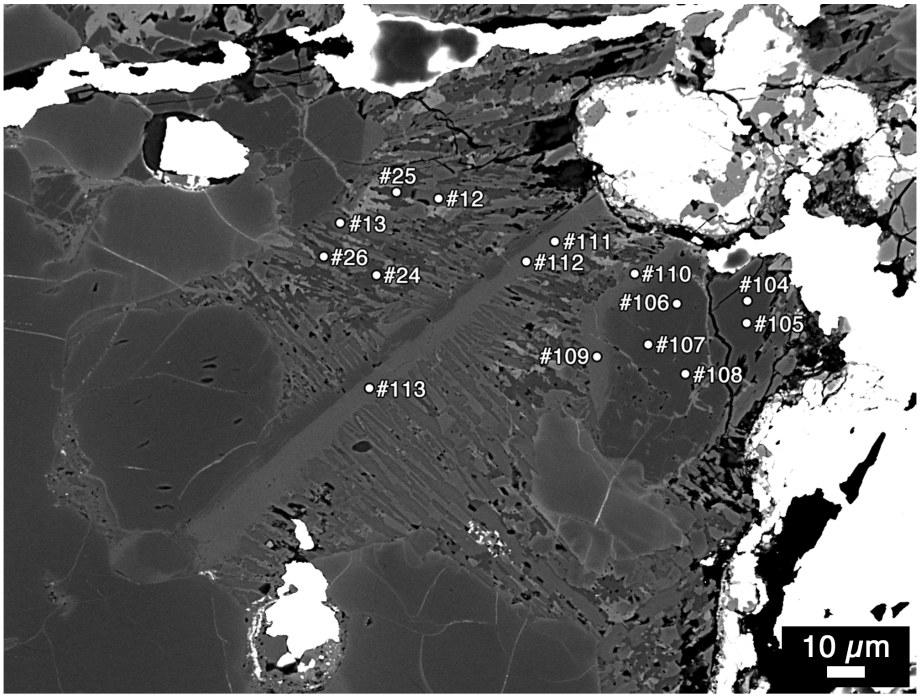

Fig. A5. (Continued)

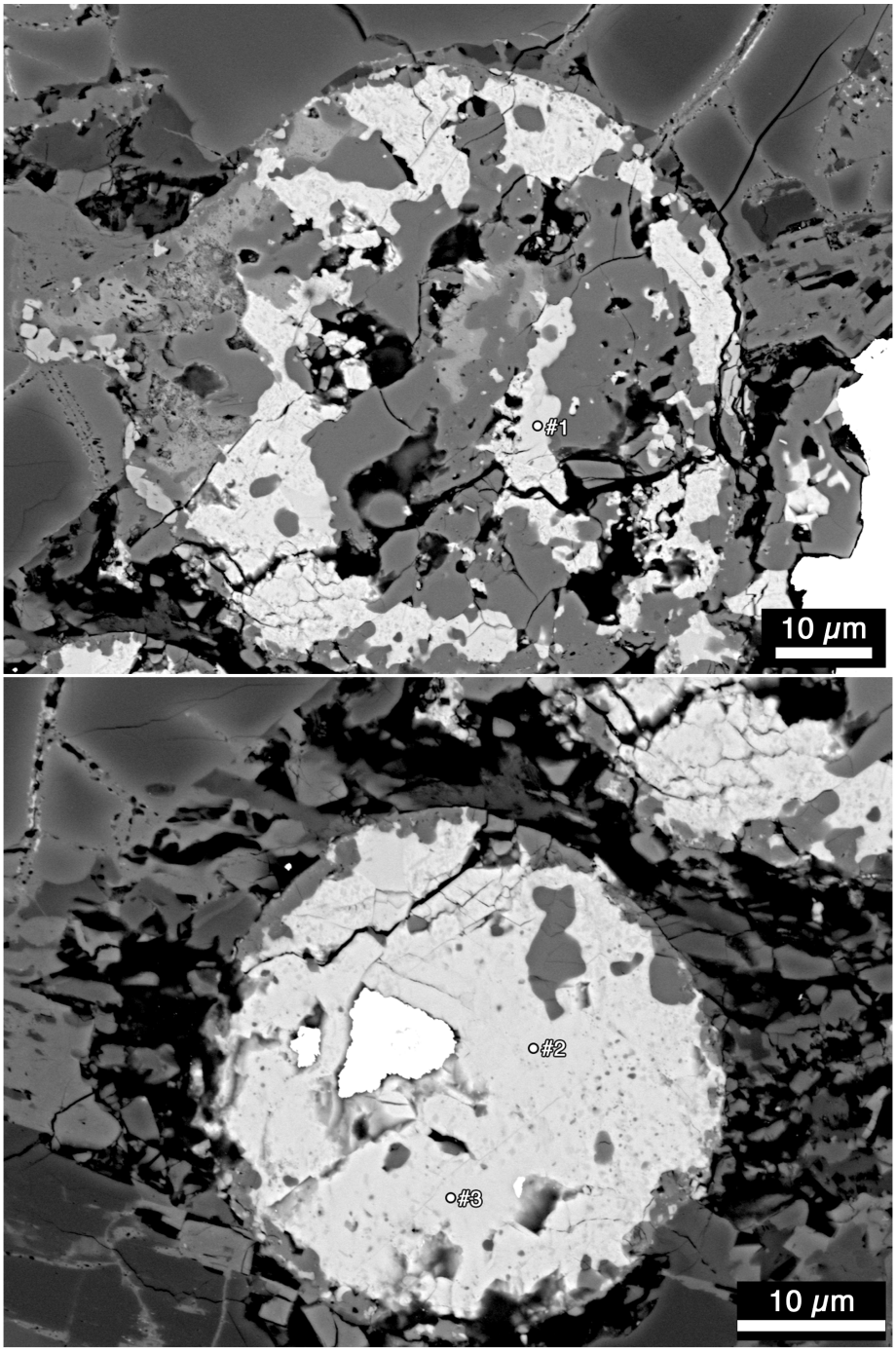

Fig. A6. White circles show locations of quantitative analyses of Fe-(Ni) sulfide in the igneous rim. Numbers correspond to Table 8.

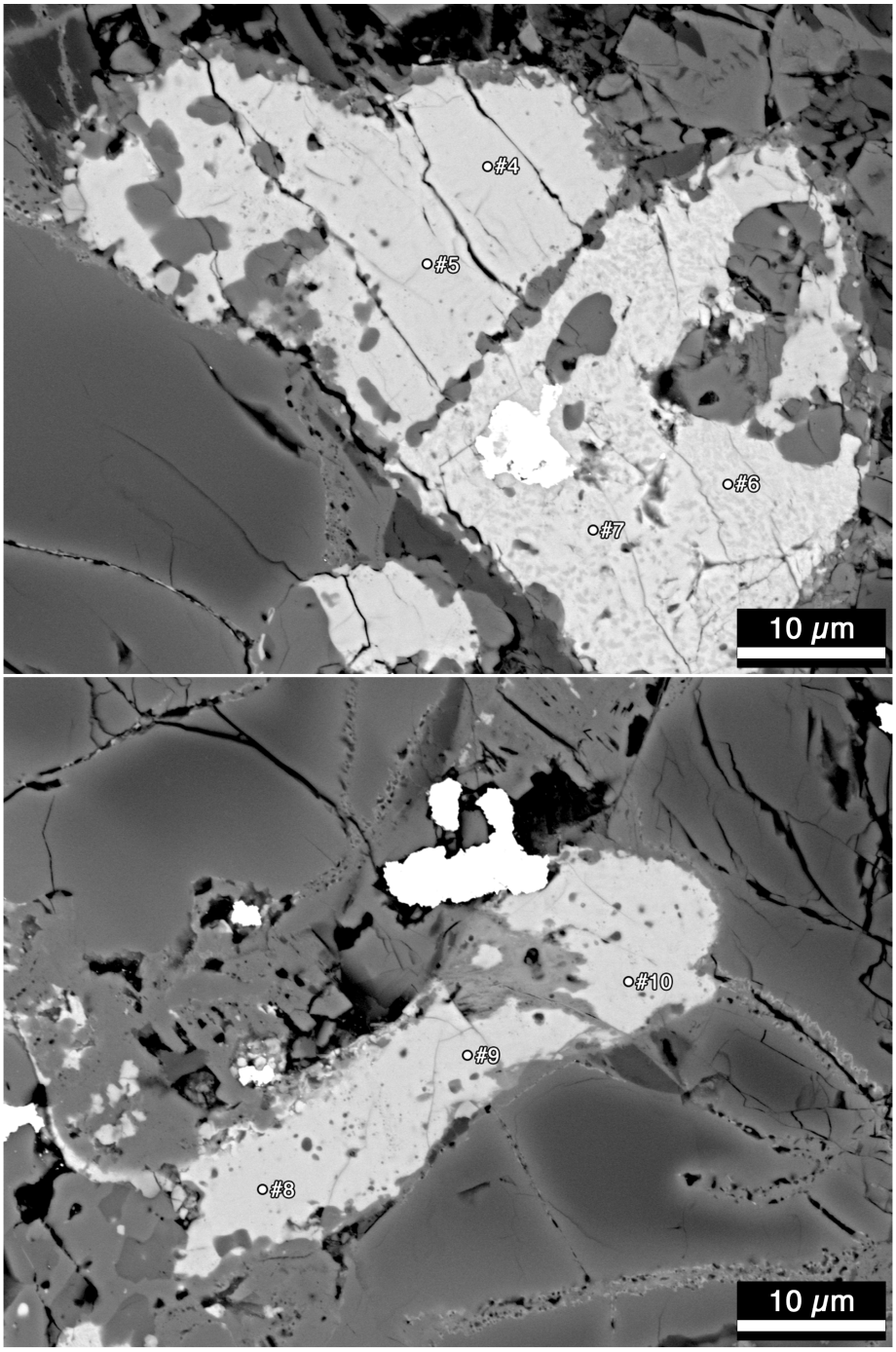

Fig. A6. (Continued)

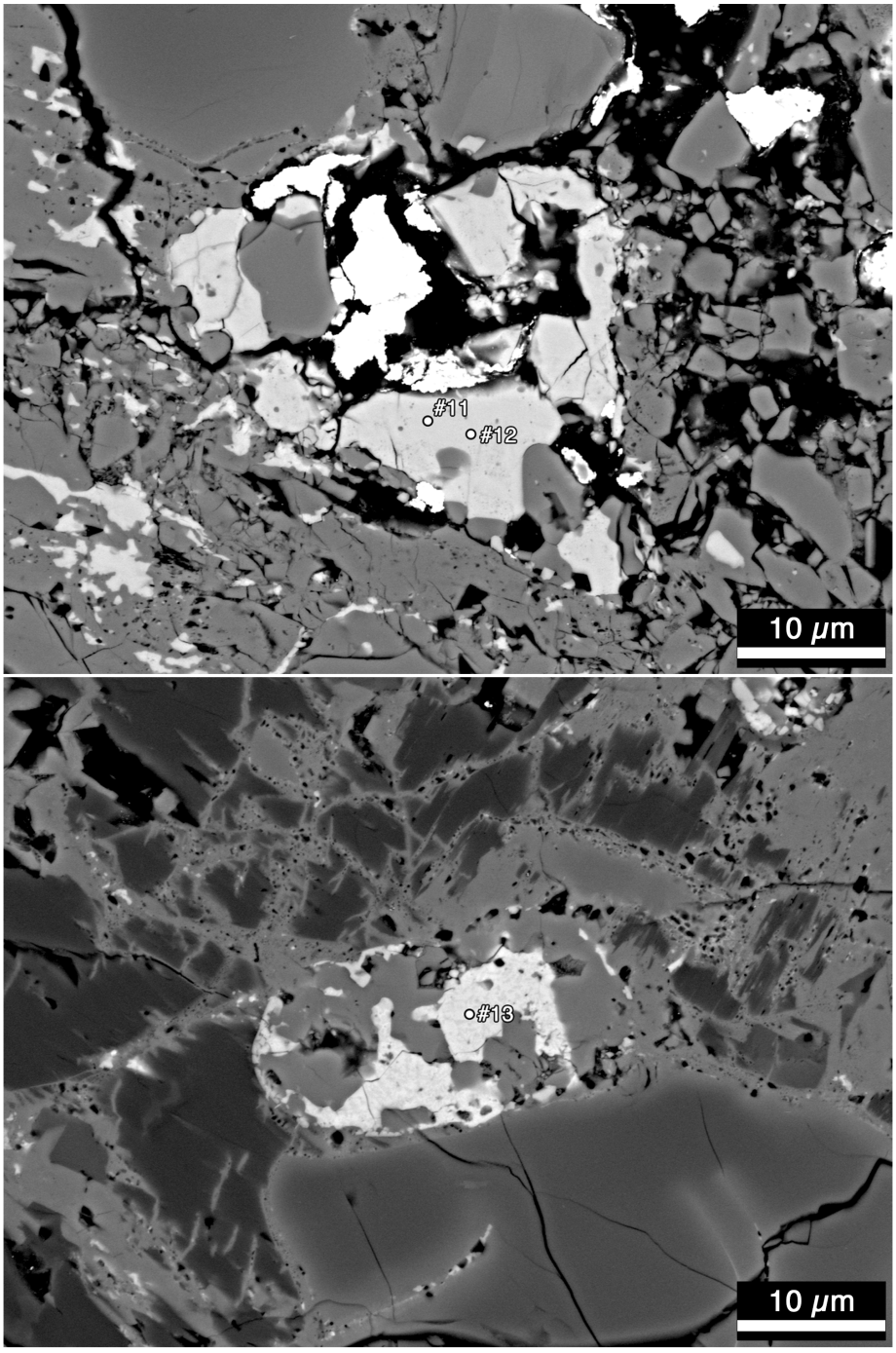

Fig. A6. (Continued)

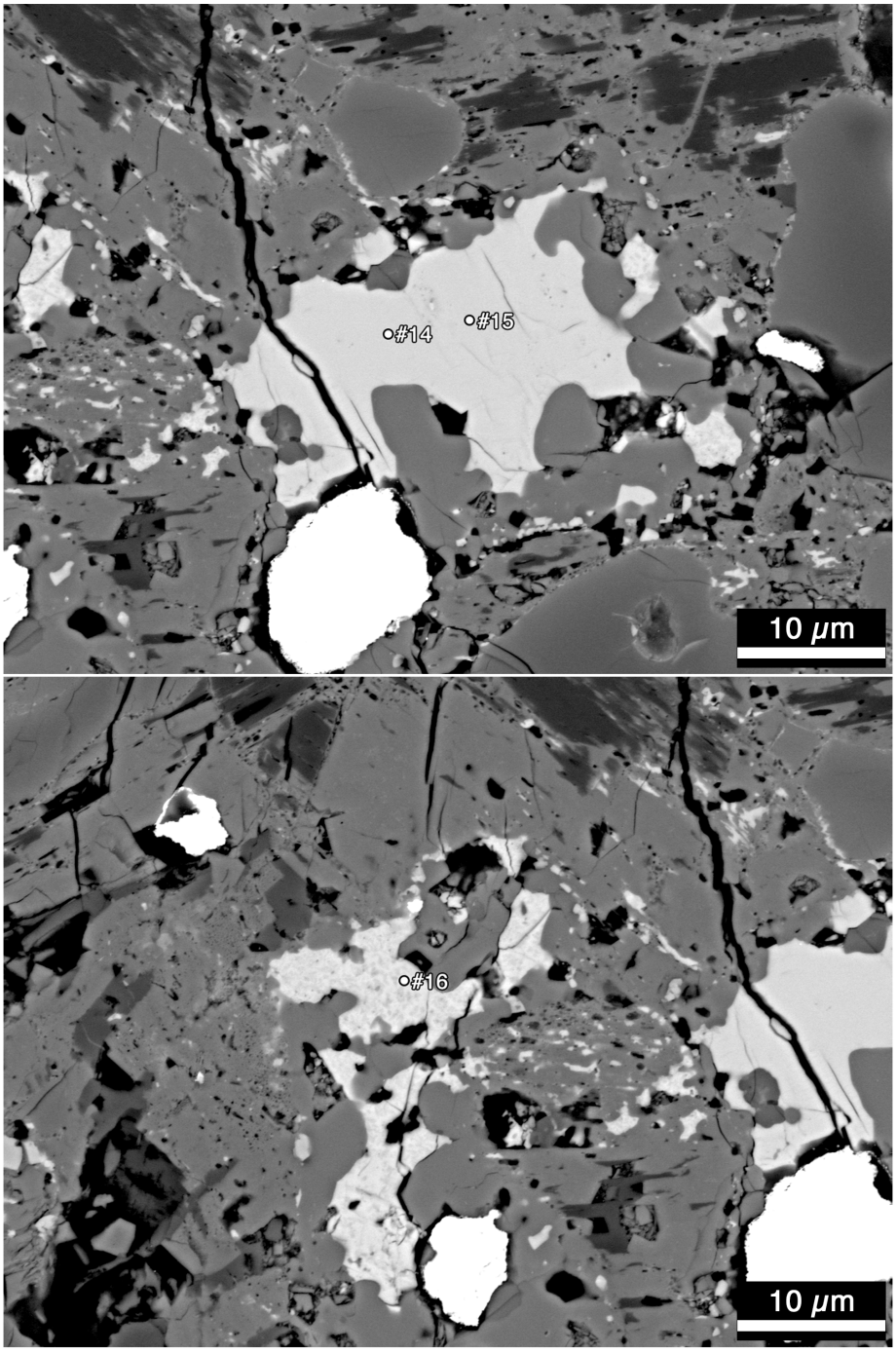

Fig. A6. (Continued)

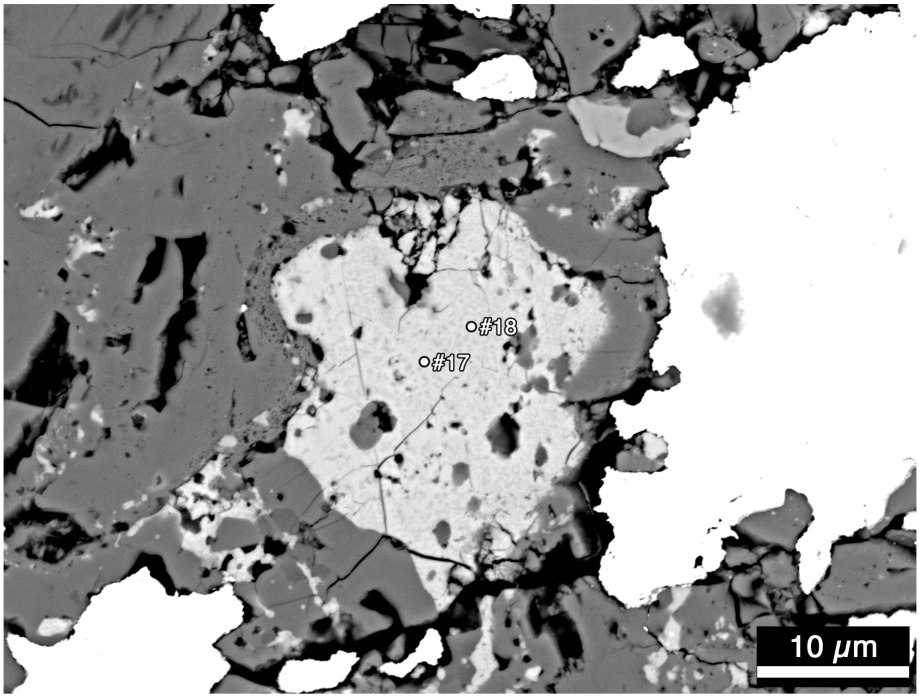

Fig. A6. (Continued)

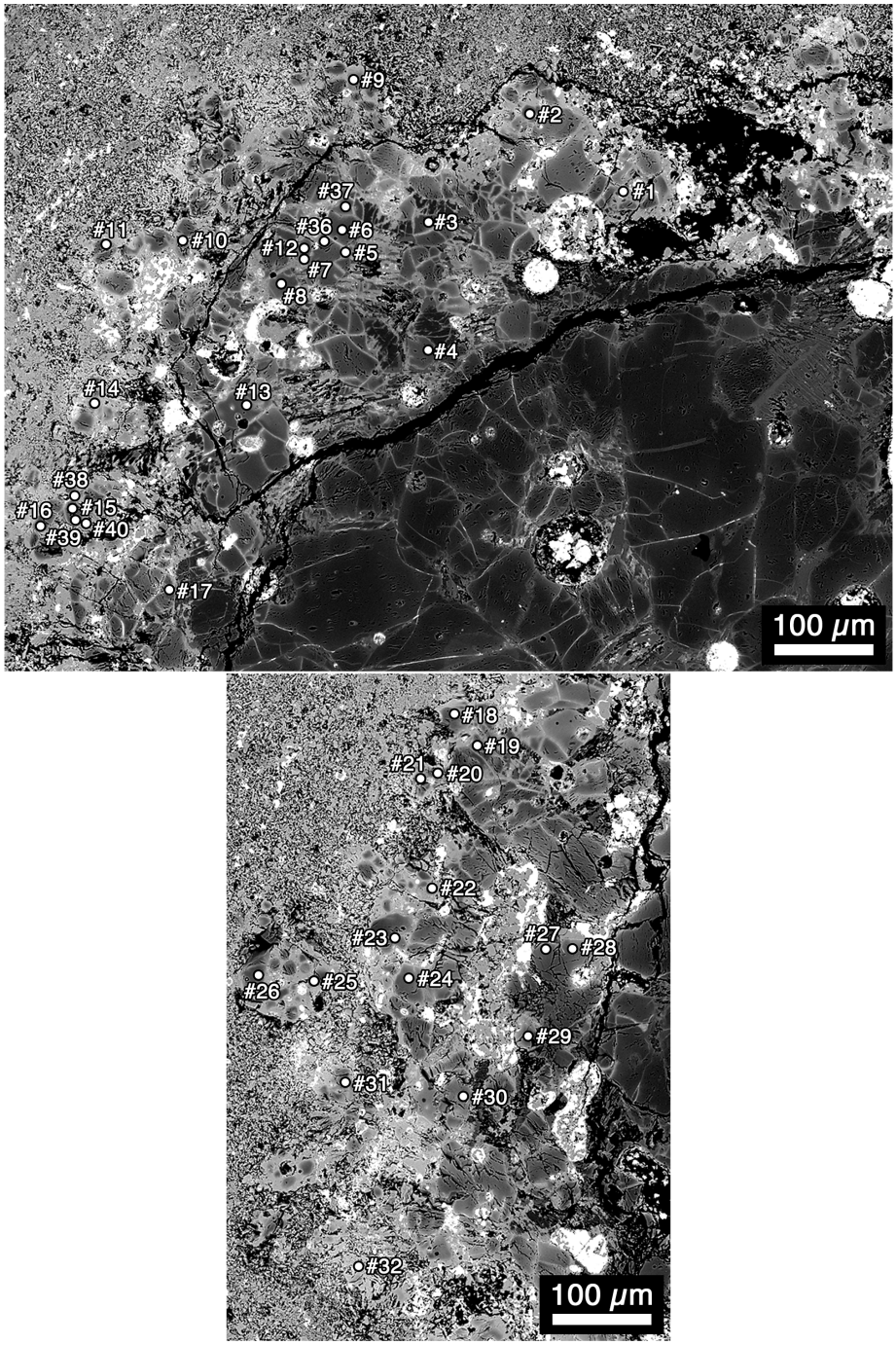

Fig. A7. White circles indicate locations of oxygen isotope analyses of olivine in the igneous rim. Numbers correspond to Table 11.

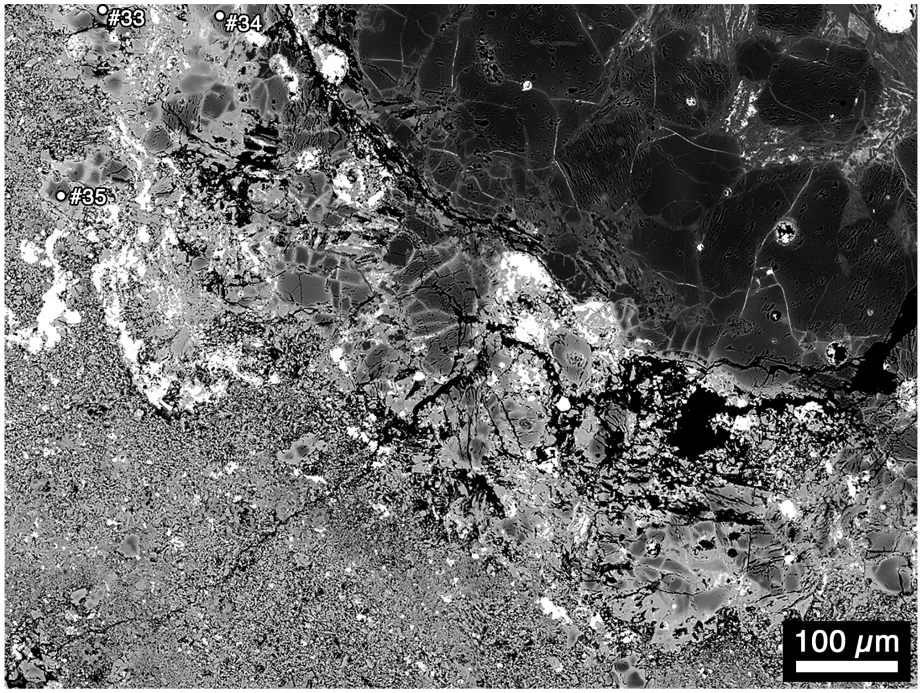

Fig. A7. (Continued)